Computational Study Of Redox Reactions in Transition Metal Compounds

Panagiota Pelekanaki

A dissertation submitted in partial fulfillment

of the requirements for the degree of

Doctor of Philosophy

of the

University College London.

Department of Chemistry

University College London

Declaration

I, Panagiota Pelekanaki confirm that the work presented in this thesis is my own. Where information has been derived from other sources, I confirm that this has been indicated in the thesis.

London, February 2015

Abstract

Redox processes taking place at transition metal (TM) ions embedded in inorganic matrices are industrially important, as they are relevant in many technological applications including heterogeneous catalysis, and hence the present computational study focuses on catalytic redox reactions. Of particular importance for oxidation reactions are the microporous aluminophosphate catalysts (AlPOs) in which Al ions can be replaced by redox-active TMs. We focus on the aerobic oxidation of linear alkanes catalysed by Mn-doped AlPO-5 and AlPO-34.

Firstly we compare the results deriving from the use of different functionals (GGA and hybrid exchange functionals). Calculated reaction and activation energies vary by changing the exchange and correlation functionals used in DFT. The rationale is that redox processes change the electronic configuration and number of *d*-electrons of the TM ions, and hence are expected to be affected by the self-interaction error (SIE) of local DFT functionals. The orbital-dependent solution obtained by inclusion of exact exchange in hybrid-exchange functionals corrects for the SIE. Since there are no experimental investigations to compare our results, we then calculated the Li intercalation potential of $LiMPO_4$ (M=Mn or Fe) using the same functionals as during the delithiation of $LiMPO_4$, the redox chemistry is the same exploited in MnAlPO-5. Amounts of HF exchange between 20-35%, give Li intercalation potential closer to the experimental value.

Moreover, we examine the oxidation of primary and secondary carbon atoms of linear alkanes (propane and hexane), and we compare the energetics in different MnAlPOs. We show that the pore size on AlPO-5 is too large to impose structural constraints while the smaller AlPO framework with the use of a longer alkanes can impose some constraints without, however, reversing the relative reactivity of carbon atoms.

Acknowledgements

First and foremost, I would like to thank my supervisors, Professor C. R. A. Catlow and Dr. F. Corà whose encouragement, supervision and support from the preliminary to the concluding level enabled me to develop a thorough understanding of the subject. Their guidance and inspiration provided me with significant values for my work and for my life.

I would also like to thank Dr. L. Gómez Hortigüela for his technical support and useful advice. I would like to acknowledge my colleagues at 351 KLB office for their contribution to a friendly working environment and for the helpful discussions.

Special thanks to Yorgos, for his patience, encouragement and faithful support during all stages of this Ph.D. I am also thankful to my dear friends Alkmini, Christina and Myrsini for being there when needed and for making my time in London enjoyable.

This thesis would be impossible without my family. I am grateful to my father Charalabos, my mother Ioanna and my sister Eleni for their endless love and for the unwavering support throughout this journey. They are my motivation, I love them and I always want to make them proud.

Finally, I acknowledge the use of the UCL Legion High Performance Computing Facility and associated support services in the completion of this work. Via our membership of the UK's HPC Materials Chemistry Consortium, which is funded by EPSRC (EP/L000202), this work made use of the facilities of HECToR and ARCHER UK.

List of publications

In preparation

P. Pelekanaki, L. Gómez Hortigüela, C.R.A. Catlow and F. Corà (2015). *Effect of exchange functionals on the calculated activation energies - A DFT study of the catalytic aerobic oxidation of ethane in MnAlPO-5.*

P. Pelekanaki, F. Corà and C.R.A. Catlow (2015). *Li Intercalation Potential of Olivine Phosphate Cathodes - A comparative study of electronic structure calculations.*

P. Pelekanaki, L. Gómez Hortigüela, F. Corà and C.R.A. Catlow (2015). *Mn-doped nanoporous aluminophosphate catalysts for the regioselective aerobic oxidation of hydrocarbons.*

Contents

1 Introduction **1**

1.1 Aerobic oxidation of linear alkanes catalysed by Mn-Doped nanoporous aluminophosphates (MnAlPO's) 4

1.2 Li intercalation in $LiMnPO_4$ and $LiFePO_4$ olivine structures 8

1.3 Thesis outline 10

2 Nanoporous aluminophosphate Catalysts (AlPOs) **11**

2.1 Introduction 11

2.2 Synthesis of microporous structures - the "template effect" 12

2.3 Electronic and structure characterisation of doped-AlPOs 13

2.3.1 Experimental methods 13

2.3.2 *Ab initio* modelling 15

2.4 Catalytic properties of doped AlPOs 18

2.4.1 Brønsted acid strength of lower valence dopant ions in AlPOs . 18

2.4.2 Lewis acidity in transition metal-doped microporous AlPOs . . 20

2.4.3 Redox activity of transition metal ions in microporous AlPOs . 23

2.5 Previous investigations on redox reactions using TM-doped AlPOs . . . 25

2.5.1 Baeyer Villiger oxidation of ketones to lactones 26
2.5.2 Epoxidation of alkenes 26
2.5.3 Aerobic terminal oxidation of linear alkanes 28
2.5.4 Selective oxidation of cyclohexane in air 29
2.6 AlPOs examined in this work 31
2.6.1 Mn-doped AlPO-5 31
2.6.2 Mn-doped AlPO-34 36
2.6.3 Challenges 37

3 Computational details and methods **39**

3.1 Introduction 39
3.2 Foundations of Quantum Chemistry 42
3.2.1 The Schrödinger equation 42
3.2.2 The Hartree-Fock method 44
3.3 Density Functional Theory 45
3.3.1 The Hohenberg-Kohn Theorems 45
3.3.2 The Kohn-Sham equations 46
3.3.3 Exchange-correlation functionals 48
3.3.4 Early approximations for exchange correlation energy 48
3.3.5 The problem of self-interaction 50
3.3.6 Orbital-Dependent and Hybrid functionals 52
3.4 Other electronic structure approaches 56
3.5 Basis Sets 57
3.6 Periodic Boundary Conditions 59

3.7 Methodology 60

3.7.1 Prior computational methods for transition metal-doped AlPO's 60

3.7.2 Transition state searching 61

3.7.3 Proposed methodology 63

3.8 High Performance Computing (HPC) 70

4 Effect of exchange functionals on the calculated activation energies - A DFT study of the catalytic aerobic oxidation of ethane in MnAlPO-5 71

4.1 Introduction 71

4.2 *Preactivation step* - Formation of the ethyl radical and Mn reduction . . 75

4.3 *Propagation step* - H-transfer from RH to $Mn^{III} \cdots$ OR 84

4.3.1 Up and Down spin choices of oxygen radical 91

4.4 Summary and Conclusions 92

5 Li intercalation potential of olivine phosphate cathodes - A comparative study of electronic structure calculations 95

5.1 Introduction 95

5.2 Approach and Methodology 98

5.3 Results and discussion 99

5.3.1 Structural parameters 99

5.3.2 Cell voltages 102

5.3.3 Electron density 107

5.4 Summary and Conclusions 110

6 Mn-doped nanoporous aluminophosphate catalysts for the regioselective aerobic oxidation of hydrocarbons 112

6.1 Introduction 112

6.2 Results and Discussion 115

6.2.1 Ethane VS Propane 115

6.2.2 Propane VS Hexane 126

6.2.3 Impact on energies with the increase on the amount of HF exchange 128

6.3 Summary and Conclusions 131

7 Conclusion 134

7.1 Summary of thesis contributions 134

7.2 Future work 137

Bibliography 140

Appendices 157

A Proof of HK Theorem 1 157

B Proof of HK Theorem 2 158

List of Figures

2.1 Schematic representation of hydrothermal (top) and ionothermal (bottom) synthesis of a tetrahedral zeolite-like framework. In the ionothermal synthesis, the solvent and the SDA are the same species. These species (e.g. water) can be also found in small amounts [56]. 14

2.2 Visualisation of the cage-structured MnAlPO-34 on the left and the channel-structured MnAlPO-5 on the right. Mn active site is represented in blue, P in brown, Al in green and O in red. 17

2.3 Electron spin density maps for (a) the isovalent 3+ ions and for the (b) low-valent 2+ transition metal ions in AlPO-34. The black and green lines represent the spin density, plotted between -0.05 and +0.05 au at linear steps of 0.005 au (black), and between 0.001 and 0.005au at linear steps of 0.001au (green). Continuous and dashed lines refer to positive and negative spin density, respectively. The continuous line is the isodensity level of 0.01 au calculated from the total electronic density, and represents the effective size of framework. On the left, the substitutional ions are Cr^{3+} (A), Mn^{3+} (B), Fe^{3+} (C), Co^{3+} (D) and on the right, the substitutional ions are Cr^{2+} (A), Mn^{2+} (B), Fe^{2+} (C), Co^{2+} (D), and Ni^{2+} (E). The plot (F) refers to the solution for Ni^{2+}, calculated with the B3LYP Hamiltonian [64]. 21

2.4 Representation of the AlPO-36 catalyst where manganese ions replace Al^{III} ions. Conversion of benzaldehyde to the perbenzoic acid intermediate affected by both dioxygen and Mn^{III} ions [37]. 27

2.5 Energy-minimised configuration adopted by (a)n-dodecane [28] and (b)n-hexane at 0 K inside an AlPO-18 framework [27]. 29

2.6 Plot representing the typical kinetics for the oxidation of cyclohexane with CoAlPO-36 as the catalyst [62]. 30

2.7 Catalytic cycle of cyclohexane oxidation on MnAPO-5 catalyst [35]. . 32

2.8 Preactivation mechanism. The black background shows initial catalyst and reactant molecules, whilst the red background presents the hydroperoxide intermediate. Yellow and blue backgrounds indicate intermediates produced and necessary to initiate subsequent reaction. Enthalpies are presented with red font colour for each elementary step and activation energies (in kJ/mol) with black [39]. 33

2.9 Propagation mechanism. Background colours and energies are presented as in figure 2.8 [42]. 34

2.10 Representation of the pore structures of (a) AlPO-5 (AFI) and (b) AlPO-34 (CHA) structure (pore apertures are respectively 7.3 Å and 3.8 Å). 37

3.1 A simulation cell surrounded by periodic images generated by PBC. The arrows indicate the movement of the molecules [121]. 60

3.2 Reaction profile where the reactant A converts to product C via the transition state B [124]. 62

3.3 Representation of AlPO-5 framework and indication of the distances of MR. 66

3.4 Schematic representation of $LiMPO_4$ olivine structure with PO_4 tetrahedra in light grey and MO_6 octahedra in dark grey. Li is represented by the black spheres in the interstitial channels. 68

4.1 View of the TS (left) and product (right) structures for the preactivation step. A hydrogen transfer to the active site takes place, yielding a Mn^{II} site and an ethyl (R·) radical, which is then rapidly stabilized by the addition of O_2 to form ROO·. Mn active site is represented in blue, P in brown, Al in green and O in red. 75

4.2 Reaction scheme showing the TS in preactivation step. 76

4.3 Energy profiles for the reaction step 1 calculated using nine functionals with different amount of HF exchange (BLYP, B3LYP, $F_{0.25}$-BLYP, F_0-PBE, $F_{0.05}$-PBE, $F_{0.10}$-PBE, $F_{0.25}$-PBE, $F_{0.50}$-PBE). 77

4.4 Calculated reaction enthalpies and activation energies as a function of the amount of HF exchange. With black and red are the relative values for F_x-BLYP functionals and with green and blue are for F_x-PBE functionals. 79

4.5 Calculated reaction enthalpies as a function of the amount of HF exchange for the component half cells (kJ/mol); a (Mn^{III} + H· → Mn^{II} (OH)), b (Mn^{III} + RH → R· + Mn^{II}(OH)) and c (RH → R· + ·H) . . . 80

4.6 Reaction profile diagrams using F_0-PBE, $F_{0.25}$-PBE, $F_{0.50}$-PBE. Energy diagram (black line), evolution of Mn spin (blue line) and of C spin (green line), and C-H distance (red line) in Å along the reaction coordinate (O(Mn)-H(CH_2CH_3)) distance). 82

4.7 Spin density maps of the transition state of reaction step (1) of PBE with 0% (a) and 50% (b) of HF exchange. F_0-PBE functional gives a product like TS while higher amount of HF exchange gives a reactant-like TS. 83

4.8 View of the TS (left) and product (right) structures for the propagation step. A hydrogen transfer to the active site takes place, yielding an ethyl (R·) radical. 85

4.9 Reaction scheme showing the TS in propagation step. 86

4.10 Projected density of states for Mn, O on the framework, O of the adsorbate, and total projection for PBE with 0% (a) and 25% (b) of HF exchange. The vertical line indicates the Fermi energy while black and red areas show the spin up and down contributions, respectively. 87

4.11 Calculated energy profiles for the reaction step 4.5a with different exchange functionals 88

4.12 Reaction profile diagrams using B3LYP, $F_{0.25}$-BLYP, $F_{0.25}$-PBE and $F_{0.50}$-PBE. Energy diagram (black line), evolution of Mn spin (blue line), C spin (green line) and O spin (red line) along the reaction coordinate ($O(OCH_2CH_3)$-$H(CH_3CH_3)$) distance). 89

4.13 Spin density maps of the transition state of reaction step (7) of B3LYP (a) and PBE with 50% (b) of HF exchange. 90

4.14 Calculated energy profiles of B3LYP, $F_{0.25}$-PBE and $F_{0.50}$-PBE functionals along the reaction coordinate distance for the two different spin directions, up (black line) and down (red line), of the radical O. 92

5.1 Schematic representation of $LiMPO_4$ olivine structure with PO_4 tetrahedra in light grey and MO_6 octahedra in dark grey. Li is represented by the black spheres in the interstitial channels. 97

5.2 Coloured lines indicate the relative error of the optimized volumes compared to experiment for the lithiated structures of (a) $LiMnPO_4$ and (b) $LiFePO_4$. Lighter, open symbols indicate corresponding delithiated phases 102

5.3 (a) Li intercalation potentials of $LiMnPO_4$ and $LiFePO_4$ olivine structures with different amounts of HF exchange and (b) Average deviation from experiment as a function of HF exchange. 105

5.4 Electron density map for the ferromagnetic $LiFePO_4$ system with the use of F_0-PBE. The α spin is indicated in red. Fe is represented in blue, P in yellow, Li in grey and O in red. 107

5.5 a) Mn spin density for $LiMnPO_4$ and $MnPO_4$ and b) Fe spin density for $LiFePO_4$ and $FePO_4$ along different amount of HF exchange. 109

6.1 Structure of the AlPO-5 on the left and of the AlPO-34 on the right highlighting the different pore sizes available. Pore apertures are respectively 7.3 Å and 3.8 Å. 114

6.2 View of the TS for the preactivation step. A hydrogen transfer to the active site takes place, yielding a Mn^{II} site and (a) a propyl or (b) an isopropyl radical is formed. Mn active site is represented in blue, P in brown, Al in green and O in red. 115

6.3 Reaction scheme showing the TSs in the preactivation step corresponding to selectivity to oxidation at (a) primary and (b) secondary C atoms. 116

6.4 Energy profiles for the H transfer from ethane(black line) from primary C of propane(red line) and from secondary C of propane(green line) for (a) MnAlPO-5 and (b) MnAlPO-34 frameworks. 117

6.5 The output file from the calculation of vibrational frequencies. 119

6.6 Calculated energy profiles for the two different spin directions, up (green line) and down (blue line), of the radical O. 121

6.7 Reaction scheme showing the TSs in the propagation step corresponding to selectivity to oxidation at (a) primary and (b) secondary C atoms. 121

6.8 View of the TS for the propagation step for the four (4) possible combinations of oxidation of propane. A red dot indicates in which position of the propane the oxidation takes place. Mn active site is represented in light blue, P in yellow, Al in pink and O in red. 122

6.9 Oxidation of propane in small pore apertures of AlPO-34 showing the bulkier TS due to the presence of two hydrocarbon molecules. 123

6.10 Propagation step with (a) AlPO5 and (b) AlPO-34 framework and propane as substrate; reaction profiles for four (4) possible combinations of primary and secondary carbon atoms, and (c) the relative reactions. 125

6.11 Structural representation of the H transfer from primary C atom of hexane in the double unit cell of MnAlPO-34. 126

6.12 Energy profiles for the H transfer from hexane from primary C1 and secondary C2, C3 carbon atoms in MnAlPO-34. 127

6.13 Energy profiles with the use of B3LYP and $F_{0.50}$-PBE functionals for (a) the preactivation step and (b) the propagation step. Ethane is used as substrate and AlPO-34 as framework. 129

6.14 Energy diagram for the activation of propane by MnAlPO-5. (a) Activation of terminal C atom and (b) Mn spin density, (c) activation of secondary C atom and (c) Mn spin density when using B3LYP and $F_{0.50}$-PBE hybrid exchange functionals. 130

List of Tables

4.1 Activation energies and reaction enthalpies with the use of all nine functionals. 78

4.2 Calculated reaction enthalpies of the component half-cells (kJ/mol); $\mathbf{Mn^{III} + H\cdot \rightarrow Mn^{II}\ (OH)}$ ($Mn(III) - O - P + \frac{1}{2}H_2 \rightarrow Mn(II) - OH - P$) and $\mathbf{RH \rightarrow R\cdot + \cdot H}$ ($CH_3CH_3(g) \rightarrow CH_3CH_2\cdot + \frac{1}{2}H_2$) 81

4.3 Mn-O bond distances in Å of the protonated oxygen. 84

4.4 Activation energies, reaction enthalpies, distances between the O which is nearest neighbour to the framework and the transferred H, as well as spin densities on O at the TS. 88

5.1 Cell parameters for the olivine-structured $LiMnPO_4$ and $MnPO_4$. 99

5.2 Cell parameters for the olivine-structured $LiFePO_4$ and $FePO_4$. 100

5.3 Volume of the olivine-structured $LiMnPO_4$ and and $MnPO_4$ and intercalation potentials. 103

5.4 Volume of the olivine-structured $LiFePO_4$ and $FePO_4$ and intercalation potentials. 104

5.5 Mulliken charges on M (Mn and Fe) and on O for $LiMnPO_4$ and $LiFePO_4$. 108

6.1 Summary of the energies (reaction enthalpies ΔH and activation energies Ea in kJ/mol) of the H abstractions from ethane and propane for both MnAlPO-5 and MnAlPO-34 frameworks. 116

6.2 Summary of the energies (reaction enthalpies ΔH and activation energies Ea in kJ/mol) of the H abstractions from propane for both MnAlPO-5 and MnAlPO-34 frameworks. 123

6.3 Summary of the energies (reaction enthalpies ΔH and activation energies Ea in kJ/mol) of the H abstraction from a hexane in MnAlPO-34 frameworks. 128

Acronyms and Abbreviations

AFM Anti ferromagnetic

AO Atomic Orbital

B3LYP Becke, three-parameter, Lee-Yang - Parr

BF Bloch Functions

DF Density Functional

DFT Density Functional Theory

FM Ferromagnetic

FTIR Fourier Transform Infrared Spectroscopy

GGA Generalized Gradient Approximation

GTF Gaussian Type Function

GTO Gaussian Type Orbital

HF Hartree-Fock

HK Hohenberg-Kohn

HSE Heyd-Scuseria-Ernzerhof

IP Interatomic Potential

KS Kohn and Sham

LDA Local Density Approximation

MGO Methanol To Gazoline

MM Molecular Mechanics

MR Membered Ring

MTO Methanol To Olefins

NEB Nudged Elastic Band

OCV Open-Circuit Voltage

PBC Periodic Boundary Conditions

PBE Perdew-Burke-Ernzerhof

PES Potential Energy Surface

QM Quantum Mechanics

QMC Quantum Monte Carlo

SDA Structure Directing Agents

SIC Self-Interaction Correction

SIE Self-Interaction Error

STO Slater Type Orbital

TM Transition Metal

Chapter 1

Introduction

The study of redox reactions has spawned considerable interest, as they are relevant in many technological applications from fuel cells and energy storage in lithium batteries [1–5], to corrosion processes [6–11] and heterogeneous catalysis. The economic importance of these processes, especially in the synthetic chemistry industry, which relies on the availability of new and improved catalysts, has led to continual attempts to investigate new materials whose electronic and structural properties are suitable for specific applications. A detailed atomic level understanding of structures, properties, reaction mechanisms of complex materials and energetics is extremely desirable as a tool to optimise existing processes and rationally design new ones, as well as preventing unwanted processes [12]. Redox catalysis has been studied theoretically and experimentally over decades in order to determine mechanistic aspects of chemical reactions and to measure thermodynamic and kinetic parameters.

Despite continuous advances in experimental methods and techniques, the study of reaction mechanisms is still an open challenge, particularly for the detection of short lived intermediates and transient species, that are present in low concentration during the overall process. It is becoming increasingly customary in such cases to complement experiment with quantum chemical computational studies. To fulfil this goal, general and reliable computer modelling techniques that do not rely on system-specific parameters are required. These methods have been developed over the decades and are now

a tool for research in solid-state chemistry, condensed matter physics and materials science in order to interpret the available experimental data as well as to predict new experimental observations. Computational studies for solid compounds are often performed at the Density Functional Theory (DFT) level. We should however bear in mind that, while the DFT theory is exact, practical implementations rely on approximations that are known to affect results. With this perspective in mind, addressing the accuracy achievable with available techniques is a topic of fundamental importance.

The motivation of this thesis is to perform a thorough computational analysis with molecular detail of redox reactions taking place at transition metal (TM) ions embedded in inorganic matrices. Of particular importance for oxidation reactions are the microporous aluminophosphate catalysts (AlPOs) in which Al ions can be replaced by redox-active transition metals such as Mn, Fe and Co. The incorporation of redox metals into these molecular sieves affords potentially interesting heterogeneous oxidation catalysts [13, 14]. These materials combine the reactivity of the redox-active cations with the unique spatial constraints imposed by the molecular dimensions of their microporous framework [15, 16]. Recent computational investigations based on B3LYP hybrid exchange-functional in DFT have been performed by Gómez Hortigüela *et al.* and determined the catalytic mechanism of the aerobic oxidation of ethane catalysed by Mn-doped nanoporous aluminophosphate-5 (MnAlPO-5). In the catalytic mechanism examined, redox activity is associated with a TM ion such as Mn, Fe, Co that replaces framework Al^{3+} sites and reversibly changes between 3+ and 2+ oxidation states during the catalytic cycle. In DFT studies, TM ions with open shell *d* electrons are sensitive to the details of the Hamiltonian, as these are the systems where the self-interaction error (SIE) of DFT is most pronounced. Because of the SIE, DFT results on redox reactions should be treated with care.

We will be mainly concerned on applications of DFT where the development of robust exchange and correlation functionals has been important [17, 18]. Early functionals used the local density approximation (LDA), which provides surprisingly good

results for metallic solids with delocalised electrons but revealed systematic shortcomings in the description of materials with localised electrons. The next generation of functionals, the so-called generalized gradient approximation (GGA) aimed at correcting those shortcomings [19]. Both of those functionals are known to fail in the description of the electronic properties of late TM compounds because of the self-interaction error which is considerable for strongly localized d or f states. The development of B3LYP and other hybrid functionals, which combine the GGA and exact exchange, allow improved accuracy and better agreement with experiment [20, 21]. Thus, we will discuss the performance of GGA and hybrid exchange functionals with different amount of HF exchange (between 0 and 50%) in modelling the catalytic oxidation of alkanes in MnAlPOs.

Clearly a reliable way of refining this range must be found, possibly by direct comparison to experiment, to establish confidence in the computational results. Unfortunately, the energetics of individual elementary steps in a complex catalytic cycle is not currently possible to measure exactly. Thus, we will exploit the fact that the Mn^{3+}/Mn^{2+} redox chemistry and local environment of Mn directly bonded to phosphate ions, is the same as in the intercalation chemistry of $LiMnPO_4$ (LMP) employed in lithium battery cathodes. The redox potential of LMP upon intercalation and deintercalation of Li is the $MnPO_4$ host is measured quantitatively in electrochemical cells, for instance via cyclic voltammetry. The shortcomings of DFT in localising an additional electron on Mn^{3+} during the catalytic cycle and the Li intercalation are very similar.

An extension of this computational study will focus on the catalytic properties of TM-doped AlPOs with different pore sized frameworks. We will examine selectivity issues related to the functionalisation of primary and secondary carbon atoms when the aerobic oxidation of linear alkanes is taking place in MnAlPO-5 and in the smaller MnAlPO-34.

We will now give a brief summary of the redox reactions examined in this thesis, considering their industrial importance and the demand for thorough computational analysis and finally, we will give the outline of the thesis.

1.1 Aerobic oxidation of linear alkanes catalysed by Mn-Doped nanoporous aluminophosphates (MnAlPO's)

Saturated hydrocarbons, or alkanes (methane, ethane, propane, hexane etc.), are amongst the most abundant organic molecules in nature on which the chemical industry has based the production of high added value organic compounds (hydroperoxides, alcohols, aldehydes, ketones, carboxylic acids, olefins, aromatic compounds etc.). However, they are known to be the least reactive organic compounds, which can be called "noble gases of organic chemistry". Due to their highly unreactive nature, their functionalisation is a challenging reaction. The chemical inertness of alkanes can be overcome if the transformations are carried out at high temperatures, but the selectivity of such processes is very low. The selective oxidation of saturated hydrocarbons under mild conditions is a difficult task due the lower thermodynamic stability of the C1 terminal oxyfunctionalization with respect to $C2\cdots C_n$ carbon atoms, but at the same time it is of great importance in catalytic chemistry as the terminal-oxidised alkanes like linear alcohols or acids are important feedstocks for the chemical, polymer and pharmaceutical industries [22]. Thus, terminal oxidation at primary carbon atoms is still a major challenge in modern catalysis research.

Traditional strong oxidants such as boiling nitric acid, concentrated sulphuric acid, chromic acid or potassium permanganate are aggressive agents and do not allow for selectivity control of hydrocarbon oxidation. Moreover, these oxidants are no longer environmentally acceptable. Hydrogen peroxide [23], organic hydroperoxides and N_2O can be used as alternative oxygen donors and permit some selectivity control

[15]; nevertheless, current environmental awareness as well as the cost of sacrificial oxidants make molecular dioxygen as the oxidant of the choice. The natural biological cycle is supported by atmospheric oxygen and a number of enzymes are capable of performing selective terminal oxidations; the active site is surrounded by several amino acid residues which impose stereochemical constraints resulting in selectivity and high activity under the most benign environmental conditions.

However, to date, there is no heterogeneous catalyst able to replicate the activity and selectivity features of enzymes in stable solid materials and fulfil all the conditions required for the industrial scale applications. Thus, new ways have been investigated to design inorganic catalysts, that would partially and regioselectively oxidize alkanes, using either molecular oxygen or air under mild conditions instead of sacrificial oxidants, as they are environmentally benign and reduce polluting by-products [24].

Crystalline nanoporous aluminophosphates (AlPOs) are heterogeneous systems that show efficacy as oxidation catalysts. AlPOs have been widely studied since their discovery by Wilson et al. in 1982 [25]. They are zeolite-like materials in which P and Al replace the Si ions in order to form a three-dimensional oxide network providing a range of polymorphic structures [26]. The activation of these crystalline microporous materials with different redox active transition metals such as Co, Mn and Fe which isomorphously replace Al in the AlPO framework, can give a series of doped materials with catalytic properties [13, 14, 27]. Microporous aluminophosphates have good thermal stability and can be easily prepared using structure-directing organic templates, providing a range of structures which differ in micropore and cage characteristics. In addition, the internal surfaces of AlPOs are only accessible to reactant molecules of particular size and shape, and yield products of appropriate dimension. In late 1990's, Thomas and co-workers [16, 28] discovered the catalytic activity of doped AlPOs in selective oxidation of the terminal carbon atoms in n-alkanes using molecular oxygen in a liquid-phase reaction. Essential for zeotype catalysts is the fine tuning of the pore

diameter which allows for the the terminal C atom of the n-alkane to approach the catalytically active site.

The intellectual challenge is to find a strategy for such environmentally acceptable objectives, as one-step processes and/or solvent free chemical conversions, using air or molecular oxygen as the oxidant [16, 28–32]. The use of dioxygen as oxidant is also desirable in other types of oxidations like the epoxidation of alkenes [33], the selective oxidation of cyclohexane [34–36] and the Baeyer−Villiger oxidation of ketones to lactones [37]. Oxidation reactions can be separated into three categories: (1) autoxidation through a free-radical chain reaction; (2) oxidation of the substrate co-ordinated to the metal ion followed by reoxidation of the reduced metal and (3) catalytic transfer of oxygen [15, 38]. The reaction conditions (gas or liquid phase, reaction temperature, pressure) and most importantly the nature of the metal and oxidant are the factors conducting the dominance of one of these mechanisms. The one-electron oxidants such as Mn, Fe and Co are known to be highly efficient catalysts for liquid-phase aerobic autoxidation reaction through the formation of free-radicals, as in the first (1) category [38]. In free-radical autoxidations, the intermediates are alkoxy and alkylperoxy radicals. The proposed elementary steps are summarised below in equations 1.1 - 1.7, where M is the transition metal.

$$RH + O_2 \rightarrow R\cdot + HOO\cdot \tag{1.1}$$

$$R\cdot + O_2 \rightarrow ROO\cdot \tag{1.2}$$

$$ROO\cdot + RH \rightarrow R\cdot + ROOH \tag{1.3}$$

$$ROOH + M^{II} \rightarrow RO\cdot + M^{III}OH \tag{1.4}$$

$$ROOH + M^{III}OH \rightarrow ROO\cdot + M^{II} + H_2O \tag{1.5}$$

$$RO\cdot + RH \rightarrow ROH \tag{1.6}$$

$$ROO\cdot + ROO\cdot \rightarrow ROH + R(H) = O + O_2 \tag{1.7}$$

Iglesia and co-workers have experimentally investigated the aerobic oxidation of cyclohexane and n-hexane catalyzed by a Mn-doped aluminophosphate with the AFI framework structure (MnAPO-5) [31, 35]. In order to determine the main reaction intermediates, they proposed a reaction mechanism based on extensive spectroscopic and isotoping labelling techniques that is summarised by the reaction steps 1.1 - 1.7. However, the *in situ* detection and analysis of a large number of intermediates involved is a difficult task. Computational methods based on electronic structure techniques can in this case be applied proficiently to complement the experimental results. The scheme proposed by Iglesia *et al.* was the starting point of computational investigations by Gómez Hortigüela *et al.* [39–43], using Density Functional Theory methods. They revealed the whole catalytic cycle of the aerobic oxidation of ethane catalyzed by Mn-doped AlPOs, which comprises over 20 reaction intermediates.

The contribution of this thesis is to build on the earlier studies by Gómez Hortigüela *et al.* in three complementary directions. The first includes a comparison of results calculated with different functionals: B3LYP results are complemented with a selection of other GGA and hybrid exchange functionals. The goal is to identify the sensitivity of results to the choice of functional in DFT calculations, in two representative steps of the catalytic cycle, proposed by Gómez Hortigüela *et al.* [39, 40]. The steps chosen are the abstraction of H from ethane in the preactivation phase, which involves a reduction of the Mn^{III} site to Mn^{II}, as in equation 1.1, and one step of the radical propagation mechanism where Mn does not change oxidation state, as in equation 1.6. Beside the intrinsic interest of this study, understanding how results depend on the choice of functional is fundamental in guiding future work.

The second direction involves the use of a different aluminophosphate framework, in particular the small pore AlPO-34. Our aim here is to compare the energetics for the aerobic oxidation of ethane in Mn-AlPO-5 and Mn-AlPO-34, and quantify the steric constraints generated by the framework structure in different steps of the reaction mechanism.

The final direction, is to discriminate the reactivity of primary and secondary carbon atoms to oxidation, which is one of the most pressing open questions in the MeAlPO literature. To achieve this, we examine the oxidation of ethane, propane and hexane in AlPO-5 and AlPO-34.

1.2 Li intercalation in $LiMnPO_4$ and $LiFePO_4$ olivine structures

One of the major challenges of chemistry in 21st century is the development of cleaner and sustainable sources of energy. A range of energy conversion and storage technologies, such as fuel cells and lithium rechargeable batteries, have been developed to relieve dependence on fossil fuels and to cut carbon emission. The performance of these energy systems depends crucially on the properties of their component materials. Innovative materials chemistry lies at the centre of advances in this field; an excellent example already commercially available are the Li-ion rechargeable batteries, whose high energy density has transformed portable electronic devices during the past two decades [44] and whose use for purposes of communication, data processing and transmission, entertainment, etc. is growing rapidly [45]. The vision of massive commercial use of electrically powered vehicles is under active commercial development [46], but requires even more efficient batteries, with a number of crucial properties. A crucial key for a good battery design depends on the choice of cathode material.The cathode should be both an ionic and electronic conductor in order to allow for the insertion/deinsertion of lithium and rapid charge and discharge capability. Furthermore, the volume change of the cathode during its operation should be as small as possible, as this ensures good reversibility and cycle life. The knowledge of the potential at which Li can be removed and inserted, is also a crucial factor in defining whether new materials are suitable as cathode materials in rechargeable lithium batteries.

Computer modelling techniques are as we have discussed, well-established tools in the field of solid state chemistry and have been applied successfully to the design

of batteries [5, 9, 47] since they can be used to calculate important properties such as open-circuit voltage (OCV) and energetics without the requirement of experimentally measured input data.

There is considerable interest in the use of lithium transition metal phosphates with an ordered olivine structure $LiMPO_4$ (M= Fe and Mn) as cathode materials for large-scale applications owing to their low cost, stability, flexibility and competitive electrochemical properties [1, 47–50] . Both $LiMnPO_4$ and $LiFePO_4$ have received growing attention as the cathode material for lithium-ion batteries [1–5], in particular, the electrochemical performance (high operating voltage; large theoretical gravimetric capacity) of $LiFePO_4$ [51, 52] makes it commercially viable.

The operative redox couple of $LiMnPO_4$ and $LiFePO_4$ is M^{3+}/M^{2+}. The reduction from 3+ to 2+ oxidation state requires a change of the electronic configuration from d^4 to d^5 for Mn and from d^5 to d^6 for Fe and thus, the localization of an extra electron on the TM cation. This change of electronic configuration of Mn and Fe is the same as that observed in selective oxidation catalysts. Such a reaction is a typical example of an electronic state where the DFT solution is affected by a large SIE. As the redox potential of $LiMnPO_4$ is well characterised quantitatively through its Li battery applications, $LiMnPO_4$ is a suitable reference to assess the DFT results also in the heterogeneous catalytic applications of MnAlPO's. Thus, density functional calculations using GGA and hybrid functionals with different amounts of HF exchange are performed in order to produce a benchmark of different functionals by examining how the amount of Hartree-Fock (HF) exchange can influence the intercalation potential of the topical olivine structures, $LiMnPO_4$ and $LiFePO_4$ thereby guiding further configurational studies of metal insertion on related reactions.

1.3 Thesis outline

In this research, we focus on particular redox reactions coupling the computational and experimental results of others where available with our theoretical calculations. The remainder of this thesis is organised as follows. In **Chapter 2**, we review the available background work on experimental and computational investigations of TM-doped nanoporous aluminophosphate catalysts. Moreover, we discuss the unraveled catalytic mechanism of the ethane with Mn-doped AlPO by Gómez Hortigüela *et al.* and the elementary reaction steps of this mechanism we chose to focus on. **Chapter 3** gives a detailed description of DFT and the problem of SIE arising when TM with strongly localised *d* states are involved. The computational methodology used for this thesis is also presented. **Chapter 4** presents our DFT study regarding the effect of exchange-correlation functionals on the calculated activation energies when the aerobic oxidation of ethane catalysed by MnAlPO-5 takes place. As there are no experimental investigations to validate our results, in **Chapter 5** we use $LiMPO_4$(M=Mn or Fe) which has a similar behaviour with our MnAlPO-5 system. We calculate the Li intercalation potentials again with a selection of functionals with different amount of HF exchange and we compare our results with the experimental and computational investigations available. In **Chapter 6** we examine any regioselectivity issues regarding our system when the framework changes from MnAlPO-5 to the smaller-pore MnAlPO-34 and also when the substrate changes from ethane to propane and then to hexane. Finally, **Chapter 7** concludes this work and discusses future directions towards catalytic redox reactions.

Chapter 2

Nanoporous aluminophosphate Catalysts (AlPOs)

2.1 Introduction

Contemporary catalytic chemistry focuses on the design of new heterogeneous catalysts and reaction pathways, through the synthesis of new microporous materials with enhanced size-shape selectivity, and with the addition of different catalytically active sites within the solid. Microporous aluminophosphate catalysts (AlPOs) have been widely studied due to their rich polymorphic behaviour. They are crystalline oxides structured by corner-shared TO_4 tetrahedra (T = Al, P), and containing internal cavities and channels of similar size to those of small organic molecules [53]. Molecules are able to diffuse through the channels and react within the solid, and this microporous architecture enables an accurate control and design, at the atomic level, of the reactions that can take place inside the solid [54]. The unique structural features of microporous oxides make AlPOs interesting in dense heterogeneous catalysis, as the reactants can be in contact with the internal surfaces of the solid, while the active sites are uniformly distributed in the bulk and not only on the external surfaces. The activation of AlPOs with transition metal (TM) ions such as Mn, Fe, Co and Ti can give a series of doped materials which open up new catalytic opportunities in the field of selective and par-

tial oxidation catalysis [24]. Although they are similar to zeolites, AlPOs comprise more types of framework dopants and at higher concentrations. In order to gain control of the activity associated with doped-AlPOs, we need to understand the structural and electronic properties of the TM dopants and how their constraint environment in microporous framework influences the catalytic behaviour.

In this Chapter we review structural and catalytic properties of these materials, in the latter case focusing on oxidation catalysis, and we also describe the AlPO systems examined in this work.

2.2 Synthesis of microporous structures - the "template effect"

Crystalline microporous aluminophosphate materials can be synthesised in different compositions. They differ from zeolite synthesis in that they are normally performed in acidic conditions. For their synthesis hydrothermal methods can be applied with water as the solvent, in a sealed autoclave under autogenous pressure [55] to form a homogeneous aqueous gel(or sol-gel as the synthesis can also take place in solution) [56] (see figure 2.1). The reaction mixture usually includes an organic template that guides the synthesis pathway towards particular structures. These organic molecules are generally known as structure-directing agents (SDAs) [57, 58]. During crystallization, they are encapsulated within the void space of the nascent frameworks without changing their chemical identity. As a result the shape and the size of the SDAs play an important role in this templating ability. A well-defined molecular shape increases the "template effect" but too rigid molecules can not adapt to the AlPO framework. Kinetics and thermodynamics are two other factors that can affect ability of a template molecule to direct the crystallisation of AlPO [57].

Solvothermal is a general term to describe the synthesis of materials with the use of a solvent [59]. In the case where water is the solvent the method is the hydrothermal

synthesis, as it has been already mentioned. However, there is many cases where the solvent can be alcohol, hydrocarbon, pyridine or other organic molecule and they can vary from non-polar and hydrophobic to polar and hydrophilic [59].

Ionothermal synthesis is another method of producing AlPOs, based on the utilisation of ionic liquids as both the solvent and the organic SDA [60]. This method has several advantages over hydrothermal or other traditional methods (figure 2.1). The fact that the solvent is also the SDA reduces any competition between the two, and the low vapour pressure of ionic liquids means that the preparations can take place at high temperature while pressure is maintained at ambient levels. Moreover, the different chemistry of the ionothermal solvent system compared to those traditionally used, produces conditions under which novel types of frameworks appear to be accessible.

2.3 Electronic and structure characterisation of doped-AlPOs

2.3.1 Experimental methods

A prerequisite for understanding the catalytic properties of TM doped aluminophosphates is thorough characterisation of the TM ion environment [61]. Therefore, the investigation of the electronic structure properties of microporous aluminophosphates is of great interest in fundamental research. A large variety of different characterisation methods have been applied depending on the nature and the valence state of the TM dopant in order to unravel the environment of the TM ion. The low level inclusion of the dopant in the framework, usually results in a disordered incorporation. In this case, element-specific spectroscopic techniques, such as X - ray absorption spectroscopy (XAS), can be employed to obtain structural information of the dopants. In particular, EXAFS (extended X-ray absorption fine structure) studies can describe the short-range order of selected atomic species regarding the number of neighbours, distances, and thermal and static disorder within the range of those distances; however,

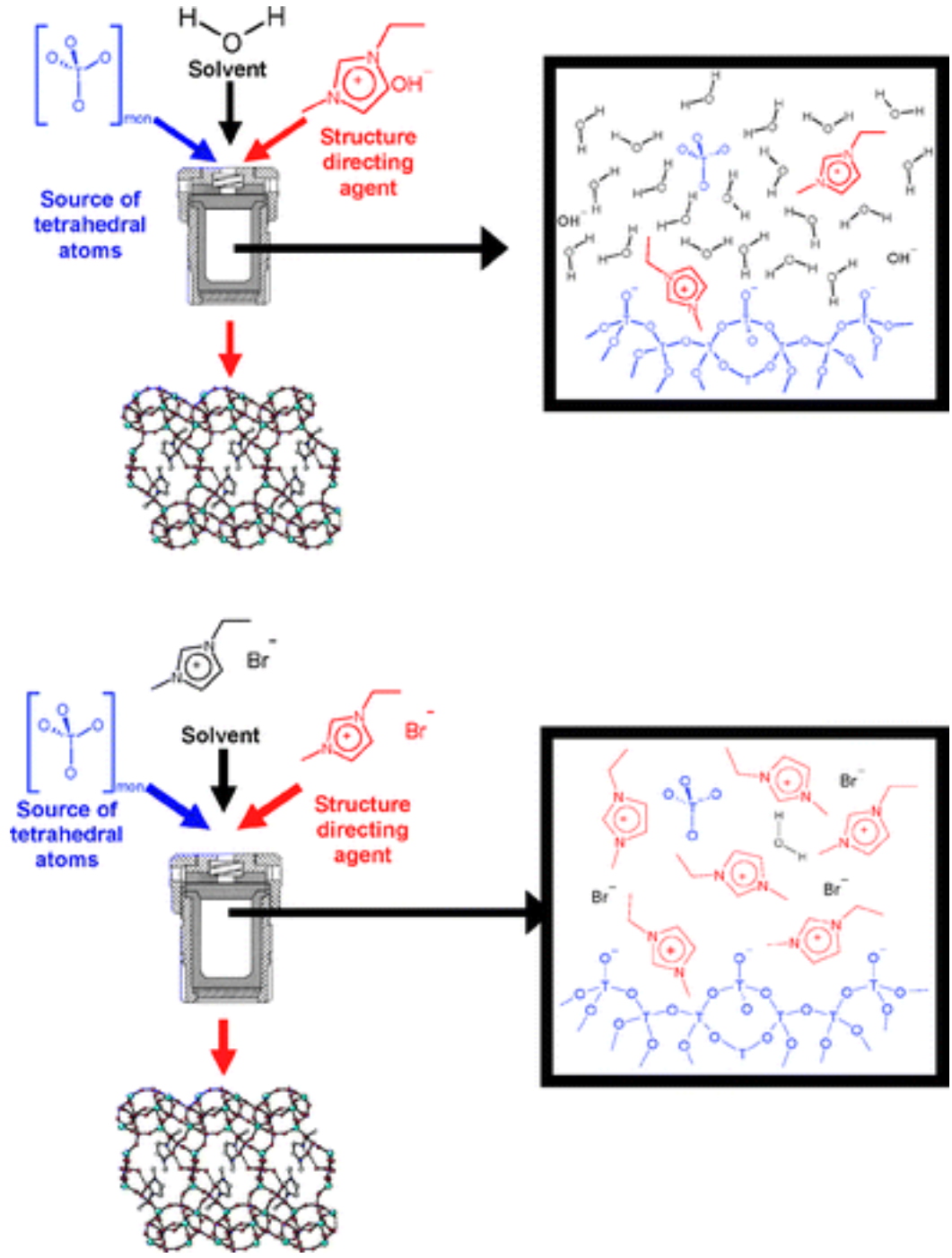

Figure 2.1: Schematic representation of hydrothermal (top) and ionothermal (bottom) synthesis of a tetrahedral zeolite-like framework. In the ionothermal synthesis, the solvent and the SDA are the same species. These species (e.g. water) can be also found in small amounts [56].

when there is more than one coordination environment and/or oxidation state, EXAFS provide average values for the selected element over the whole structure. While XAS is suitable to determine the local structure of the metal centres, X - ray diffraction (XRD) is essential to monitor the crystallinity of the sample and thus, a combination of both methods is suggested. An additional advantage of combined XRD/XAS techniques is that measurements can be performed *in situ* at operating conditions and with reasonable time resolution. Sankar *et al.* [62] have used XRD/XAS to investigate the integrity of the microporous Co-doped AlPO structure as well as to determine the redox chemistry associated with the cobalt ions. Thomas *et al.* [63] have also used both techniques to investigate local structural changes around manganese (or cobalt) active site, in the selective oxidation of linear alkanes in AlPOs. Infrared (IR) and nuclear magnetic resonance (NMR) spectroscopy can also be used to study the catalyst *in situ* under working conditions.

UV-visible spectroscopy is commonly employed for the characterisation of doped AlPOs. It has been used to determine the oxidation state of the TM in MAlPO samples (M = Mg^{2+}, Mn^{2+}, Co^{2+} etc.), before and after the catalytic reactions. In the study of Modén *et al.* [31] on the mechanism of cyclohexane oxidation on MnAPO-5 catalysts, the UV-vis spectra of the MnAPO-5 have shown that Mn^{2+} represents the most abundant active structure during steady-state catalysis.

2.3.2 *Ab initio* modelling

Corà *et al.* [64] studied computationally the framework stability of TM-doped zeotypes. A structural analysis on AlPO-34 (figure 2.2) showed that AlPOs have a molecular-ionic character, and are consistent of Al^{3+} and PO_4^{3-} ions. M is the dopant atom, O_n (n=1-4) is the nearest neighbour oxygens to the M active site and T is a generic site of the framework which can also include the dopant ion. They found that the M-O_H distance to the protonated oxygen is at least sufficiently longer than the three $M-O_{1-3}$

to the non-protonated oxygens. Jahn-Teller type distortions for open-shell dopant ions, do not play a major role compared to the relaxation around the acid OH group.

From the calculated electronic density it was suggested that the bonding characteristics of T-O (T = Al, P) are "local" property of the solid, and are only slightly affected by the long-range crystalline structure. By calculating the values for the flexible T-O-T angles it was found that the structural distortion caused by the dopant is "local" affecting the nearest neighbour ions, but not the more distant of the framework. In particular, the angular distortion is highly pronounced around the protonated oxygen where M-O_H-T angle changes up to 30^o for large dopants. Compared to the covalent PO_4^{3-} ions where angular constraints are pronounced, the ionic character of the AlO bonds, leads to little angular strain in the AlO_4 tetrahedra.

Ab initio calculations by Saadoune *et al.* [13] have also shown that the local environment of Mn and Co dopants is a distorted tetrahedron because of the Jahn-Teller distortions and moreover, the bond distances between the M^{III} dopants and the neighbouring oxygens reveal an ionic character, explaining the Lewis acidity of the M^{III} ions.

Atomic, chemical and structural properties of 23 substitutional dopants in the AlPO-34 framework have been examined in [64]. This study covers most of the isomorphous framework replacements that have been examined experimentally, as well as framework replacements that have not been achieved, yet. The ionic size of the dopant plays a major role in characterising the properties of the doped frameworks while affecting a wide range of their features, from the local distortion around the dopant to the incorporation energy of the dopant in the framework and its site ordering.

The complex catalytic behaviour displayed by AlPOs depends on a combination of structural and chemical properties of the active site, which must be assessed on an individual basis. The behaviour can be rationalised by dividing the framework T sites into two structural types (figure 2.2); the *caged* and *free* according to their local structural constraints. In the former case, the framework forms a rigid structure around the

site, while the free T sites are located in more flexible regions of the framework. Bigger dopants, although they may diffuse more slowly in the framework, tend to substitute free T sites, located in unconstrained regions of the framework. Smaller dopants are more stable energetically when they replace T sites positioned in smaller cages. This site preference grows as the size difference between host ion and dopant increases.

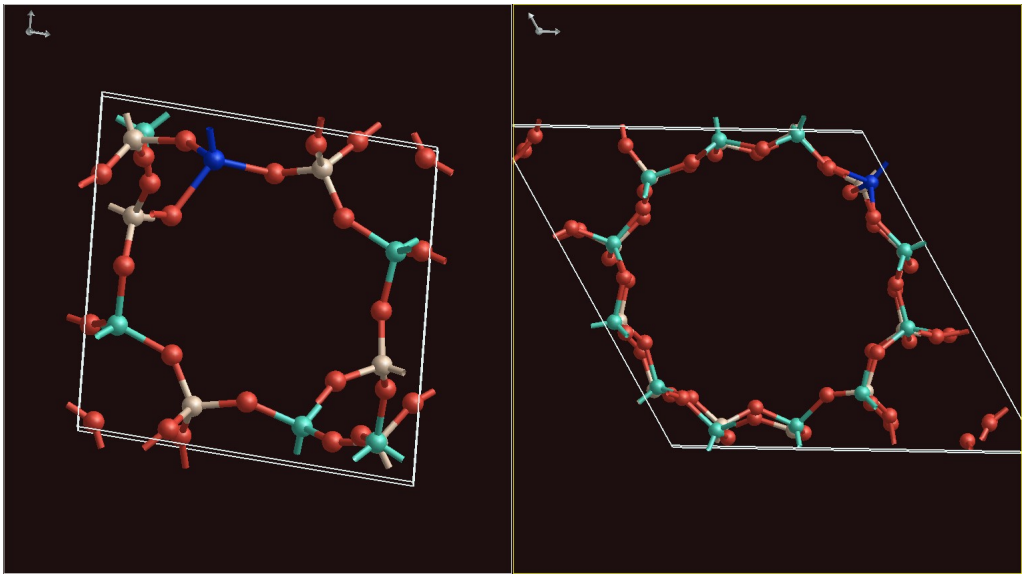

Figure 2.2: Visualisation of the cage-structured MnAlPO-34 on the left and the channel-structured MnAlPO-5 on the right. Mn active site is represented in blue, P in brown, Al in green and O in red.

2.4 Catalytic properties of doped AlPOs

After the electronic and structural characterisation of the doped frameworks, in this part we present three properties of the dopant ions that are of direct interest for their catalytic behaviour. These are the Brønsted and Lewis acid strength, and the redox potential.

The catalytic activity of TM-doped AlPOs has been widely examined experimentally. As the catalytic activity of AlPO materials can be related to their acidity, fourier transform infrared spectroscopy (FTIR) spectroscopy has been used for acidity measurements. For example, in the study of Gómez Hortigüela [65], the MgAPO samples were pressed into thin self-supporting wafers and activated in vacuum with CaF_2. The acidity of these calcined samples was assessed by pyridine adsorption and characterised by FTIR spectroscopy. In combination with XAS, these *in situ* techniques give quantitative knowledge about the local structure of metal-ion centred active sites [27].

In this part we will give strong emphasis on previous computational investigations on the catalytic activity of AlPOs.

2.4.1 Brønsted acid strength of lower valence dopant ions in AlPOs

Various doped AlPOs and zeolites show solid acid behaviour, which is of great interest in heterogeneous catalysis [54] . For example, the transformation of methanol to olefins (MTO) and methanol to gasoline (MTG) are common acid-catalysed reactions that employ the shape-selectivity of acid zeotypes [66]: small-pore frameworks such as H-SAPO-34 yield the MTO reaction [67] while larger frameworks, like H-ZSM5 yield the MTG reaction [68]. The introduction of acid protons in zeotype frameworks effects charge-compensation for low valence dopant ions. In principle, isomorphous substitution of a framework cation with any low valence dopant can take place, e.g. M^{2+}/ Al^{3+} and M^{4+}/ P^{5+} substitutions in AlPOs require a charge compensation which can be accomplished with the use of acid protons. In order to optimise the activity and/or selectivity of the catalysts without extensive testing of every dopant, it is useful

to scale the relative acidity for the possible dopants and correlate the acidity with the chemical composition. There are several comparative experimental studies which have investigated the correlation of the catalytic activity for isostructural frameworks with the dopant type. Thus, correlations between the the acid strength of doped zeotypes with either ionic radii [69] , electronegativity [70] and T-O_H-T' bond angle of the protonated oxygen with its nearest neighbour ions T and T' in the framework [71] have been proposed. Corà *et al.* [64] claimed in their computational study that experimental comparison of the properties for all possible dopant ions is limited to only a subset of the possible low valence ions due to restrictions arising from the framework stoichiometry. In particular, it is difficult to obtain isomorphous substitutions of low valence ions which are often energetically unstable, while the use of stoichiometric amounts of different dopant ions during the synthesis may lead to to different concentrations of dopants in framework and extra-framework positions in the final product. In addition, it is possible to create different active defect centres in the catalyst which may interact with each other if they are in the same region, which can, as a result, change the activity of the catalyst. However, they have shown that computer modelling is able to control the above variables and define a scale of relative acidity for the possible dopants while grading their catalytic activity. They applied computational modelling techniques (with periodic QM calculations) to study a set of 17 low valence dopant ions isomorphously substituted in different zeotypes. The relative acid strength due to the low valence dopant ions was screened by calculating OH stretching frequency, ν_{OH} as both acidity and ν_{OH} are often assumed to correlate [72]: a stronger OH bond yields a higher value of ν_{OH} and a weaker acid site. They showed that within the structural limitations imposed by the relative size of dopant and host framework ions, smaller dopants yield shorter M-O and *M*-H distances in the equilibrium structure, and give lower ν_{OH}. As a result they are stronger acids. Thus, the ionic size of the dopant ion *M* gives the biggest influence on the acid strength of doped AlPOs.

The major role of the dopant in characterising the properties of the doped frameworks have been also investigated from Elanany *et al.* [73]. They studied computationally using DFT, the relative strength of Brønsted acid sites in isomorphously substituted MAlPO-34 (M= Ti^{4+}, Si^{4+}, Cr^{2+}, Mn^{2+}, Fe^{2+}, Co^{2+} and Ni^{2+}). Ammonia (NH_3) was used as a basic probe molecule and the relative acidity was measured from the calculated values of the adsorption energies, suggesting that MnAlPO-34 has the strongest Brønsted acid site.

2.4.2 Lewis acidity in transition metal-doped microporous AlPOs

There has been a lot of debate over the origin of Lewis acidity in microporous framework oxides [74, 75] . Experimental data have shown the presence of two discrete adsorption sites, attributed to the framework Brønsted and Lewis acid sites [76]. The incorporation of TM ions in the AlPO framework can give rise to the formation of bridged hydroxyl groups (Brønsted sites) of different acidic strength, while Lewis sites of low as well as of high acidity are simultaneously generated. However, all dopant ions do not interact in the same way with Lewis bases; for example, Ni-doped AlPOs have lower concentration of strong acid Lewis sites compared to their Co and Mn analogues.

QM calculations have been performed in order to examine the origin of Lewis acidity in doped AlPO-34 with 2+ and 3+ TM ions as dopants [64]. The calculated electronic distribution of the TM dopants and the orientation of the unpopulated and/or partially filled *d* orbitals were used to explain the presence or absence of Lewis acidity in the framework. Figure 2.3 presents the plots from the calculated total and spin electronic density of each TM in its equilibrium structure [77]; (a) shows the results for the isovalent 3+ ions, and (b) the results for the low-valent 2+ ions.

The plane in its plot is chosen to contain the M-O_H-P unit (the TM dopant, one of its nearest neighbour oxygen ions and the next nearest phosphorus ion bonded to the oxygen). The spin density in both (a) and (b) represents the distributions of the

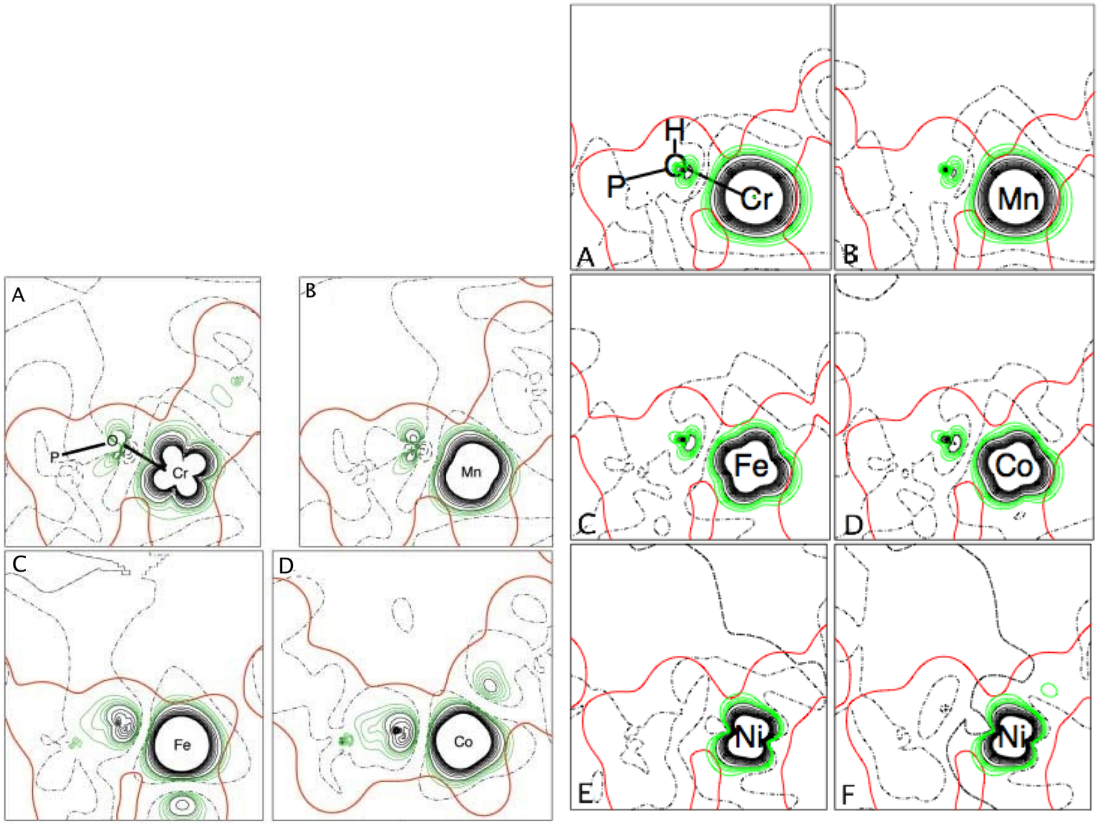

(a) (b)

Figure 2.3: Electron spin density maps for (a) the isovalent 3+ ions and for the (b) low-valent 2+ transition metal ions in AlPO-34. The black and green lines represent the spin density, plotted between -0.05 and +0.05 au at linear steps of 0.005 au (black), and between 0.001 and 0.005au at linear steps of 0.001au (green). Continuous and dashed lines refer to positive and negative spin density, respectively. The continuous line is the isodensity level of 0.01 au calculated from the total electronic density, and represents the effective size of framework. On the left, the substitutional ions are Cr^{3+} (A), Mn^{3+} (B), Fe^{3+} (C), Co^{3+} (D) and on the right, the substitutional ions are Cr^{2+} (A), Mn^{2+} (B), Fe^{2+} (C), Co^{2+} (D), and Ni^{2+} (E). The plot (F) refers to the solution for Ni^{2+}, calculated with the B3LYP Hamiltonian [64].

half filled *d* AOs of the TM. Regarding the Lewis acidity of open-shell TM ions in the high-spin state, half filled *d* AOs (that is, with electronic configuration d^3-d^4), and ions with *d* AOs that are at least half filled (with electronic configuration d^5-d^8) behave in a different way. In the former case the spin density represents the AOs which are less influenced by Lewis acidity: they are half filled, while the other *d* orbitals are empty and therefore stronger Lewis acids. In the latter case, the spin density represents the *d* orbitals responsible for the Lewis acidity: they are half filled, while the remaining levels are all occupied by two electrons, and hence inactive towards Lewis acidity. From figure 2.3 it was observed that the orientation and the radial extent of the spin density along with the Pauli repulsion area (thicker line) depend on the electronic configuration of the TM dopant. A molecule inserted in the Ni-doped AlPO will be subject to Pauli repulsion before interacting effectively with the Lewis active orbitals of Ni ion, while this is not the case for the other dopants. This explains effectively the origin of the Lewis acidity in Mn, Fe, and Co-doped materials and its absence in the Ni-doped in agreement with the experimental results of [76].

Finally, it was shown [77] that the TM ions which are located in open regions of AlPO frameworks, where the space behind the dopant and the protonated oxygen is not protected by other ions, are expected to be more Lewis active i.e. single walls between large cages like in AlPO-34. Alternatively, when the TM and the protonated oxygen are not approachable from behind by adsorbed molecules, they will be less Lewis active, i.e. one-dimensional channels made of "double-wall" building units, like in AlPO-5 and AlPO-11 structures [77].

In general, Lewis acid-base interaction between the adsorbed molecules and the doped AlPOs requires the presence of empty *d* orbitals on the TM dopant oriented in a perpendicular direction to the framework structure.

2.4.3 Redox activity of transition metal ions in microporous AlPOs

Finding a catalyst with the right compromise between redox activity and selectivity is still an open question. TM-doped AlPOs are known to be active heterogeneous catalysts for the selective oxidation of hydrocarbons [54] , but different TM ions exhibit different activity to the catalysts [16, 24, 78].

Corà *et al.* calculated the redox energies of the M^{II}/M^{III} couples for Cr, Mn, Fe and Co in the AlPO-34 framework. Hydrogen was used as reductant according to the below equation:

$$M^{III}AlPO-34+\frac{1}{2}H_2 \xrightarrow{\Delta E^{III/II}} M^{II}HAlPO-34 \tag{2.1}$$

According to their results, Fe is the most stable in 3+ oxidation state when inserted in the AlPO framework, while for Mn the most stable is 2+. Cr and Co can easily change oxidation state and thus they have intermediate behaviour. In addition, the crystalline environment of the redox active ions is a very important factor in determining their redox potential and the redox energy for the same ion can change substantially as a function of its chemical environment.

In general, it was suggested that in each redox catalytic cycle in MeAlPOs there are at least two elementary reaction steps where in the first M affects oxidation by reducing its oxidation state from 3+ to 2+ and a second one involving the reoxidation from 2+ to 3+ oxidation state. The relative performance of the M^{II}/M^{III} couple will depend on which elementary step is rate determining for the catalytic reaction and in the relevant experimental conditions. The relative rate of each elementary step can be affected by the framework type, the temperature and the partial pressures of reagents and products and thus, the relative activity of Fe, Co, Mn and Cr-AlPO catalysts can be also influenced. Assuming that the rate determining step in the catalytic cycle is the one where the oxidation state is reduced from 3+ to 2+, they predicted that the relative activity decrease in the order MnAlPO>CoAlPO>CrAlPO>FeAlPO. An example regarding this trend was reported by Thomas *et al.* [16] showing that MnAlPO and

CoAlPO are highly active in the regioselective oxidation of linear alkanes by molecular oxygen when the reduction of M^{3+} to M^{2+} takes place. The opposite trend was identified in the catalytic step involving the reoxidation of the M dopant with a report [24] presenting that FeAlPOs shows catalytic activity superior to that of the Co and Mn-substituted analogues for the selective oxidation of cyclohexane in air. According to the authors, these results are due to the fact that only a small proportion of the Co^{2+} and Mn^{2+} ions that are isomorphously embedded in the AlPO-36, AlPO-11 and AlPO-5 structures change their oxidation state to +3 by O_2 or dry air, in contrast to Fe^{2+} which is completely converted into Fe^{3+}.

In the case where the two elementary steps described above have comparable rate, CrAPO and CoAPO catalysts are expected to be the most active, as Cr and Co are the ions that can more easily change their oxidation state in either direction. Luna *et al.* [78] investigated experimentally the redox activity of several dopants in the AlPO VPI-5 framework when oxidation of cyclohexane takes place under mild conditions, showing that CrAPO has the highest activity while MnAPO has the lowest. From references [24] and [78] it has been suggested that the cyclohexane oxidation proceeds via different mechanisms in small and large pore AlPO catalysts. The size of pores is smaller in the framework used in [24] than in VPI-5 framework used in [78]. In small-pore AlPOs, such as AlPO-34, there are kinetic constraints and the alkane can only "crawl", yielding an effective contact with the active site. As a result, we expect kinetic control of the reaction in small-pore catalysts like AlPO-34, and thermodynamic control in large pore materials like the AlPO VPI-5, explaining the different relative activity of the same dopant ions in different microporous materials.

2.5 Previous investigations on redox reactions using TM-doped AlPOs

The use of catalysis is widespread in the chemical industry, not only to optimise economic operations and minimise their environmental impact, but also as a way to control selectivity in reactions where the required products are not the thermodynamically stable combination of the reagent molecules in the gas phase. In general, selectivity can be achieved with the introduction of stereochemical constraints in the catalyst region surrounding the active site. In aluminophosphate catalysts, the fine tuning of the pore diameter allows for shape-selectivity as the reaction taking place can be affected by the constraint environment and thus, the terminal C atom of a n-alkane could approach the catalytically active site [16]. In nature, most biological conversions involving dioxygen require enzymatic catalysis, for example in redox metallo-enzymes that catalyze shape- and regio-selectively the oxidation of hydrocarbons [79–81]. An aim of contemporary catalysis is to replicate the selectivity issues of enzymes. A first approach is to design new molecular-sieve solids containing active sites which are all in an identical chemical and structural environment, and this is the concept of Single-Site-Heterogeneous Catalysts (SSHCs), as discussed by Thomas *et al.* [82].

There is extensive research on the performance of microporous aluminophosphate catalysts in different types of oxidations [27]. Microporous AlPOs enable a synergic effect obtained by the redox-activity of the TM cations in low-coordination environments and the unique spatial constraints imposed by the molecular dimensions and crystalline nature of their porous framework [15, 16, 24, 30, 38], making them efficient and selective catalysts for a wide range of oxidation reactions. Some previous studies on industrially fundamental selective oxidations are presented in this section.

2.5.1 Baeyer Villiger oxidation of ketones to lactones

In 1991 Yamada *et al.* [83] used homogeneous (TM based) catalysts with molecular oxygen and a sacrificial aldehyde to epoxidise olefins. Raja *et al.* [29, 37] employed similar conditions but considering the redox properties, they used three different structures of potential heterogeneous catalysts to epoxidise alkenes or to convert ketones to lactones at low temperature. The catalysts used were CoAlPO-36, MnAlPO-36, CoAlPO-5, MnAlPO-5, CoAlPO-18 and MnAlPO-18 which all contain small amounts (up to 4%) of either manganese or cobalt redox cations. Figure 2.4 shows an example of Baeyer Villiger oxidation and represents the AlPO-36 catalyst where one of the aluminium sites is occupied by manganese. The structure has well-defined oval-shaped channels. Bulky sacrificial benzaldehyde molecule accesses the large internal surfaces of AlPO catalyst and is converted in the presence of oxygen to the corresponding peroxy acid. This peroxy acid is then involved in a nucleophilic attack at the carbonyl carbon, leading to the production of lactone.

2.5.2 Epoxidation of alkenes

Further extension of Raja's work on Baeyer Villiger oxidation of ketones to lactones suggested selectivities for the epoxidation of alkenes using framework substituted transition metal ions such as Mn and Co, in microporous aluminophosphate (MAlPO-36) catalysts [33]. Benzaldehyde molecules may freely enter the large internal surfaces of both MAlPO-36 and MAlPO-5 catalysts to firstly generate the PhCO· and then the PhCOOO· radicals which, from the sequence of steps shown below lead to the formation of benzoic acid and cyclohexene oxide.

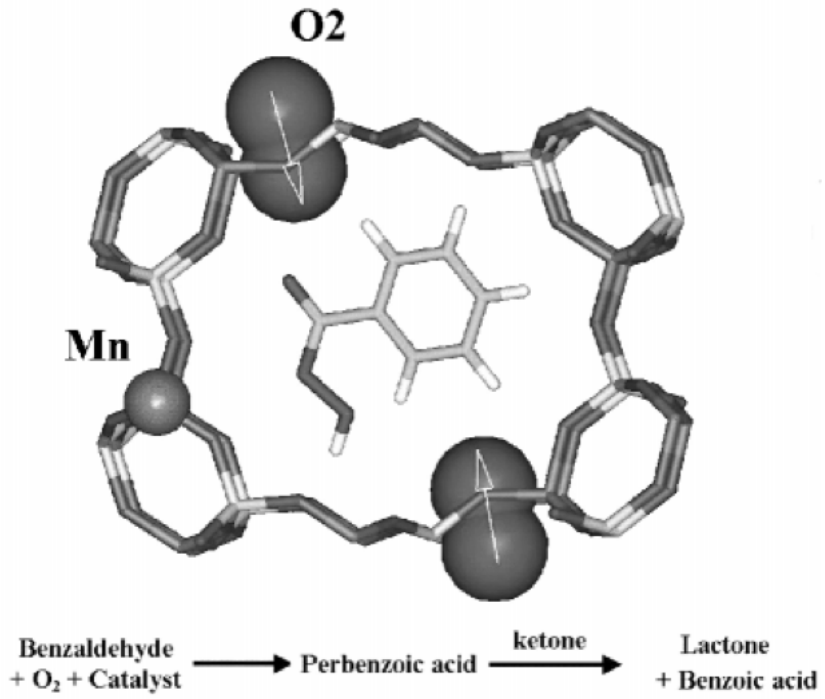

Figure 2.4: Representation of the AlPO-36 catalyst where manganese ions replace Al^{III} ions. Conversion of benzaldehyde to the perbenzoic acid intermediate affected by both dioxygen and Mn^{III} ions [37].

$$PhCHO + Mn^{III} \rightarrow PhCO\cdot + H^{+} + Mn^{I}I \tag{2.2}$$

$$PhCO\cdot + O_2 \rightarrow PhCOOO\cdot \tag{2.3}$$

$$PhCOOO\cdot + PhCHO \rightarrow PhCOOOH + PhCO\cdot \tag{2.4}$$

$$PhCOOOH + PhCHO \rightarrow 2PhCOOOH \tag{2.5}$$

$$PhCOOO\cdot + C_6H_{10} \rightarrow C_6H_{10}O + PhCOO\cdot \tag{2.6}$$

$$PhCOOOH + C_6H_{10} \rightarrow C_6H_{10}O + PhCOOH \tag{2.7}$$

$$PhCOO\cdot + PhCHO \rightarrow PhCOOH + PhCO\cdot \tag{2.8}$$

$$PhCOOH + Mn^{II} \rightarrow PhCOO\cdot + OH^{-} + Mn^{III} \tag{2.9}$$

The experimental conditions chosen for this study, from the temperature and pressure to the amount of catalyst and the concentration of catalytically active redox ions, have not led to maximum conversion and selectivity. The 50% of the Mn^{II} (or Co^{II}) has converted to the Mn^{III} (or Co^{III}) but the tetrahedral co-ordination of the transition metal ions does not change within the framework of AlPO catalyst.

2.5.3 Aerobic terminal oxidation of linear alkanes

Raja *et al.* [28] have designed an heterogeneous catalyst that selectively converts dodecane in dry air at temperatures up to 550^{o}C. The 4% of Al^{III} ions in the AlPO-18 catalyst has been replaced by Mn^{II} ions. The Mn^{II} ions are all converted to the +3 oxidation state remaining securely in tetrahedral co-ordination within the microporous aluminophosphate AlPO framework.The terminal methyl group (C1) and the secondary (C2) of the dodecane are much more closer to the tetrahedral framework site than C3, C4 and C5 groups. This shows that the Mn^{III} ions in the framework of the AlPO-18 cage, together with intercage molecular oxygen, affect significantly more the C1 and C2 methyl groups than the rest of carbons on the dodecane backbone.

Parallel work at CoAlPO-18 [24] catalyst has also shown that this catalyst preferentially activates the terminal and the secondary methyl groups of n-hexane. A bound hexane (or any other linear alkane) molecule, with its slightly bent end, approach easier the active sites, which selectively favour oxidation at the terminal carbon atoms.

Figure 2.5 represents the configuration adopted by n-dodecane and n-hexane at 0K after energy minimisation, which were derived from a calculation [84] that combines Monte Carlo, molecular dynamics, and docking procedures.

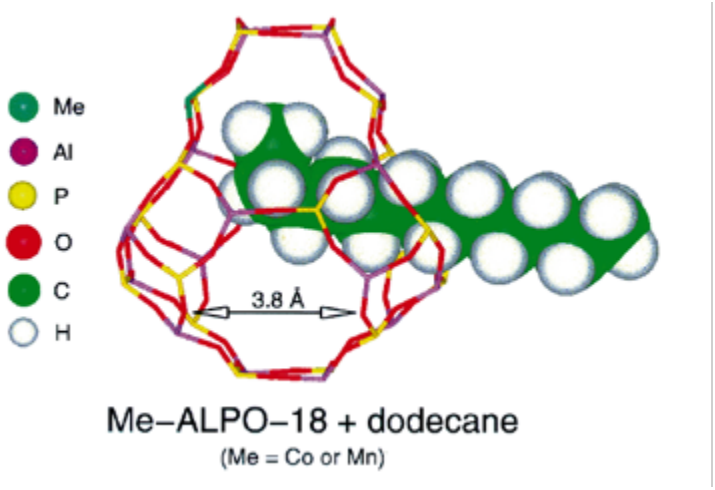

(a)

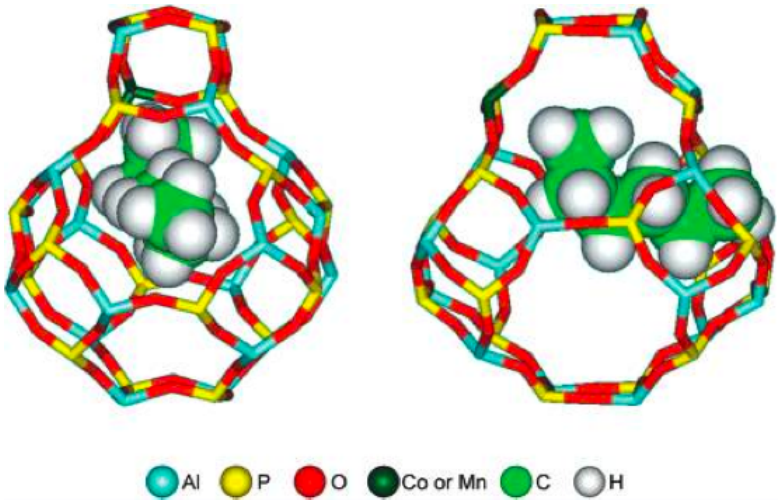

(b)

Figure 2.5: Energy-minimised configuration adopted by (a)n-dodecane [28] and (b)n-hexane at 0 K inside an AlPO-18 framework [27].

2.5.4 Selective oxidation of cyclohexane in air

The conversion of cyclohexane into cyclohexanol is one of the main target reactions in the research area of selective oxidation of alkanes due to the industrial importance of the latter compound as a feedstock in several processes such as the production of nylon from ε-caprolactam and adipic acid [85]. Sankar *et al.* [62] have described a systematic catalytic study of selective oxidation of cyclohexane to yield cyclohexanol, cyclohex-

anone and adipic acid, using molecular oxygen as the oxidant at moderate temperature (403 K) and pressure. They have used four cobalt containing aluminophosphate catalysts, CoAlPO-5, CoAlPO-36, CoAlPO-11 and CoAlPO-18, which differ in the amount of oxidisable cobalt centres and have investigated which of them appears to have the best catalytic activity. The results show that CoAlPO-36 is the significantly the most active catalyst compared to the other three catalysts. Figure 2.6 plots the kinetics for the oxidation of cyclohexane using CoAlPO-36 catalyst at 403 K. After the initial period of 120 min, the major products are cyclohexanol and cyclohexanone. As the time continues beyond the 8 hours, sufficient amounts of adipic acid appear in the mixture of products. Re-use of the CoAlPO-36 catalyst did have a negative effect on the catalytic activity. Further studies on the selective oxidation of cyclohexane in air have shown that the FeAlPO-5 catalyst has also exceptionally good activity.

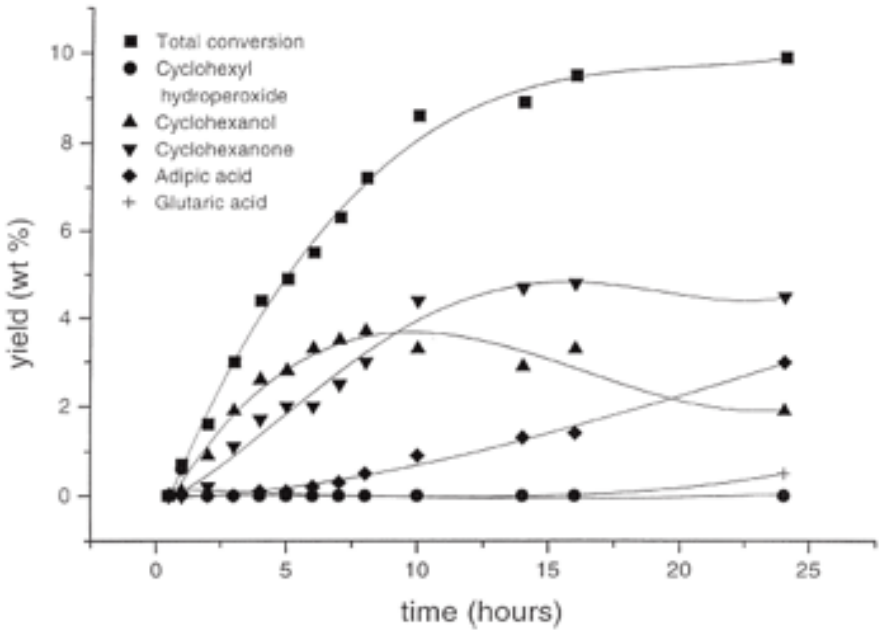

Figure 2.6: Plot representing the typical kinetics for the oxidation of cyclohexane with CoAlPO-36 as the catalyst [62].

2.6 AlPOs examined in this work

Transition metal doped aluminophosphates are of great importance due to their catalytic efficiency and so far, we have presented a thorough literature review where several fundamental topics of these heterogeneous catalysts have been examined. In the following chapters we will focus on two different Mn-doped AlPO frameworks, the MnAlPO-5 and MnAlPO-34. We have employed the Mn doped AFI and CHA structures since both systems have been widely investigated experimentally and computationally.

2.6.1 Mn-doped AlPO-5

AlPO-5 framework comprised one-dimensional, non-interconnected, 12-membered ring (MR) channels whose walls are formed by 6-MR windows. These large channels are surrounded by smaller 6- and 4-MR voids, which are too small to permit the diffusion of small molecules. The main channels of this structure type are nearly circular and have a diameter of 0.73 nm (figure 2.10a).

Moden *et al.* [35] have studied the cyclohexane oxidation reaction pathways and elementary steps on MnAPO-5 catalysts with kinetic and isotopic measurements. The elementary steps for cyclohexane (RH) oxidation are are presented below:

$$H\cdot + ROOH \rightarrow RO\cdot + H_2O \tag{2.10}$$

$$RO\cdot + R'H \rightarrow R'\cdot + ROH \tag{2.11}$$

$$R'\cdot + O_2 \rightarrow R'OO\cdot \tag{2.12}$$

$$R'OO\cdot \rightarrow OH\cdot + R'(-H) = O \tag{2.13}$$

$$OH\cdot + RH \rightarrow H\cdot + ROH \tag{2.14}$$

$$R'OO\cdot + R'H \rightarrow R'\cdot + R'OOH \tag{2.15}$$

Figure 2.7 shows the catalytic cycle. As it is shown, ROOH is a reactive intermediate in ROH and R-(-H)=O formation. UV-visible spectroscopy was used to determine the oxidation state of Mn before and after catalytic reactions and it was observed that the most abundant surface intermediate (MASI) is Mn^{2+} during steady state catalysis. Taken this assumption into consideration, it was concluded that the reaction of ROOH with divalent Mn is a kinetically relevant step. Among others, extensive spectroscopic and isotopic labelling techniques were used in order to determine the main reaction intermediates.

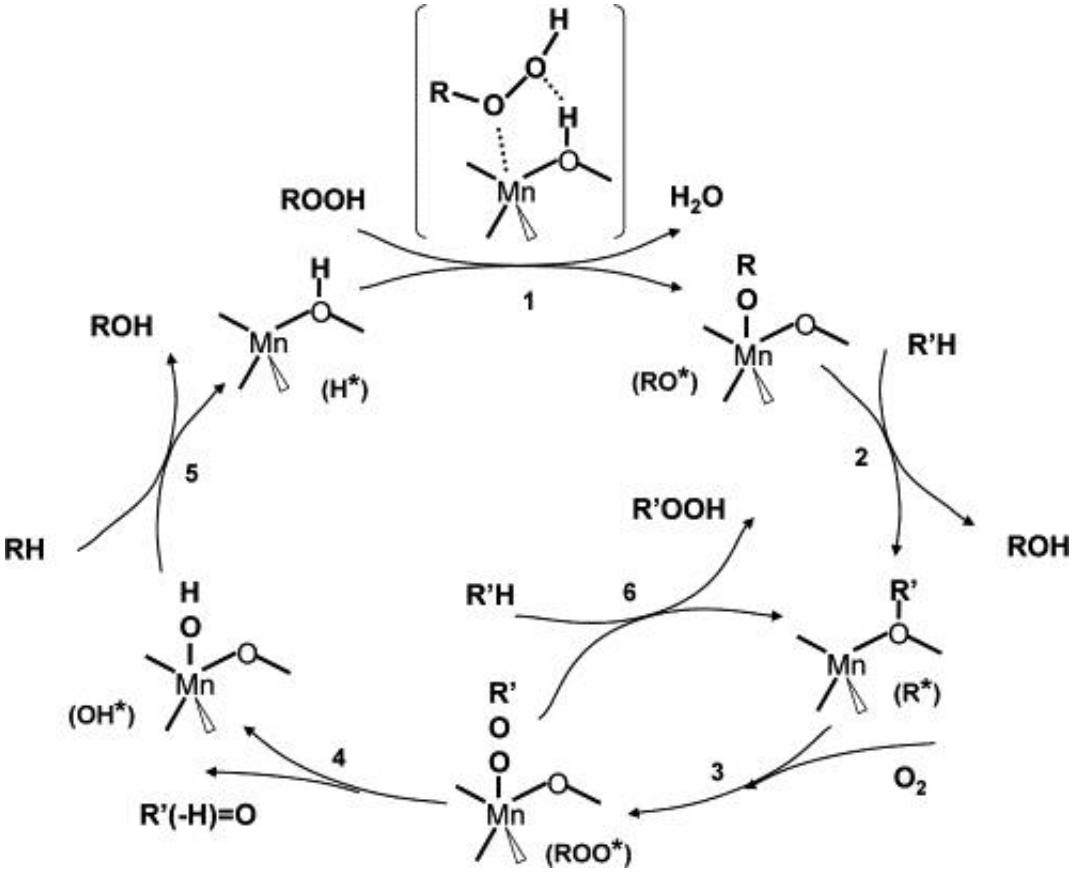

Figure 2.7: Catalytic cycle of cyclohexane oxidation on MnAPO-5 catalyst [35].

This reaction scheme guided the computational studies of Gómez Hortigüela *et al* [39, 40]. They successfully applied state of the art electronic structure computational methods based on hybrid exchange Density Functional Theory (DFT) in order to investigate the aerobic oxidation of hydrocarbons catalysed by Mn-AlPO5. The whole

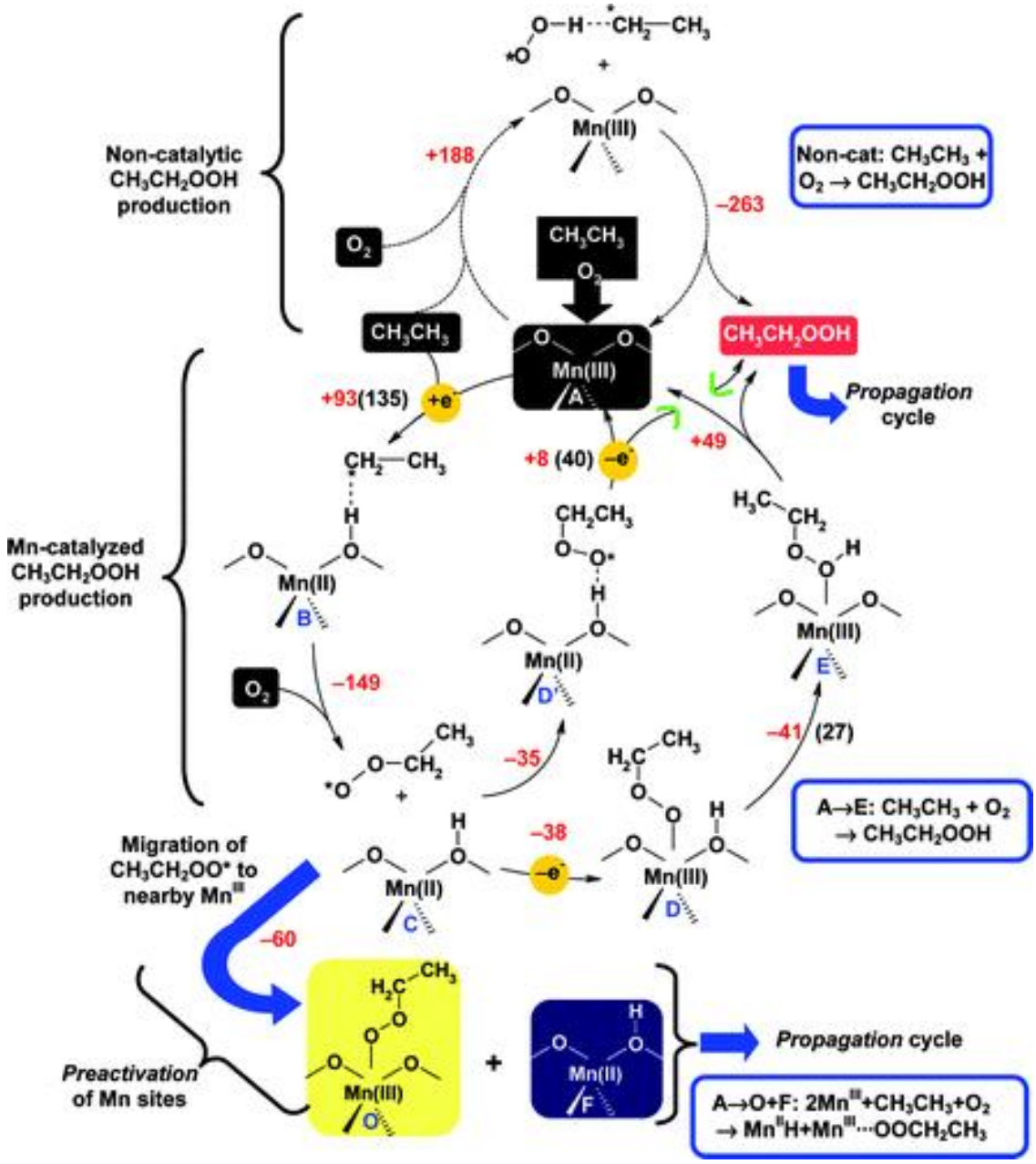

Figure 2.8: Preactivation mechanism. The black background shows initial catalyst and reactant molecules, whilst the red background presents the hydroperoxide intermediate. Yellow and blue backgrounds indicate intermediates produced and necessary to initiate subsequent reaction. Enthalpies are presented with red font colour for each elementary step and activation energies (in kJ/mol) with black [39].

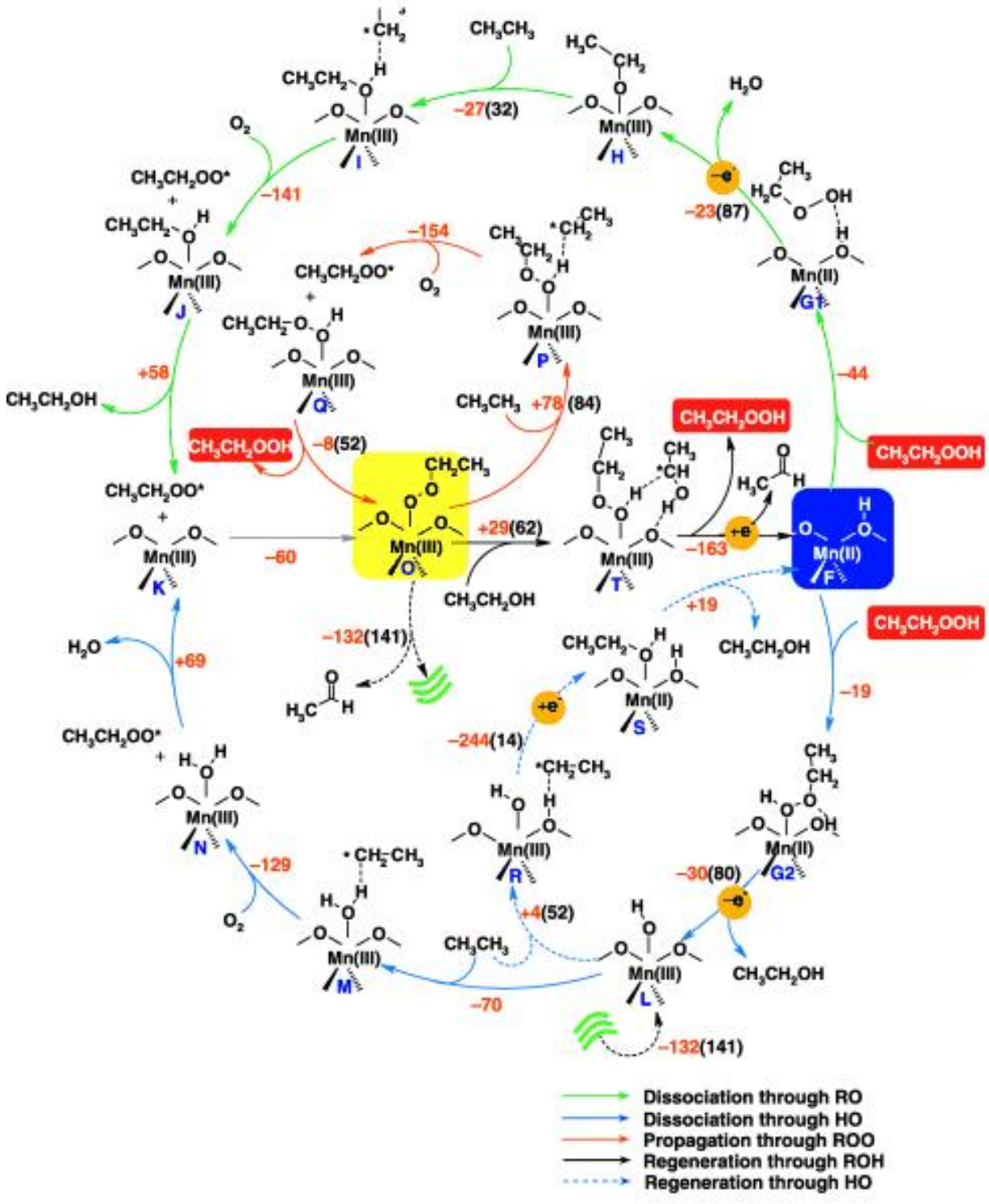

Figure 2.9: Propagation mechanism. Background colours and energies are presented as in figure 2.8 [42].

catalytic cycle was unraveled [39–43] in agreement and complementing the data available from experiment.

Ethane was used as the model hydrocarbon because its simplicity allows the use of expensive periodic DFT techniques. The Mn redox activity, particularly its reversible transfer between 2+ and 3+ oxidations states, and the tetrahedral coordination of Mn within the microporous AlPO framework are both important factors in the catalytic efficiency of MnAlPOs. The role of both Mn^{II} and Mn^{III} in the reaction mechanism is significant: Mn^{III} sites produce the alkyl hydroperoxide which can only be transformed by Mn^{II} into alcohol, aldehyde and acid. The computational study demonstrated the requirement of an initial preactivation step (figure 2.8 [39]) to yield reduced Mn^{II} sites which are able to decompose the hydroperoxide intermediates. In the case of Mn^{II}-doped AlPOs, Mn^{II} is reduced by the hydrocarbon substrate itself via radical H· abstraction. A propagation cycle follows (figure 2.9 [40]) where Mn^{III} -OOR leads to production of ROOH, whilst Mn^{II} transforms this ROOH into the final oxidative products through two different pathways, alkoxy- or hydroxy- radical like intermediates.

In particular, the catalytic cycle starts with a preactivation step (A→B in figure 2.8) with a high activation energy of 135 kJ/mol, where Mn^{III} abstracts a H from the ethane yielding a reduced Mn^{II} site and an ethyl radical [39]. The alkyl radicals R· are subsequently stabilised by the addition of O_2 (B→C) yielding peroxo radicals ROO· that desorb from Mn^{II} and form a complex with a new Mn^{III} site (C→D).

The propagation phase of the catalytic reaction proceeds from Mn^{II} (F) and ROO·(Mn^{III}) (O). The latter complexes are responsible for the production of the hydroperoxide intermediate (ROOH) through H abstraction from hydrocarbon molecules, yielding in turn alkyl radicals R that undergo again steps B→C and C→D. This subcycle provides a catalytic source of ROOH.

The decomposition of the ROOH intermediate can only occur on reduced Mn^{II} sites (F→G1 and F→G2) [41] and has two alternative mechanistic pathways depending on the stereochemistry of the adsorption of ROOH on Mn^{II}, yielding either RO·(Mn^{III})

and H_2O (G1) or HO·(Mn^{III}) and ROH (G2) both resulting in the oxidation of Mn. Subsequent propagation reactions take place from these Mn^{III} complexes via H abstraction from new ethane molecules by the radical O atom of RO·(Mn^{III}) or HO·(Mn^{III}) (H→I and L→M) [42], to yield the primary oxidative products (ROH, H_2O, and ROOH). In order to close the reaction cycle the reduction of the Mn^{III} sites must occur; this step is referred to as regeneration [43]. The most favoured regeneration route takes place through a mechanism consisting of two H abstractions from the alcohol ROH to give the aldehyde/ketone (R(=O)) and Mn^{II}(H) sites (O→T→F).

Characteristic in this reaction cycle is that whenever a new hydrocarbon radical is formed it is stabilised by addition of O2; this step is always highly exothermic and barrierless and it is the main thermodynamic driving force for the reaction to proceed. At the high O_2 partial pressure that these catalytic oxidations usually operate at, we can expect the O_2 addition to occur promptly upon formation of a new C-based radical.

In general, there is a very good agreement between the computational results of this mechanism and the experimental observations available in the literature [31, 35], confirming both the excellent performance of the computational methodology (analysed in detail in Chapter 3) and the validity of the mechanism proposed.

2.6.2 Mn-doped AlPO-34

AlPO-34 is closely related to the zeolitic aluminosilicate chabazite which makes it suitable for heterogeneous catalysis due to its pore dimensions and shape. As in AlPO-5, Al^{3+} ions can be substituted by four-coordinated Mn^{3+} ions. Figure 2.10b illustrates the AlPO-34 structure. The unit cell contains 36 ions with the chemical formula ($Al_6P_6O_{24}$). The 3D-channels are controlled by 8-membered rings, with pore diameter of 0.38 nm [86], non-circular, whose walls are formed by 6-MR or 4-MR of AlO_4 tetrahedra. The rings form two ellipsoidal cages per unit cell, the cages sharing 6-MR. Due to its small pores and its small unit cell, AlPO-34 has been extensively studied experimentally and theoretically. As already presented in previous section, Corà *et*

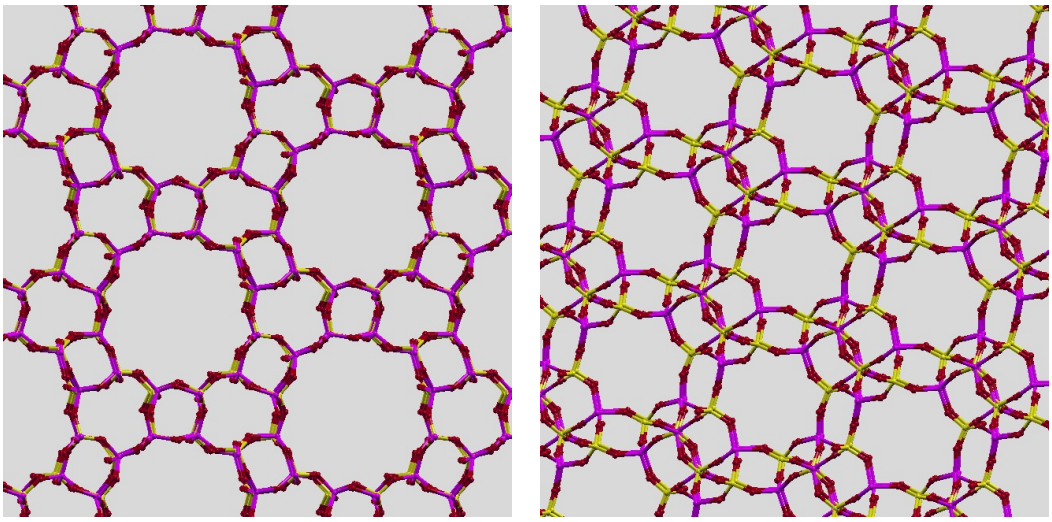

(a) (b)

Figure 2.10: Representation of the pore structures of (a) AlPO-5 (AFI) and (b) AlPO-34 (CHA) structure (pore apertures are respectively 7.3 Å and 3.8 Å).

al. have thoroughly investigated the framework stability and catalytic activity of doped AlPO-34 [64].

Our particular interest on AlPO-34 arises from the fact that it is an analogous framework to AlPO-18, as both structures have pores similar to those of the zeotypic analogue of the aluminosilicate mineral chabazite [86]. Previous studies on MAlPO-18 molecular sieves (M= Mn^{2+}, Zn^{2+}, Mg^{2+}, Co^{2+} etc.) have shown that they are powerful solid acid catalysts for a series of low-temperature reactions [27].

2.6.3 Challenges

Some of the challenges stemming from this thorough literature review will be addressed in the next Chapters. In particular, this thesis focuses on two representative steps of the catalytic cycle obtained from the work of Gómez Hortigüela *et al.* [39–43]. The first is the abstraction of H from ethane in the preactivation phase (reaction step $A \rightarrow B$ in figure 2.8), which involves a reduction of the Mn^{III} site to Mn^{II} and the formation of an ethyl radical. The second step comes from the propagation phase of the catalytic cycle

where Mn does not change oxidation state (reaction step $H \rightarrow I$ in figure 2.9) where the radical-like nature of this RO· ligand allows a H-transfer from a new hydrocarbon molecule in order to saturate the ethoxo radical RO· by forming an ethanol molecule (ROH). By examining these two key reaction steps in detail, we gain valuable additional understanding of the fundamental electronic processes.

In Chapter 6, we would like to investigate one of the most pressing open questions in the Me-AlPO literature regarding their role in the regioselective and shape-selective oxyfunctionalization of alkanes with molecular oxygen. We would like to discriminate the reactivity of primary and secondary carbon atoms of linear alkanes to oxidation and examine if the smaller pores of Mn-doped AlPO-34 can impose any steric constraints when a catalytic reaction takes place in comparison to the larger pores of MnAlPO-5. Thus, we focus again on the two elementary steps examined before to study the aerobic oxidation of ethane with Mn-doped AlPO-34 as catalyst, and then by changing our substrate from ethane to propane and hexane we examine selectivity issues.

Chapter 3

Computational details and methods

3.1 Introduction

Computer modelling techniques, as already discussed, enable the study of the structural and electronic properties of a system and effectively complements the experimental investigations. It provides atomic-level insight in solid-state and materials sciences and thus, the development of modelling is of great value for the investigation of the structural chemistry of complex materials [12]. As there is an increased industrial demand for designing new materials whose electronic and structural properties are suitable for specific applications, general and reliable *ab-initio* electronic structure techniques are required. These methods have been developed through the decades and are now an established tool for research in solid-state chemistry, condensed matter physics and materials science, where they can be used to interpret available experimental data as well as to direct new experimental attempts.

There is a wide range of modelling techniques applied in complex materials [87], from quantum mechanical (QM) methods to molecular mechanical (MM) methods based on force-fields, and interatomic potentials (IP) [88]. QM methods focus on the numerical computation of molecular electronic structures either at *ab initio* or semi-empirical level. *Ab initio* methods are based entirely on quantum mechanics and basic physical constants, while semi-empirical methods only treat the valence electrons ex-

plicitly and employ additional empirical parameters to make up for this lack of explicit detail in all of the electrons. *Ab initio* methods are used for a broad range of systems and are more rigorous compared to semi-empirical methods; however, the latter are less demanding computationally. QM methods account for the Schrödinger equation at some level of approximation and address Hartree-Fock methods and density functional theory (DFT) techniques, while considering part of the electrons in the system either at semi-empirical level or at *ab initio* level. There is some overlap between the approximations used in HF and DFT (e.g. Born-Oppenheimer approximation) but the two methods differ in the way they treat the electron-electron interaction, as we will show in the next sections. Alternatively to QM methods, interatomic potential methods do not attempt to solve the Schrödinger equation but they depend primarily on the Born-Oppenheimer approximation, which allows to write the potential energy (V) of the system as a function of the nuclear coordinates [89].

Modelling of aluminophosphates makes use of both techniques in order to develop a detailed understanding of structures and processes at the atomic and molecular level. In general, molecular modelling tools are applied in AlPOs and there is a range of possible applications from framework structure modelling and modelling of sorption and diffusion, to modelling of template-host interactions and investigating defect and surface chemistry. IP have been applied by Corà *et al.* [64] to identify which factors are important to define the structural stability of AlPOs as well as to study the site-ordering of dopant ions in AlPOs by investigating the structure and energy of trivalent substitutional ions of different size which replace an Al ion in the framework. IP techniques have been also used to evaluate the stability of these structures and the feasibility of their synthesis [90]. QM methods focus on two major issues in AlPOs which are, finding structural details that are difficult to access from experiment and also calculating the reaction energies and barriers.

This thesis focuses on catalysis involving redox reactions of TM ions, and hence the identification of transition state is very important. In particular, the search for TS

structures is one of the most interesting for two reasons; first, transition state searches can be used as starting point for reaction mechanisms and second, although femtosecond spectroscopy is able to detect reaction intermediates with extreme short life, there is no experimental procedure which allows the direct observation of these structures. The recent studies of Gómez Hortigüela *et al.* [39, 40], where a whole catalytic mechanism was unraveled, establishes the significancy of computer modelling. Moreover, since in AlPO catalysts both the framework stability and the activation of the framework with TM dopant ions are crucial, modelling can provide accurate information on the structure and chemistry of the active sites.

In this Chapter we firstly review some of the fundamental aspects of electronic structure theory in order to discuss afterwards the DFT method and the approximations of electron-correlation energy. Also, we make reference to the self-interaction error (SIE) arising from DFT approximations and how this is crucial on systems with well localised *d* electrons. Finally we present the methodology used for this thesis, where we examine the performance of GGA and hybrid exchange functionals within density functional theory in representing the energetics of particular redox reactions.

3.2 Foundations of Quantum Chemistry

In this section section we introduce the Schrödinger equation with the molecular Hamilton operator and we present the Hartree-Fock method [87].

3.2.1 The Schrödinger equation

Most quantum chemical approachers aim to solve approximately the time-dependent, non relativistic Schrödinger equation for a multi-particle system consisting of M nuclei and N electrons:

$$\hat{H}\Psi(r_1, ..., r_N, R_1, ...R_M) = E\Psi(r_1, ..., r_N, R_1, ...R_M) \tag{3.1}$$

where $\hat{H}$ is the Hamilton operator of the system, E is the energy of the eigenstate and Ψ is the wavefunction of the eigenstate [91]. The wavefunction Ψ depends on the positions of both the electrons $(r_1, ..., r_N)$ and the nuclei $(R_1, ..., R_N)$ in the molecular system. The Hamiltonian is $\hat{H}$ is a differential operator and represents the total energy:

$$\hat{H} = \hat{T}_e + \hat{T}_n + \hat{V}_{ee} + \hat{V}_{en} + \hat{V}_{nn} \tag{3.2}$$

These first two terms describe the kinetic energy of the electrons and nuclei, respectively. The kinetic energy of the electrons $\hat{T}_e$ and nuclei $\hat{T}_n$ are defined as:

$$\hat{T}_e = -\frac{1}{2}\sum_{i=1}^{N}\nabla_i^2 \tag{3.3}$$

$$\hat{T}_n = -\frac{1}{2}\sum_{A=1}^{M}\frac{1}{M_A}\nabla_A^2 \tag{3.4}$$

where M_A is the mass of nucleus A in multiples of the mass of an electron. The Laplacian operator ∇_q^2 is defined as the sum of differential operators in cartesian coordinates:

$$\nabla_q^2 = \frac{\vartheta^2}{\vartheta x_q^2} + \frac{\vartheta^2}{\vartheta y_q^2} + \frac{\vartheta^2}{\vartheta z_q^2} \tag{3.5}$$

These kinetic terms are combined with the remaining three terms for the potential energy arising from the repulsive Coulombic interaction between two electrons $\hat{V}_{ee}$ and

two nuclei $\hat{V}_{nn}$, and the attractive electrostatic interaction between the nuclei and the electrons $\hat{V}_{en}$, defined as:

$$\hat{V}_{ee} = \sum_{i=1}^{N} \sum_{j>i}^{N} \frac{1}{r_{ij}} \tag{3.6}$$

$$\hat{V}_{nn} = \sum_{A=1}^{M} \sum_{B>A}^{M} \frac{Z_A Z_B}{R_{AB}} \tag{3.7}$$

$$\hat{V}_{en} = \sum_{i=1}^{N} \sum_{A=1}^{M} \frac{Z_A}{r_{iA}} \tag{3.8}$$

where A and B run over the M nuclei while i and j denote the N electrons in the system.

Considering the differences between the masses of nuclei and electrons, as the mass of the proton is three orders of magnitude greater than the mass of an electron, it is obvious that the nuclei move much slower than the electrons. Thus, it is reasonable to assume that the electrons move in the field of fixed nuclei. This is the Born-Oppenheimer approximation [92]. Since the nuclei are treated as fixed point charges with zero kinetic energy, the potential energy due to nucleus-nucleus repulsion is merely a constant. Thus, with the removal of the nuclear components, the complete Hamiltonian described in equation 3.2 reduces to the electronic hamiltonian as shown below:

$$\hat{H}_{el} = \hat{T}_e + \hat{V}_{ee} + \hat{V}_{en} \tag{3.9}$$

The solution of the Schrödinger equation for electrons becomes:

$$\hat{H}_{el} \Psi_{elec} = E_{elec} \Psi_{elec} \tag{3.10}$$

Ψ_{elec} depends on the electron coordinates, while the nuclear coordinates do not explicitly appear in Ψ_{elec} but they enter only parametrically. The total energy is then the sum of the electron energies and the nuclear repulsion term.

$$E_{tot} = E_{elec} + E_{nuc} \tag{3.11}$$

3.2.2 The Hartree-Fock method

Hartree-Fock theory is fundamental to much of electronic structure theory. It is the basis of molecular orbital (MO) theory, which says that each electron's motion can be described by a single-particle function (orbital) which does not depend explicitly on the instantaneous motions of the other electrons.

The Hartree-Fock equation may be written:

$$\hat{F}(1)\Phi_i(1) = \varepsilon_i\Phi_i(1) \tag{3.12}$$

where $\hat{F}$ is the Fock operator, ε_i is the energy of electron i, and $\Phi_i(1)$ is the function describing electron i in orbital 1. The above equation can be written more completely:

$$\hat{F}(1)\Phi_i(1) = -\left(\frac{1}{2}\nabla_i^2\right)\Phi_i(1) - \sum\left(\frac{Z_A}{r_{1A}}\right)\Phi_i(1) + \sum_{j\neq i} J_j(1)\Phi_i(1) + \sum_{j\neq i} K_j(1)\Phi_i(1) \tag{3.13}$$

The first term is the kinetic energy term, while the second term represents the coulombic term for the interaction between the electron and nucleus A. The third term is the Coulomb operator ($\hat{J}$) because it leads to energy terms corresponding to the electrostatic repulsion between an electron in orbital $\Phi_i(1)$ with electrons in every other orbital, and the last term is called the exchange operator ($\hat{K}$) because it takes into account the modification in the energy due to the effects of spin correlation between electrons of the same spin.

In Hartree-Fock methods the Schrdinger equation is solved directly, with electron positions described exactly; however, the equations neglect more detailed correlations due to many-body interactions. The effects of electronic correlations can not be neglected and as a result the failure of Hartree-Fock theory to successfully incorporate correlation leads to the false prediction that jellium is an insulating rather than a metallic system. Thus, the requirement of a computational method that successfully incorporates the effects of both exchange and correlation has lead to the density functional theory approach.

3.3 Density Functional Theory

Density Functional Theory (DFT) [92, 93] is a theoretical approach which is very popular in modern quantum chemistry. DFT is a computational simple ground-state theory which emphasises the charge density as the relevant physical quantity. It has been proven that DFT is highly successful in describing structural and electronic properties in a wide range of materials, from atoms and molecules to crystals and complex systems. Thus, DFT has become a useful tool in first-principles calculations aimed at describing properties of molecular and condensed matter systems. It will be the main computational method used in the present thesis.

3.3.1 The Hohenberg-Kohn Theorems

Compared with earlier methods based on the Hartree Fock (HF) theory, the great advantage of DFT is that reasonable computational accuracy can be achieved for large molecular complex solids with lower computational cost. In the mid 1960s, Hohenberg and Kohn proved that by determining the electron density of a chemical system we can find all of the ground state electronic properties [17]. An important variational principle is associated with the first Hohenberg-Kohn (HK) theorem:

Theorem 1: "It is impossible that two external potentials $V(\boldsymbol{r})$ and $V'(\boldsymbol{r})$ whose difference $V'(\boldsymbol{r}) - V(\boldsymbol{r})$ is not a constant give rise to the same ground state distribution $\rho(\boldsymbol{r})$."

The proof of the theorem can be found in Appendix A.

The electron density is a measurable observable for all molecules, in contrast to the wavefunction which is only a mathematical construct. The fundamental mathematics of DFT is a functional $F[\rho(r)]$ representing the expectation value of $H_0 = T + U$ (i.e. the total kinetic energy plus the total electron-electron interaction energy) which allows the calculation of the energy of a system of electrons from its electronic density,

ρ(r). For a system with nuclear potential field V(r) and electron density, the energy of the fundamental state is written as:

$$E[\rho(\mathbf{r})] = \int V(\mathbf{r})\rho(\mathbf{r})dr + F[\rho(\mathbf{r})] \tag{3.14}$$

where

$$\int V(\mathbf{r})\rho(\mathbf{r})dr = V_{ne}[\rho(\mathbf{r})] \tag{3.15}$$

Because of theorem 1, specifying the ground-state density $\rho(\mathbf{r})$ uniquely determines the value of F and hence the total ground-state energy. In the second HK theorem the ground state is found by minimising the total energy with respect to $\rho(\mathbf{r})$, subject to fixed total number of electrons N.

Theorem 2: "The ground-state energy for a given external potential $V(\boldsymbol{r})$ is correctly obtained by minimising the functional $E[\rho(\boldsymbol{r})] = \int V(\boldsymbol{r})\rho(\boldsymbol{r})dr + F[\rho(\boldsymbol{r})]$ with respect to $\rho(\boldsymbol{r})$ for fixed $V(\boldsymbol{r})$ and fixed N and the resulting $\rho(\boldsymbol{r})$ gives the correct density distribution of the ground state."

The proof of this Theorem is given in Appendix B.

3.3.2 The Kohn-Sham equations

In 1965, Kohn and Sham [18] tried to deal with density functional problems through a formalism which describes the densities and their subsequent correlations to molecular energies for a non-interacting system of N - electrons [94]:

$$E[\rho(\mathbf{r})] = T_{ni}[\rho(\mathbf{r})] + V_{ne}[\rho(\mathbf{r})] + V_{ee}[\rho(\mathbf{r})] + E_{xc}[\rho(\mathbf{r})] \tag{3.16}$$

where E is the energy, T_{ni} is the kinetic energy of the non-interacting electrons, V_{ne} is the nuclear electron attraction (Coulombic) energy, $V_{ee}[\rho(\mathbf{r})]$ is the classical electrostatic

(Hartree) energy and the final E_{xc} term is the electron electron exchange and correlation energy which contains the correction for the self-interaction energy and the difference between the kinetic energies of the interacting and non-interacting systems. Within an orbital expression for the density, the above equation may be written:

$$E[\rho(\mathbf{r})] = \sum_{i=1}^{N}\langle\psi_i| - \frac{1}{2}\nabla^2 - \sum_{A=1}^{M}\frac{Z_A}{|\mathbf{r}-R_A|} + \frac{1}{2}\int\frac{\rho(\mathbf{r}')}{|\mathbf{r}-\mathbf{r}'|}d(\mathbf{r}')|\psi_i\rangle + E_{xc}[\rho(\mathbf{r})] \quad (3.17)$$

The density for the non-interacting electrons is constructed as a sum over particle indices:

$$\rho(\mathbf{r}) = \sum_{i=1}^{N}|\psi_i|^2 \quad (3.18)$$

Minimisation of the energy functionals leads to the one-electron electron problem

$$h_i^{KS}\psi_i = \varepsilon_i\psi_i \quad (3.19)$$

where ε_i corresponds to the energy of the Kohn-Sham (KS) orbital ψ_i. The KS one-electron operator is defined as

$$h_i^{KS} = -\frac{1}{2}\nabla^2 - \sum_{A=1}^{M}\frac{Z_A}{|\mathbf{r}-R_A|} + \frac{1}{2}\int\frac{\rho(\mathbf{r}')}{|\mathbf{r}-\mathbf{r}'|}d(\mathbf{r}') + V_{xc}(\mathbf{r}) = -\frac{1}{2}\nabla^2 + V_{eff} \quad (3.20)$$

where V_{eff} is the KS effective potential.

The exchange-correlation potential is:

$$V_{xc}(\mathbf{r}) = \frac{\delta E_{xc}[\rho(\mathbf{r})]}{\delta\rho(\mathbf{r})} \quad (3.21)$$

$V_{xc}(\mathbf{r})$ is the so-called functional derivative. As the V_{eff} depends upon $\rho(\mathbf{r})$, the KS equations must be solved self-consistently. The $\rho(\mathbf{r})$ is initially guessed, and then using an approximate form for the functional dependence of exchange correlation energy E_{xc}, V_{eff} is computed. The KS equations are then solved to give an initial estimate of ψ_i in equation 3.19 and by using this set of orbitals the calculated density in equation 3.18 is improved. The self-consistency continues until convergence. The final energy

is calculated from equation 3.16. KS DFT is in principle exact if we know $E_{xc}[\rho(\mathbf{r})]$ exactly. Increasingly accurate approximations have been proposed through the years, and a variety of functionals such as B3LYP, PBE and more, have been developed as approximate forms for the exchange-correlation energy [95, 96].

3.3.3 Exchange-correlation functionals

As already discussed above, the $E_{xc}[\rho(\mathbf{r})]$ includes the non-classical aspects of the electron-electron interaction along with the component of the kinetic energy of the real system different from the fictitious non-interacting system. The exchange effects take place between identical particles and they are due to the Paul Exclusion principle. The exchange energy may be written as function of the single particle orbitals:

$$E_x = -\frac{q^2}{2}\sum_{ij}\int d^3\mathbf{r}\int d^3\mathbf{r}'\frac{\psi_i^*(\mathbf{r})\psi_j^*(\mathbf{r})\psi_i(\mathbf{r})\psi_i(\mathbf{r})}{|\mathbf{r}-\mathbf{r}'|} \tag{3.22}$$

The exchange hole is larger than the correlation, where as "exchange hole" we define the region of reduced probability for encountering a second electron around a given reference electron, because two electrons with the same spin cannot occupy the same point in space. As correlation energy we describe the energy lowering that occurs due to the mutual avoidance of electrons to lower the Coulomb repulsion energy. The "correlation hole" is the region of reduced probability for encountering a second electron around a given reference electron, due to the fact that electrons avoid each other because they have the same charge [97].

3.3.4 Early approximations for exchange correlation energy

Since all terms in equation 3.16 are well defined functionals of $\rho(\mathbf{r})$, the first HK theorem assures us that the exchange-correlation energy $E_{xc}[\rho(\mathbf{r})]$ is a unique and universal functional of the electron density. As already mentioned, the problem is that we do not have an exact formula for it. Local Density Approximation (LDA) and Generalised Gradient Approximation (GGA) are early and simple approximations for $E_{xc}[\rho(\mathbf{r})]$.

3.3.4.1 The Local Density Approximation

One very simple approximation for $E_{xc}[\rho(\mathbf{r})]$ is the LDA which makes use of the fact that we know E_{xc} almost exactly for the uniform electron gas [98, 99]. LDA assumes that the general inhomogenenous electronic system is locally homogenous and thus, the exchange correlation energy at every point in the system can be considered the same as that for a locally uniform electron gas of the same charge density [17, 92]. The total exchange-correlation energy in the whole system is:

$$E_{xc}^{LDA}[\rho(\mathbf{r})] = \int d^3\mathbf{r}\rho(\mathbf{r})\epsilon_{xc}^0(\rho(\mathbf{r})) \tag{3.23}$$

where ϵ_{xc}^0 is the exchange-correlation energy per electron in a homogeneous electron gas of density $\rho(\mathbf{r})$.

The quality of $\epsilon_{xc}^0(\rho(\mathbf{r}))$ can be further split into exchange and correlation contributions [97]:

$$\epsilon_{xc}^0(\rho(\mathbf{r})) = \epsilon_x^0(\rho(\mathbf{r})) + \epsilon_c^0(\rho(\mathbf{r})) \tag{3.24}$$

The exchange part ϵ_x^0 is the exchange energy of the uniform electron gas of a particular density and was originally derived by Bloch and Dirac in the late 1920's [100]:

$$\epsilon_x^0 = -\frac{3}{4}\sqrt[3]{\frac{3\rho(\mathbf{r})}{\pi}} \tag{3.25}$$

LDA provides surprisingly good results for metallic solids with delocalised electrons. However, it tends to overestimate the binding energies and underestimates the bond distances when describing materials with localised electrons. In addition, LDA underestimates the band gaps of semiconductors and insulators [101].

3.3.4.2 The Generalised Gradient Approximation

GGA is a semi-local approximation of the exchange-correlation energy and accounts for the non-uniformity of the electron density by considering the gradients of the spin-

polarized charge densities in each point. GGA incorporate the gradient corrections to $\epsilon^0_{xc}(\rho(\mathbf{r})$:

$$E^{GGA}_{xc}[\rho(\mathbf{r})] = \int d^3\mathbf{r}\rho(\mathbf{r})\epsilon^0_{xc}(\rho(\mathbf{r}))F(\rho(\mathbf{r}), \nabla\rho(\mathbf{r})) \tag{3.26}$$

with $F(\rho(\mathbf{r}), \nabla\rho(\mathbf{r}))$ to be defined suitably.

The first widely popular GGA exchange functional was developed by Becke [20] and its mathematical form has correct asymptotic behaviour at long range for the energy density. Other GGA exchange functionals have appeared, including the PBE, which were based on rational function expansions of reduced gradient [19]. Popular correlation functionals such as LYP, were developed in order to correct the correlation energy density. In particular, LYP is the only correlation functional able to correct the SIE in one-electron systems [21]. A complete specification of the exchange and correlation functionals is achieved by combining two acronyms and thus, BLYP includes Becke's GGA exchange with GGA correlation functional of Lee, Yang and Parr. In this work, both PBE and BLYP were used.

3.3.5 The problem of self-interaction

A large number of problems in simple DFT approximations come from the SIE the spurious interaction of an electron with itself. In classic Quantum Mechanics (QM), the electrostatic interaction between electrically charged particles is described by Coulomb's law:

$$U_{ee} = \frac{Q_1 Q_2}{\mathbf{r}_{12}} \tag{3.27}$$

while in DFT, as already mentioned, the electron-electron interaction energy is expressed as a functional of electron density. The Coulomb electron-electron interaction between two charge distributions ρ_1 and ρ_2 is given by:

$$V_{ee}[\rho(\mathbf{r})] = \frac{1}{2}\int\int \frac{\rho_1(\mathbf{r}_1)\rho_2(\mathbf{r}_2)}{\mathbf{r}_{12}} d(\mathbf{r}_1)d(\mathbf{r}_2) \tag{3.28}$$

DFT calculations employ the total electron density of the system for both ρ_1 and ρ_2 terms; each electron is therefore represented in both ρ_1 and ρ_2 and it does spuriously interact with its own charge distribution, hence the term self-interaction.

In one-electron systems, the condition for a functional to be self-interaction-free is sum of exchange-correlation and Hartree energies should be exactly zero [102].

$$V_{ee}[\rho(\mathbf{r})] + E_{xc}[\rho(\mathbf{r}) = 0 \tag{3.29}$$

In approximate exchange functionals the cancellation is incomplete and the remainder is known as the SIE. However, in one-electron systems the cancellation of self-interaction is quite good but this is not the case for finite systems [103]. Unfortunately, the SIE of a particular exchange approximation is much more difficult to quantify in a many-electron system and there is no unique way to correct it. The more the electrons are localised the bigger the error and thus, because of the SIE, DFT tends to favour delocalised solutions where electrons do not interact strongly with themselves, which could be a problem in the description of strongly localised d or f states in transition metal or rare earth compounds. The presence of self-interaction is reflected in an incorrect long-range behaviour of the potential acting on an electron. For an atom, we should have $V_{xc}(\mathbf{r}) \rightarrow$ -1/$\mathbf{r}$ for $\mathbf{r}\rightarrow \infty$, but simple functionals yield instead a potential that decays exponentially.

Although GGA improves on the performance of LDA, both LDA and GGA choices are affected by the SIE [104]. There are several approaches for Self-Interaction Correction (SIC), but their theoretical foundation is not completely convincing and,

thus, their efficacy is still a matter of debate. More advanced functionals (e.g orbital dependent functionals) seem to perform better in this respect.

Systematic improvements are known such as DFT+U , SIC-DFT and hybrid exchange functionals that introduce orbital-dependent terms in the Hamiltonian, thus restoring the individual contribution of each electron to Coulomb and exchange terms [102, 104, 105].

3.3.6 Orbital-Dependent and Hybrid functionals

To begin with, the use of KS orbitals is precisely what made DFT so successful allowing for much more flexibility in the construction of functionals and thus for more accurate functionals. Most importantly, the orbital dependent functionals can be used to compensate for self-interaction on a per orbital basis [102] and can give meaningful, well-defined, localised orbitals. In the following, we discuss specific examples of orbital-dependent functionals that have been proven to be of general practical usefulness.

The meta-generalised-gradient-approximation (meta-GGA) functionals represent a well-known class of orbital dependent functionals as they go beyond simply the gradient correction and they include the second derivative of the electron density whereas GGA include only the density and its first derivative in the exchange-correlation potential [106] . A functional is called a meta-GGA if it uses the kinetic energy densities:

$$t(\mathbf{r}) = \sum_{i}^{occupied} \frac{1}{2}|\nabla\psi_i(\mathbf{r})|^2 \tag{3.30}$$

where the ψ are the self-consistently determined Kohn-Sham orbitals. However, the crucial problem of self-interaction is only slightly reduced, because a major contribution to the self-interaction energy comes from the Hartree energy.

A widely used approach to correct for the SIE is the construction of hybrid exchange functionals. These are a class of functionals which attempt to combine some of the most useful features of the Hartree-Fock Hamiltonian within DFT. As already men-

tioned, in HF theory the self-interaction cancellation between Coulomb and exchange contributions is exact, or in other words the HF solution is self-interaction free. To the extent that errors in total HF energies track with the errors in HF exchange, the mixture of HF and DFT formulations can provide a convenient method to correct for the electronic SIE.

In 1993, Becke was the first who devised the hybrid approach [107]. Later in 1996, Ernzerhof and co-workers attempted to rationalise the idea of mixing the Fock exchange to the standard DFT [108, 109]. However, the evaluation of the Fock exchange under periodic boundary conditions required a lot of computational effort and as a result the application of HF/DFT combinations to periodic systems was rare and the routine hybrid functional calculations of molecular systems were not possible. The CRYSTAL98 code was the first periodic code which supported hybrid functionals using local basis sets. Since then, many solid-state studies have been carried out with hybrid functionals, providing valuable insight on how accurate and applicable they can be.

The performance of hybrid exchange functionals in solid state chemistry has been thoroughly analysed by Corà *et al.* [104]. In particular they focused on transition metal compounds and they showed how hybrid functionals describe crystalline solids. The structural and electronic properties were investigated as the amount of HF (exact) exchange in the hybrid functional was getting larger. The most important output was that the electronic localisation in the solution was increased when the HF exchange was added. This caused the lattice parameter to decrease and the ionicity of the materials, the elastic constants and bulk moduli to increase. For other properties such as band gaps, phonon spectra, magnetic coupling constants and those depending on the extent of electronic localisation for both cases of perfect and defective lattices, it was found that HF and standard DFT functionals (LDA and GGA) generated systematic errors with opposite sign comparing to experimental results, while the hybrid functionals could yield more accurate results. In general, they concluded that although the optimum amount of HF exchange used in the functional differs according to the examined sys-

tem, the best percentage for a solid state specific hybrid functional is generally higher than in molecules, where standard choices are B3LYP (20% HF) and PBE0 (25% HF) [110].

Another hybrid functional, the Heyd-Scuseria-Ernzerhof (HSE06) performs very well, due to the SIE correction from the partial inclusion of Hartree-Fock exchange [111]. The HSE06 functional derives from PBE0 functional, which is an implementation of the Becke three-parameter hybrid formula:

$$E_{\mathrm{xc}}^{\mathrm{PBE0}} = \frac{1}{4}E_{\mathrm{x}}^{\mathrm{HF}} + \frac{3}{4}E_{\mathrm{x}}^{\mathrm{PBE}} + E_{\mathrm{c}}^{\mathrm{PBE}}, \tag{3.31}$$

where $E_{\mathrm{x}}^{\mathrm{HF}}$ is the HartreeFock exact exchange functional, $E_{\mathrm{x}}^{\mathrm{PBE}}$ is the PBE exchange functional, and $E_{\mathrm{c}}^{\mathrm{PBE}}$ is the PBE correlation functional [19, 107]. In HSE06, the exchange terms are divided into short-range and long-range parts, and to avoid the expensive calculation of long-range HF exchange, this term is replaced by long-range PBE exchange:

$$E_{\mathrm{xc}}^{\omega\mathrm{PBEh}} = \frac{1}{4}E_{\mathrm{x}}^{\mathrm{HF,SR}}(\omega) + \frac{3}{4}E_{\mathrm{x}}^{\mathrm{PBE,SR}}(\omega) + E_{\mathrm{x}}^{\mathrm{PBE,LR}}(\omega) + E_{\mathrm{c}}^{\mathrm{PBE}} \tag{3.32}$$

where ω is a screening parameter controlling the range of the interaction. Standard values of $\omega = 0.2$ determined as a compromise between speed and accuracy from a test set of molecules and solids [112] .

There is some evidence of cancellation of the self-interaction in DFT+U methods which lead to much better results [7, 8, 113]. DFT+U method was developed by Anisimov *et al.* [105, 114] to deal with electron correlations in transition metal and rare earth compounds. With the use of DFT + U functionals, only a single effective interaction parameter, U, is required to characterize the localization of the 3*d* electrons. The performance of LDA+U and GGA+U is presented thoroughly from Rohrbach *et al.* [115]. The key concept of DFT+U is to address the on-site Coulomb and exchange interactions in the localized *d* or *f* orbitals with an additional Hubbard-type [116] term. By treating the regular DFT Hamiltonian (LDA or GGA) with standard Hubbard mod-

els, a hybrid Hamiltonian is formed which modifies the electron potential within the transition metal or rare earth atom radii from the LDA/GGA by an amount proportional to the U parameter in this model. The spin-polarized DFT+U total energy is obtained by the following expression:

$$E^{DFT+U} = E^{DFT} + \frac{U-J}{2}\sum_{m\sigma}(n_{m\sigma} - n_{m\sigma}^2) \tag{3.33}$$

where $n_{m\sigma}$ is the operator yielding the number of electrons occupying an orbital with magnetic quantum number m and spin σ at a particular site and U and J are the spherically averaged matrix elements of the screened Coulomb electron-electron interaction [117]. U values have been calibrated for many transition metals of interest using the approach outlined in Wang *et al.*'s work [8]. For the GGA+U method, there is little additional computational cost compared to GGA, making it an efficient way to study transition metal compounds.

Although orbital dependent functionals seem to perform better, they still suffer from limitations, in particular DFT+U and hybrid exchange functionals, while introducing terms explicitly aimed at correcting the SIE do not derive from first principles. Hence their results should be treated in parametric way, and the best correction determined by comparison with experiment. The main parameter of hybrid exchange functionals is the variable amount of HF exchange employed in the description of exchanges forces.

The hybrid functionals we used in Chapters 4 and 5 are PBE and BLYP with different amount of HF exchange from 5 to 50% , while in Chapter 6 we limited our work to B3LYP (20% HF) and PBE with 50% of HF exchange.

3.4 Other electronic structure approaches

After years of continuous theoretical developments and improvements, working formulations of the exchange and correlation functionals at the basis of DFT retain a low computational cost, while in the same time they are accurate for most needs in both molecular and solid-state sciences. The formulation of hybrid HF/DFT functionals has been crucial in achieving this goal [104]. However, there is a large number of electronic structure methods from post-HF which are based on wavefunction techniques, to Quantum Monte Carlo (QMC) .

Post-HF techniques [87, 91], such as configuration interaction (CI) [118] and Møller-Plesset perturbation (MP2 [119], MP3, MP4) are *ab inito* quantum chemistry methods that have recently become available. They are a set of methods developed to improve HF or SCF by accounting for electron correlation. However, MP2, for example, overestimates pure van der waals interactions and relies on error compensations. MPn theory usually suffers from severe spin contamination, especially when open-shell molecules are involved. Coupled cluster is another technique used for describing many-body systems. CCSD(T) is the coupled cluster theory with single and double excitations and perturbative corrections for connected triples excitations. Connected triples are found to be extremely crucial for dispersion bonded systems. CCSD(T) describes very well the van der waals interactions but the computational cost becomes very high and thus, it is applied only to systems with few tens of electrons. In general, although post-HF methods in solid-state systems yield more accurate results than HF calculations, their extension is difficult and with high computational cost.

QMC method aims to study complex quantum systems and facilitate the calculation of various properties of correlated quantum systems [120]. It is a broadly applicable computational tool for providing a reliable solution of the many-body Schrödinger equation for molecules, solids and other systems. QMC is able to give accurate treatment of van der waals forces in solid materials. However, as we describe in our method-

ology section, for our studies the omission of van der waals dispersion is not likely to affect our results.

3.5 Basis Sets

The basis set is the set of mathematical equations from which the wave function is constructed and they are almost always needed to practically solve the Schrödinger equation. Basis sets describe the molecular orbitals in QM as atomic functions and for a basis set to be good, these functions should allow for the wave function to be precisely described with the lowest possible computational cost. Slater type orbitals (STO) originally described these functions:

$$R(r) = Nr^{n-1}e^{-\zeta r} \tag{3.34}$$

where the radial part is described by a normalising constant N, the principal quantum number n, the distance of the electron r and a constant describing the effective charge of the nucleus ζ. However, integrating the $e^{-\zeta r}$ is not always straightforward and thus, in conventional wave functions based approaches, such as HF, the Gaussian type orbitals (GTO) are preferred. GTOs have the same angular dependence as STO, but they have a radical part in $e^{-\zeta r^2}$. Unlike the STO functions, GTO do not exhibit the correct cusp at nucleus and the desired exponential decay in the tail regions since r$\rightarrow \infty$. Thus, accuracy must be improved since GTOs have computational advantages (easier to evaluate).

The main way is to choose several values of ζ in the $e^{-\zeta r^2}$ term and take a linear combination of these. Each individual GTO (each separate value of ζ) is called a primitive Gaussian. Once the best linear combination of primitives is obtained, the weightings are frozen and the resulting combination is called contracted Gaussian and can better approximate the exponential function of real electron density. A common notation for Gaussian basis sets is X-YZG, where X is the amount of functions used

to describe the core electrons, and Y and Z are the amount of contracted and diffuse functions used to describe the valence electrons respectively.

GTOs can be improved by making them "double-zeta" and for e.g. in an STO-6-31G basis set, each core orbital is considered to be a STO represented by a fixed linear combination of 6 Gaussian primitives and each valence orbital is treated as two STOs ("double-zeta") described by three Gaussian primitives respectively.

Basis sets are often enhanced by the addition of polarization functions. This method works by adding an element of higher angular momentum number to the basis set, representing the perturbation of an electron cloud by an atom's environment. For e.g. in an STO-6-31G* basis set, the asterisk * indicates the polarization for heavy atoms while two asterisks indicate polarization on light atoms. Further improvement of these basis sets is accomplished by adding diffuse functions.

In addition, there are basis sets for solids which do not actually comply with the linear combination of atomic orbitals (LCAO) scheme i.e., plane waves, which are employed in complex periodic systems in DFT. The orbital wavefunction is described by a finite number of plane waves. Since the deeply bound core electrons within plane wave basis sets require a huge amount of basis functions for their description, the computational cost is high. To solve this problem, plane wave basis sets are often used in combination with an "effective core potential" or pseudo-potential (nonlocal operators, i.e. they are not simple functions) and the plane waves are only used to describe the valence charge density. This is because core electrons tend to be concentrated very close to the atomic nuclei. Gaussian plane waves (GPWs) require pseudo-potentials to describe the high variance of wavefunctions close to the nucleus.

3.6 Periodic Boundary Conditions

The electron correlation within a solid is not the only obstacle to solving the Schrödinger equation for a condensed matter system: for solids, we should take into account the effectively infinite number of electrons within the solid. Together with periodic boundary conditions (PBC), Bloch's theorem has enabled simulating the infinite bulk using a single unit cell, and it based on the translational invariance of the system in three dimensions [100]. According to the Bloch's theorem, the wavefunction of an electron within a perfectly periodic potential may be written as:

$$\psi_{nk}(\mathbf{r}) = e^{ik\cdot r} u_{nk}(\mathbf{r}) \tag{3.35}$$

where $u_{nk}(\mathbf{r})$ is a function that possesses a periodic potential because the ions are arranged with periodicity of the Bravais lattice

$$u_{nk}(\mathbf{r} + \mathbf{R}) = u_{nk}(\mathbf{r}) \tag{3.36}$$

where R is the length of the unit cell, n is the band index and takes numbers n=1, 2, 3,..., and k is a wavevector confined to the first Brillouin Zone.

In PBC, the system modelled is assumed to be a unit cell which is surrounded by an infinite array in three dimensions of identical replicas where all boundaries (surfaces) are so far away that they can be omitted, and only the lattice (which is periodic) affects the properties of the material. As shown (for a 2D system) in figure 3.1 [121], the blue box represents the unit cell while the surrounded boxes are exact copies in every aspect. Thus, PBCs preserve mass and the number of atoms in the cell and also no atom is acted on by any surface forces, as these are completely removed [87]. The r_{cut} is the cut-off distance which is normally applied in evaluating non-bonded interactions.

As we can see, an atom could possibly interact with one in the neighbouring cell (which is an image of one of the atoms in the simulation cell) because it is within the cut-off distance.

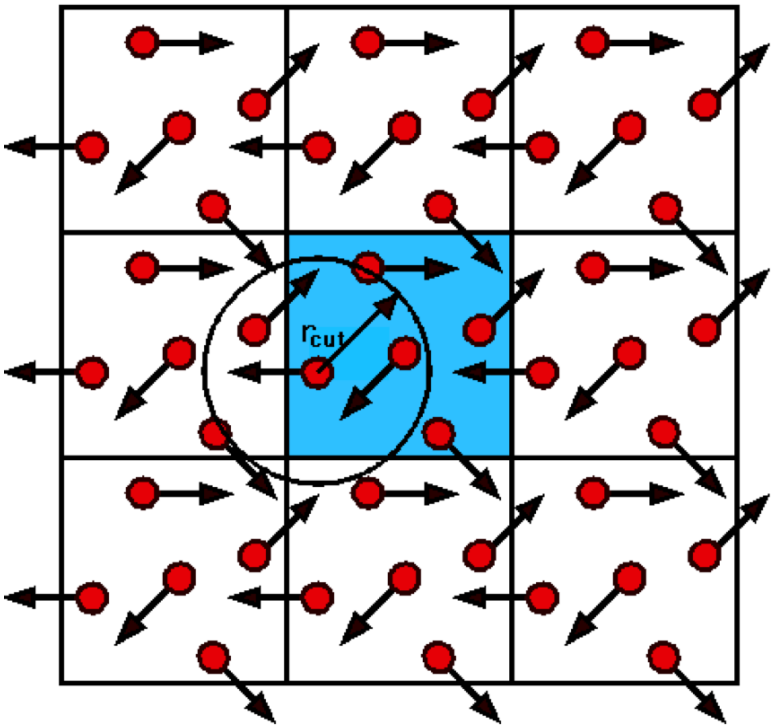

Figure 3.1: A simulation cell surrounded by periodic images generated by PBC. The arrows indicate the movement of the molecules [121].

3.7 Methodology

In this thesis we examine the performance of GGA and hybrid exchange functionals within density functional theory in representing the energetics of redox reactions. Thus, having addressed the general aspects of DFT we focus on its implementation for the systems discussed in this thesis.

3.7.1 Prior computational methods for transition metal-doped AlPO's

A wide range of computational techniques for solid-state research allow the understanding of different aspects of the chemistry of pure and doped zeotypes. IP techniques discussed earlier, can describe the structural stability of different undoped frameworks of AlPOs and give valuable insight on the structural strain caused when a dopant ion with different size or charge is added (see reference [64]).

QM methods provide information on the electronic properties, such as the relative stability of different electronic and spin states of TM dopants, focusing explicitly on the treatment of electronic degrees of freedom. The model of the solid as well as the Hamiltonian provide several alternatives when applied to the study of zeotypes. Techniques that employ periodic boundary conditions (PBC) are appropriate for the extended nature of crystalline materials.

Periodic QM calculations were performed by Corà et al. [64] in order to describe the equilibrium structure of nanoporous AlPO polymorhps using a range of different Hamiltonians from the HF to LDA, GGA and HF-DF hybrid scheme (B3LYP functional). Since all Hamiltonians provided results in good overall agreement, subsequent studies on doped AlPOs were performed at the (unrestricted) Hartree- Fock (HF) level of theory. By using QM, they investigated possible correlations between the acidity of the doped framework and the atomic properties of the dopant, such as ionic radius and electronegativity, and its crystalline environment (bond distances and angles) in the AlPO framework [13, 122].

3.7.2 Transition state searching

During a study of reactivity, a parallel process to energy minimisation techniques is the transition state searching. For a given reaction as shown in figure 3.2, a transition state (TS) corresponds to a maximum energy structure lying between connecting reactants and products. A TS is defined as a saddle point, which is a stationary point with one negative frequency along the vector that connects minima. Finding a TS on a potential energy surface (PES) is a delicate process because roughly guessed attempts to locate a TS may lead to unsuccessful results. Several standard molecular quantum mechanical codes have managed to code algorithms that could efficiently locate saddle points on the PES [123].

Usually periodic codes based on plane waves pseudo-potential approach adopt the nudged elastic band (NEB) approach [125]. The NEB has the advantage of requiring

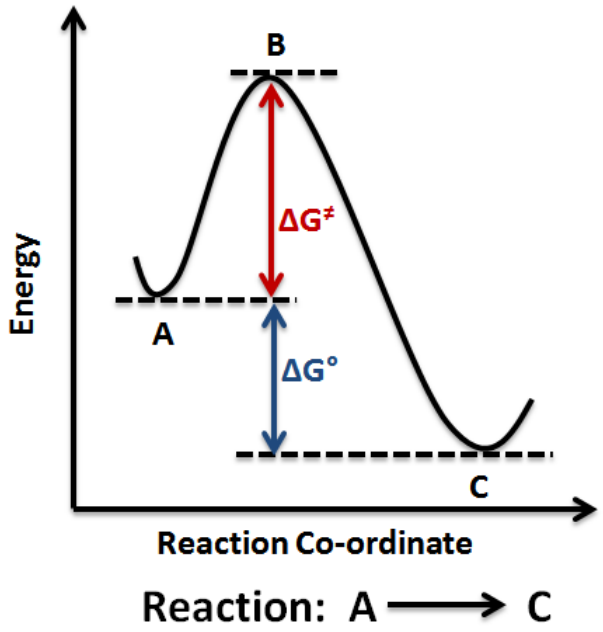

Figure 3.2: Reaction profile where the reactant A converts to product C via the transition state B [124].

energy and gradient only to discover the minimum energy path, at the expense of a relatively high number of images needed to improve the accuracy of the search. The initial and final steps of the examined reaction are known and the code works by linearly interpolating a set of images between those steps, and then minimizes the energy of this string of images. Each image corresponds to a specific geometry of the structure from the initial to the final state, creating a snapshot along the reaction path. Thus, once the energy of this string of images has been minimized, the true Minimum Energy Path (MEP) can be found.

Another method which is used to identify saddle points on a PES is the dimer method [126]. In this method, the user can start from an initial guess and search for a nearby saddle point. Another application of dimer method is to start from a minimum basin and search in random directions for saddle points. If the transitions out of a basin

are found, their individual rates can be evaluated, and the system can be evolved over long time scales using kinetic Monte Carlo.

Metadynamics is another method usually applied within molecular dynamics simulations, which was first suggested by Laio and Parrinello [127]. Metadynamics and NEB rely on the knowledge *a priori* of the reaction coordinate.

3.7.3 Proposed methodology

Since there is a wide range of problems associated with the presence of TMs in AlPOs, the calculations described in the following chapters have been performed with a particular methodology and code which have been carefully validated in previous studies [39, 40, 64].

DFT calculations were performed, as implemented in the program CRYSTAL [128]. The CRYSTAL code is a very useful tool in order to perform consistent studies of the physical and chemical properties of molecules, polymers, nanotubes, surfaces and crystalline solids. The CRYSTAL package performs *ab initio* calculations of the ground state energy, energy gradient, electronic wave function and properties of periodic systems within Hartree Fock, density functional or various hybrid approximations [129] .

3.7.3.1 Aerobic oxidation of linear alkanes catalysed by Mn-doped AlPOs

As already described in detail in Chapter 2, we focused on two elementary reaction steps of the catalytic mechanism in reference [40]; one from the preactivation cycle

$$RH + Mn^{III} \rightarrow R\cdot + Mn^{II}(H) \tag{3.37}$$

and one from the propagation cycle

$$ROO\cdot(M^{III}) + RH \rightarrow ROOH(M^{III}) + R\cdot \tag{3.38}$$

Mn-doped AlPO-5 and AlPO-34 are the systems we focused on Chapters 4 and 6. Mn dopants are open-shell ions with unpaired electrons and the spin-polarized solution was computed after definition of the electron ($\alpha - \beta$) occupancy. Spin polarization occurs due to exchange-correlation effects via the interactions of the electrons of the same spin as an unpaired electron in the open-shell system. Unrestricted wavefunctions allow different spatial distribution for electrons with α spins and β spins and therefore can describe spin polarization.

The basis set employed to describe the host AlPO framework has been optimised by Corà *et al.* [130] and describes very well the electronic distribution on the metal sites. The electronic distribution of the systems is described as a linear combination of atomic orbitals (Bloch functions (BF) defined in terms of local functions), and the basis functions are expressed analytically as a contraction of Gaussian-type orbitals [26]. Gaussian type functions (GTF) of *s*, *p* and *d* symmetry are used. A triple-valence plus polarization basis set was used for Mn and a double-valence plus polarization for the rest of the atoms for all calculations, and are provided from the online library of the CRYSTAL code [131]. The use of GTOs can describe much better Jahn-Teller type distortions for open-shell d^4 transition metals like Mn^{3+}, like in our system, compared to the use of pseudo-potentials. In addition, Gómez Hortigüela *et al.* [14] have compared rigorously the predicted structure of the active sites in MnAlPOs using this computational methodology, with that obtained by X-ray absorption spectroscopy showing that the performance of the computational settings chosen is reliable.

Both AlPO-5 and AlPO-34 frameworks are periodic in 3 dimensions (crystals, 3D) and they are described with PBC.

In Chapter 4, ethane (CH_3CH_3) is used as the hydrocarbon and Mn-doped AFI structure as the catalyst. The AFI framework comprise one-dimensional, non-interconnected, 12-membered ring (MR) channels whose walls are formed by 6-MR windows (figure 3.3). These large channels are surrounded by smaller 6- and 4-MR voids, which are too small to permit the diffusion of the hydrocarbon reactants; inside

the aluminophosphate frameworks, divalent cations such as Mn^{2+} are inserted in tetrahedral position and replace Al^{3+} (but not P^{5+}) and as a result, Mn can take only one type of position in the MnAlPO-5. Thus, 1 Mn ion is inserted in a tetrahedral position by replacing one Al ion in the unit cell. One crystallographic cell of 72 atoms is used with P1 symmetry. Mn image sites do not interact with each other significantly as the distance between them is over 8 Å. No significant interaction appears between the reactants in contiguous image cells because the AFI unit cell dimensions are sufficiently large.

Van der Waals dispersion occurs between the different parts of our system, which are the hydrocarbon and the AFI framework. Because we are looking at the reactivity and we are calculating activation energies, changing configuration between reagents and TS would not lead to significant changes to dispersion energies. Both reagent and product molecules are contained in the AlPO pores and thus, the dispersion is transferable throughout the reaction. As a result the contribution of dispersion correction is expected to be negligible [132].

In order to obtain the initial unit cell parameters, full geometry optimizations of the MnAlPO-5 are performed with Mn in the oxidized state, since this corresponds to the initial state of the catalyst in the absence of reactants; for the rest of the calculations the unit cell dimensions are kept fixed.

Full geometry optimizations of the reactants and products were performed in order to find the reaction enthalpies. In addition, by finding the whole reaction profile we could identify reliably the activation energies. To locate the TS we performed a scan calculation along the reaction coordinate by moving the reactant species in discrete steps of 0.1 Å in order to find the reaction pathway. For the first step of the preactivation cycle, the reaction coordinate is the distance between the dissociating H and the framework O atom forming the new O-H bond. Similarly, for the first step of the propagation cycle, the reaction coordinate is the distance between the H atom in the hydrocarbon that is going to be transferred and the radical O atom in RO·.

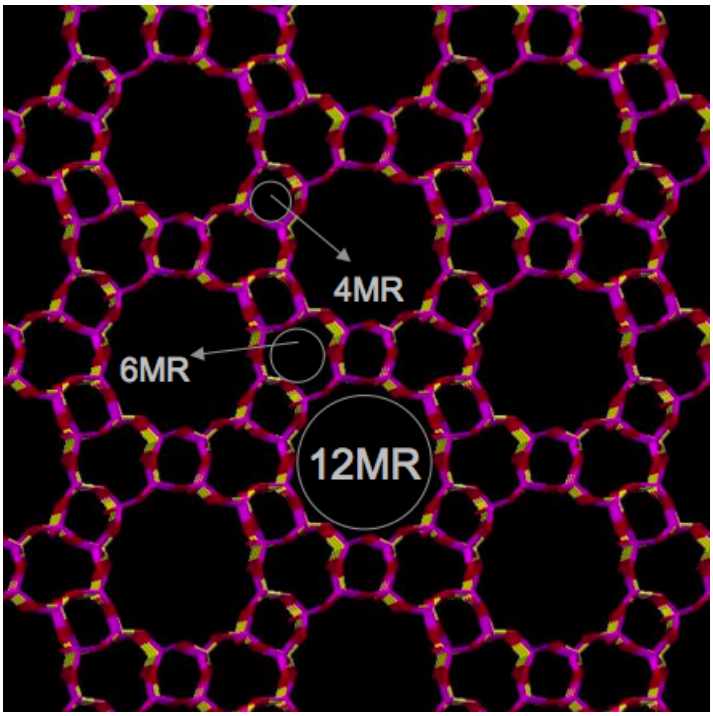

Figure 3.3: Representation of AlPO-5 framework and indication of the distances of MR.

A series of constrained geometry optimizations is then performed by keeping the reaction coordinate fixed and allowing the rest of the internal coordinates to relax. At the end of the scan, a set of intermediate energy points connecting reactants and products is obtained. The corresponding activation energies and the transition states (TS) are identified as the point where the energy along the reaction profile is a local maximum. Gómez Hortigüela *et al.* have shown in the previous studies [40] that this procedure of TS search is reliable and gives results that are close to those obtained using second derivative-based methods, both in geometry and energy. In addition, the examined reaction steps are understood very well and it was not necessary to use other TS search methods, such as the NEB and metadynamics.

In order to focus on the full reaction mechanism, previous studies [39–43] have been limited to the B3LYP functional. However, reaction enthalpies and activation barriers, especially when involving open-shell TM ions with *d* electrons are sensitive

to the details of the Hamiltonian as these are the systems where the SIE of DFT is most pronounced. As already discussed, GGA functionals [133] are known to fail in the description of the electronic properties of early TM compounds because of the SIE which is considerable for strongly localized *d* or *f* states. However, the development of B3LYP [20, 21] and other hybrid functionals, which combine the GGA and exact exchange, allow accuracy to be imposed whenever HF and standard DFT results deviate in opposite directions from experiment[104]. The self-interaction correction is accomplished via the inclusion of HF exchange, that localizes electrons on the *d* orbitals and is larger the greater the localization of the states [96].

One of the aims of this thesis is to benchmark different functionals by examining how they influence the calculated reaction enthalpies and activation barriers of redox reactions. We complement the B3LYP results with a selection of GGA and hybrid functionals, using a varying amount of HF exchange. In particular, the standard DFT functionals we used are BLYP and PBE with 0% of HF, while the hybrid exchange functionals are BLYP with 20 and 25% of HF exchange and PBE with 5, 10, 20, 25 and 50 % of HF exchange. Hereinafter, we indicate as F_z-xc (xc=BLYP or PBE) the hybrid exchange functionals where a fraction z of HF exchange has been employed in conjunction of the BLYP or PBE exchange functional.

In Chapter 6, we followed the same methodology as in Chapter 4. However, ethane (C_2H_6), propane (C_3H_8) and hexane (C_6H_{14}) were used as hydrocarbons in order to examine any selectivity issues and then we changed our catalyst from MnAlPO-5 to MnAlPO-34 to observe if a smaller framework imposes any steric constraints to the reaction. For CHA (AlPO-34) structure we used one crystallographic cell of 36 atoms with P1 symmetry. Mn image sites do not interact with each other significantly as the distance between them is over 8 Å. No significant interaction appears between the reactants in contiguous image cells because the unit cell dimensions are sufficiently large. In this Chapter, we limited our work to B3LYP hybrid exchange functional, although some calculations were also performed with $F_{0.50}$-PBE.

3.7.3.2 The Li intercalation in $LiMnPO_4$ and $LiFePO_4$ olivine structures

The Mn^{3+}/Mn^{2+} redox chemistry and local environment of Mn observed in MnAlPO system is the same exploited in the intercalation chemistry of $LiMnPO_4$ in Li-battery cathodes. Figure 3.4 shows the olivine structure adopted by $LiMPO_4$ (M=Mn or Fe). Both lithiated and de-lithiated MPO_4 adopt an orthorhombic unit cell with four formula units (FU) and space group *Pnma*. The olivine structure consists of MO_6 octahedra and PO_4 tetrahedra; the M^{2+} ions with their surrounding 6 oxygen atoms form a network of corner-shared octahedra interlinked by PO_4 tetrahedra together with the 4 oxygen atoms form an isolated tetrahedron with P in the centre. The presence of large tetrahedral polyanions $(PO_4)^{3-}$, corner-shared MO_6 octahedra, and the use of the M^{3+}/M^{2+} redox couple are distinctive features of olivine class cathodes.

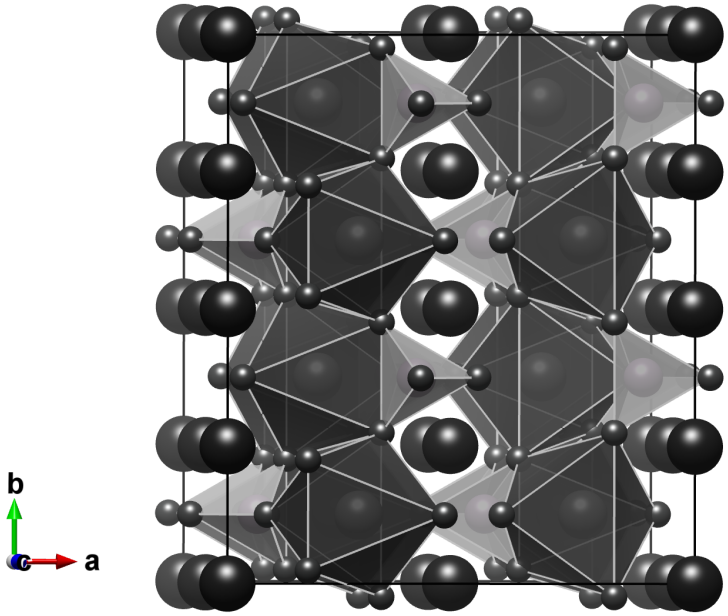

Figure 3.4: Schematic representation of $LiMPO_4$ olivine structure with PO_4 tetrahedra in light grey and MO_6 octahedra in dark grey. Li is represented by the black spheres in the interstitial channels.

The open-circuit voltage (OCV) between two electrodes depends on the difference between the chemical potential of Li at the anode and the cathode. As Li ions are inserted into the cathode, the chemical potential increases, leading to a decrease in the OCV. The insertion reaction is represented by the following equation:

$$\delta x Li + Li_x MPO_4 \rightarrow Li_{x+\delta x} MPO_4 \tag{3.39}$$

the difference of the Li chemical potential (μ_{Li}) between the anode and cathode and the OCV can then be related [134]:

$$V(x) = \frac{\mu_{Li(x)}^{cathode} - \mu_{Li}^{anode}}{F} \tag{3.40}$$

where F is the Faraday constant.

The average intercalation potential $\langle V \rangle$ for Li insertion between $Li_{x_1} MPO_4$ and $Li_{x_2} MPO_4$ can be found by integrating the latter equation between x_1 and x_2. Neglecting the entropic and $P\Delta V$ contributions [9], $\langle V \rangle$ can be calculated as follows:

$$\langle V \rangle = \frac{-[E(Li_{x_2} MPO_4) - E(Li_{x_1} MPO_4) - (x_2 - x_1)E(Li)]}{(x_2 - x_1)F}, \tag{3.41}$$

where E is the total calculated energy (in eV). Typically x_1=0 and x_2=1 are taken as composition limits as in these cases there is no Li-vacancy disorder. $\langle V \rangle$ is thus determined by computing the total energy of three compounds: $LiMPO_4$, MPO_4 and metallic Li.

In Chapter 5, we perform DFT calculations in $LiMPO_4$(M=Mn or Fe) which has a similar behaviour with the MnAlPO-5 system. In a similar fashion to Chapter 4, DFT calculations were performed, using the program CRYSTAL09 [128]. The wavefunction of the system is described as a linear combination of atomic orbitals, and the basis functions are expressed analytically as a contraction of Gaussian-type orbitals. A triple-valence plus polarization basis set was used for Mn and Fe and a double-valence plus polarization for the rest of the atoms for all calculations, as provided from the online library of the CRYSTAL code [131]. Full geometry optimizations of all phases

were performed using different GGA and hybrid exchange functionals. In particular, two of the them are standard DFT functionals (BLYP and F_0-PBE) and the rest are hybrid exchange functionals; B3LYP, $F_{0.25}$-BLYP and $F_{0.35}$-BLYP with 20, 25 and 35% of HF exchange and $F_{0.05}$-PBE, $F_{0.10}$-PBE, $F_{0.20}$-PBE, $F_{0.25}$-PBE, $F_{0.35}$-PBE and $F_{0.40}$-PBE.

3.8 High Performance Computing (HPC)

This work made use of the facilities of high-performance computing services in order to run calculations that require large numbers of processing cores in parallel fashion. Thus, HECToR and ARCHER, the UK's national high-performance computing service, was used throughout the research. ARCHER is a Cray XC30, funded by EPSRC, NERC, EPCC and Cray Inc. It is more than three times more powerful than its predecessor, HECToR, and is hosted by the University of Edinburgh [135]. A series of calculation were also performed with Legion, which is a centrally funded computing facility aimed at supporting all types of research at University College London (UCL) [136]. The larger computing power available is enabling researchers who study problems with a global impact in the area of chemistry and materials science to explore the chemical properties of materials in physically realistic environments rather than making approximations and using idealised systems.

Chapter 4

Effect of exchange functionals on the calculated activation energies - A DFT study of the catalytic aerobic oxidation of ethane in MnAlPO-5

4.1 Introduction

The study of redox reactions through electronic-structure techniques has stimulated interest because of their significance in heterogeneous catalysis [137–139]. The estimation of redox energies is important for the design of more efficient catalysts. In this chapter, we focus on the widely studied aerobic oxidation of ethane catalyzed by Mn-doped AlPO-5 and we examine the performance of GGA and hybrid exchange functionals.

Previous computational investigations [39–43], using hybrid exchange Density Functional Theory (DFT) techniques have considered the whole catalytic cycle of the aerobic oxidation of ethane catalyzed by Mn-doped AlPO-5, which comprises over 20 reaction intermediates. The elementary reaction steps have been divided in subsequent

stages of preactivation, propagation, hydroperoxide decomposition and regeneration (further oxidation):

Preactivation mechanism

$$CH_3CH_2H + Mn^{III} \rightarrow CH_3CH_2\cdot + Mn^{II}(H) \quad (4.1)$$

$$CH_3CH_2\cdot + O_2 \rightarrow CH_3CH_2OO\cdot \quad (4.2a)$$

$$CH_3CH_2OO\cdot + Mn^{III} \rightarrow CH_3CH_2OO\cdot(M^{III}) \quad (4.2b)$$

Hydroperoxide decomposition

$$CH_3CH_2OO\cdot(M^{III}) + CH_3CH_2H \rightarrow CH_3CH_2OOH(M^{III}) + CH_3CH_2\cdot \quad (4.3)$$

$$CH_3CH_2OOH + M^{II}(H) \rightarrow CH_3CH_2O\cdot(M^{III}) + H_2O \quad (4.4a)$$

$$CH_3CH_2OOH + M^{II}(H) \rightarrow HO\cdot(M^{III}) + CH_3CH_2OH \quad (4.4b)$$

Propagation mechanism

$$CH_3CH_2O\cdot(M^{III}) + CH_3CH_2H \rightarrow CH_3CH_2OH(M^{III}) + CH_3CH_2\cdot \quad (4.5a)$$

$$HO\cdot(M^{III}) + CH_3CH_2H \rightarrow H_2O(M^{III}) + CH_3CH_2\cdot \quad (4.5b)$$

Regeneration mechanism

$$CH_3CH_2OO\cdot(M^{III}) + CH_3CH_2OH \rightarrow CH_3CH_2OOH + Mn^{II}(H) + CH_3CH(=O) \quad (4.6)$$

The Mn redox activity, particularly its reversible interconversion between 2+ and 3+ oxidation states, and how the variable coordination number of Mn in the AlPO framework enables reversible complexation with substrate molecules, are both important factors in the catalytic efficiency of MnAlPOs. The role of both Mn^{III} and Mn^{II} in the reaction mechanism is significant: Mn^{III} sites produce the alkyl hydroperoxide which can only be transformed by Mn^{II} into alcohol, aldehyde and acid. The computational study demonstrated the requirement of an initial preactivation step to yield reduced Mn^{II} sites which are able to decompose the hydroperoxide intermediates. Here, starting from a calcined oxidised catalyst with Mn^{III}, Mn^{II} is produced via radical H· abstraction, from the hydrocarbon substrate itself (full description of mechanism in Chapter 2). In this chapter, we focus on two representative steps, as already discussed in previous chapters, of the catalytic cycle obtained from previous work; the first is the abstraction of H from ethane in the preactivation phase (reaction step 4.1), which involves a reduction of the Mn^{III} site to Mn^{II}. The second step comes from the propagation phase of the catalytic cycle where Mn does not change oxidation state (reaction step 4.5a). By examining these two key reaction steps in detail, we gain valuable additional understanding of the fundamental electronic processes and are able to gauge the performance of different functionals in DFT calculations.

In order to focus on the full reaction mechanism, earlier studies have been limited to the B3LYP functional. However, reaction enthalpies and activation barriers, especially when involving open-shell transition metal (TM) ions with *d* electrons are sensitive to the details of the Hamiltonian which are the systems where the SIE of DFT is most pronounced. Local and semi-local functionals such as LDA and GGAs [133] are known to fail in describing the properties of electrons in well localized electronic states, such as in the 3*d* atomic orbitals of first row TM ions. Quantitative study of these systems require orbital dependent functionals of which hybrid-exchange formulations represent one widely employed example [20, 21, 104]. In the hybrid exchange functionals, the self-interaction correction is accomplished via the inclusion of a fraction of

HF exchange, whose effect is to localize electrons on the *d* orbitals and is larger the greater the localization of the states [96].

With reference to the two steps that we examine in detail, while the effect of the SIE on the reduction energy of Mn^{III} to Mn^{II} is now well acknowledged, we would like to note that even step 4.5a, where Mn does not change oxidation state, will be affected by the SIE to some extent, because the localisation of the radical varies in the TS relative to reagents and products.

The aim is to benchmark different functionals by examining how they influence the calculated reaction profiles. We complement the B3LYP results with a selection of GGA and hybrid functionals, using a varying amount of HF exchange between 0 and 50%. Our results aim to provide a quantitative and qualitative benchmark for this important type of reaction and thus, guide future work on heterogeneous redox processes.

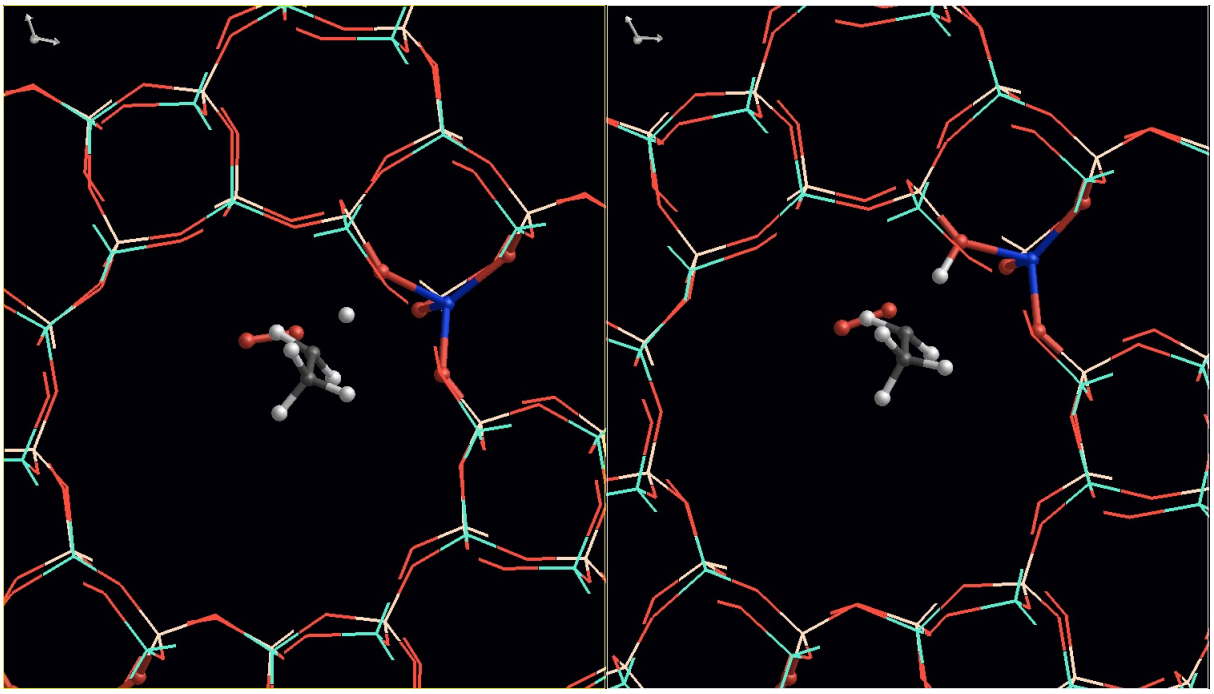

Figure 4.1: View of the TS (left) and product (right) structures for the preactivation step. A hydrogen transfer to the active site takes place, yielding a Mn^{II} site and an ethyl (R·) radical, which is then rapidly stabilized by the addition of O_2 to form ROO·. Mn active site is represented in blue, P in brown, Al in green and O in red.

4.2 *Preactivation step* - Formation of the ethyl radical and Mn reduction

The first part of this study considers the initial elementary step (reaction step 4.1) of the preactivation mechanism presented in reference [39]. Preactivation of the Mn^{III}-AFI catalyst in the presence of O_2 and ethane yields reduction of the Mn active site through homolytic transfer of a hydrogen atom from RH to the active site (figures 4.1 and 4.2).

$$Mn^{III}\,(O) + RH \rightarrow Mn^{II}\,(OH) + R\cdot$$

Our results suggest that O_2 does not intervene in this initial step and is always located far from the radical species upon geometry optimisation at each step. A bond is formed between the H of the ethane molecule and one O of the framework which is nearest neighbour to Mn, as shown in figure 4.2.

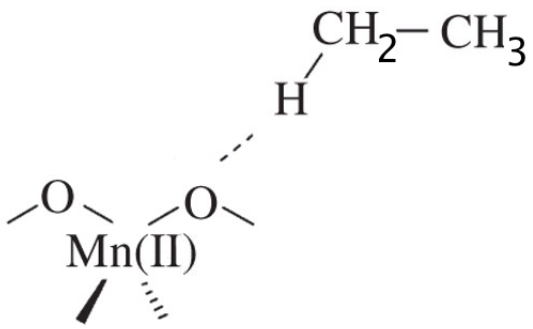

Figure 4.2: Reaction scheme showing the TS in preactivation step.

The reaction coordinate is scanned from the initial value of up to 3.2 Å corresponding to the O-H distance in the geometry optimized configuration for the reagents, to a final value of 1.00 Å, with steps of 0.1 Å or smaller in the vicinity of the TS. The energy evolution as a function of the reaction coordinate is shown in figure 4.3 for all functionals employed. Table 4.1 and figure 4.4 summarise the activation energies and reaction enthalpies. The zero of the energy is chosen to coincide with the reagents i.e. Mn^{III}-AlPO5 with one ethane molecule not interacting with the active site. From figure 4.4 we observe small differences between the two semi-local exchange functionals F_x-BLYP and F_x-PBE (where x is the amount of HF exchange). The energy difference is at most 10kJ/mol and hence, the choice of the amount of HF exchange is more crucial than the type of the functional.

Results show a clear dependence on the amount of Hartree-Fock (HF) exchange. For all functionals, the energy increases as expected as the H atom from the hydrocarbon approaches the framework O nearest neighbour to the Mn active site. As the amount of HF exchange in the functionals increases, the transition state is lower in en-

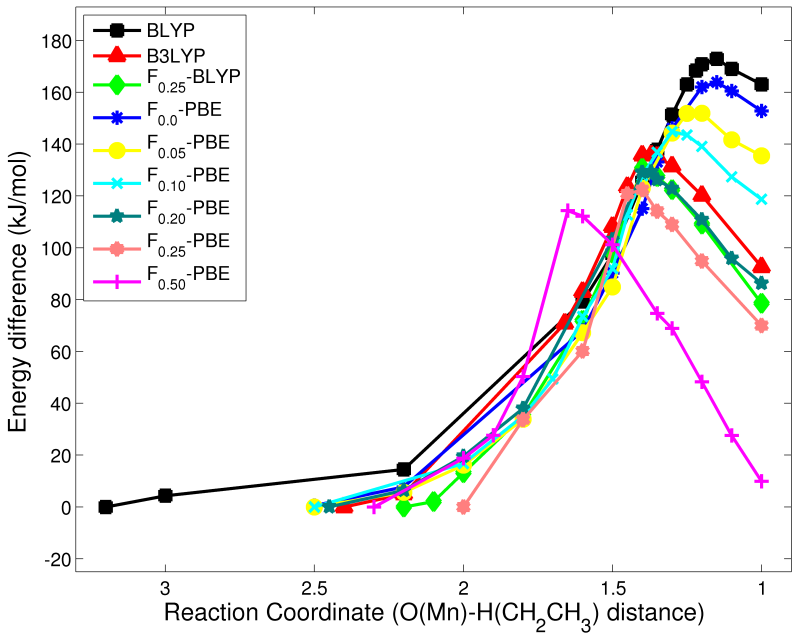

Figure 4.3: Energy profiles for the reaction step 1 calculated using nine functionals with different amount of HF exchange (BLYP, B3LYP, $F_{0.25}$-BLYP, F_0-PBE, $F_{0.05}$-PBE, $F_{0.10}$-PBE, $F_{0.25}$-PBE, $F_{0.50}$-PBE).

ergy and its geometry closer to the reactants. F_0-PBE and BLYP which are pure GGA functionals have a product-like TS and give very similar energy profiles. $F_{0.50}$-PBE, which has the largest amount of Hartree Fock exchange among those we considered here, has the most reactant-like TS.

The variation in reaction enthalpies is very large and the difference between functionals is up to 150 kJ/mol. This is a profound implication for chemistry. $F_{0.50}$-PBE has the lowest reaction enthalpy of 9.89 kJ/mol, while BLYP and F_0-PBE have the highest reaction enthalpies of 163.06 and 152.80 kJ/mol respectively. This is a very significant variation indeed which would correspond to an entirely different chemical behaviour. Clearly this difference deserves an in depth investigation for modelling to be a valid contributor to this and related catalytic studies.

	Activation Energy(kJ/mol)	Reaction Enthalpy(kJ/mol)	r_{OH}(TS)(Å)
BLYP	172.93	163.06	1.15
B3LYP	135.80	92.66	1.35
$F_{0.25}$-BLYP	130.66	78.58	1.40
F_0-PBE	163.86	152.80	1.15
$F_{0.05}$-PBE	151.93	135.51	1.20
$F_{0.10}$-PBE	144.81	118.72	1.30
$F_{0.20}$-PBE	129.29	86.32	1.37
$F_{0.25}$-PBE	122.43	69.97	1.40
$F_{0.50}$-PBE	119.0	9.89	1.65

Table 4.1: Activation energies and reaction enthalpies with the use of all nine functionals.

The large dependence on the amount of HF exchange is clear. To understand where it may arise from, we decomposed the overall reaction step into its component half reactions, the first being the reduction of Mn^{III} to Mn^{II} with atomic H, the other the oxidation of the alkane substrate:

$$Mn^{III} + H\cdot \rightarrow Mn^{II}\,(OH)$$

$$RH \rightarrow R\cdot + \cdot H$$

The calculated reaction enthalpies of the component half cells are reported in table 4.2, while figure 4.5 shows their variation as a function of the HF exchange fraction in the functional. The dissociation of ethane is affected only in minor way as the amount of HF exchange increases. It is clear that the difference in the overall redox energy originates in the calculated reduction potential of Mn in the AlPO framework. This

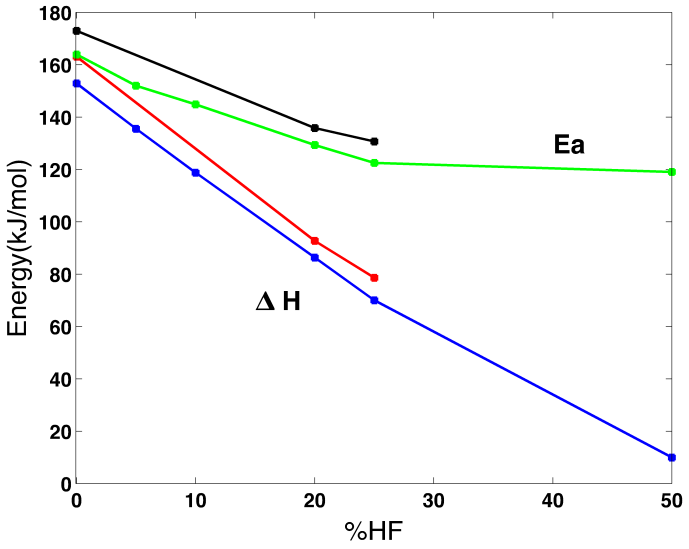

Figure 4.4: Calculated reaction enthalpies and activation energies as a function of the amount of HF exchange. With black and red are the relative values for F_x-BLYP functionals and with green and blue are for F_x-PBE functionals.

reduction requires a change from d^4 high spin to d^5 high spin electronic configuration through the localisation of an additional electron on the Mn^{3+} site. Such a situation is a typical example of an electronic state where the DFT solution is affected by a large SIE. To investigate further how the electronic configuration of Mn evolves during the reaction, in figure 4.6 we report the evolution of spin density on the Mn and C atoms as a function of the reaction coordinate for three different functionals.

Mn starts from a d^4 electronic configuration with four unpaired electrons localized in $3d$ atomic orbitals. On approaching the TS geometry, the spin on Mn starts to increase and undergoes an abrupt change from ~ 4 to ~ 5 when the energy reaches its maximum, i.e. at the TS, which confirms the homolytic character of the H transfer. Mn^{2+} and Mn^{3+} are both stable in high-spin electronic configuration because of the low ligand field splitting caused by the p donor character of O-based ligands as well as the tetrahedral coordination of the Mn ions. Pure DFT functionals, F_0-PBE and BLYP, are affected by the SIE, that spuriously destabilises localized electronic states, and hence

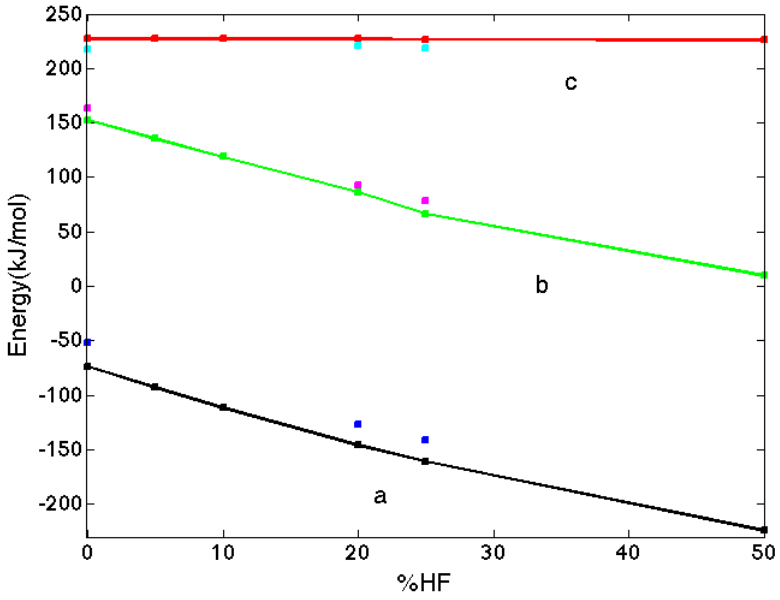

Figure 4.5: Calculated reaction enthalpies as a function of the amount of HF exchange for the component half cells (kJ/mol); a (Mn^{III} + H· → Mn^{II} (OH)), b (Mn^{III} + RH → R· + Mn^{II}(OH)) and c (RH → R· + ·H)

underestimate the stability of the d^5 Mn^{2+}. The SIE is corrected with the inclusion of orbital dependent exact-exchange with the hybrid exchange functionals. The increase of Hartree-Fock exchange from 20% in B3LYP, to 25% in $F_{0.25}$-PBE and 50% to F_{50}-PBE, progressively stabilises the high spin d^5 electronic configuration of Mn^{2+} relative to Mn^{3+}. The C-H bond remains stable as the hydrocarbon approaches the framework O up to a (R)H-O(Mn) distance of 1.7Å and energy increases substantially when the bond starts to dissociate. The spin of Mn (blue line) increases for all functionals approximately from ∼ 3.77(corresponding to Mn^{III}) to ∼ 4.83(Mn^{II}) simultaneously with the dissociation of the C-H bond and the H transfer to the Mn active site. The second product of this preactivation step is an ethyl radical (R·), whose unpaired electron is localized on one of the organic C atoms; the C spin (green lines in figure 4.6) changes from 0 to -1.0 with small variations depending on the functional, proving that the mechanism of the C-H bond cleavage is homolytic (C-H → C·+ ·H).

functional (HF%)	Mn^{III} + H· → Mn^{II} (OH)	RH → R· + ·H
BLYP	-51.7	217.1
B3LYP	-126.9	220.6
$F_{0.25}$-BLYP	-140.8	218.5
F_0-PBE	-73.3	227.1
$F_{0.05}$-PBE	-92.7	227.0
$F_{0.10}$-PBE	-111.5	227.0
$F_{0.20}$-PBE	-145.8	226.9
$F_{0.25}$-PBE	-161.0	226.7
$F_{0.50}$-PBE	-198.0	226.1

Table 4.2: Calculated reaction enthalpies of the component half-cells (kJ/mol); **Mn^{III} + H· → Mn^{II} (OH)** ($Mn(III) - O - P + \frac{1}{2}H_2 \rightarrow Mn(II) - OH - P$) and **RH → R· + ·H** ($CH_3CH_3(g) \rightarrow CH_3CH_2 \cdot + \frac{1}{2}H_2$)

In figure 4.7, we report the spin density maps for the transition state configuration for F_0-PBE and $F_{0.50}$-PBE functionals. The α spin density (red regions in figure 4.6) is strongly localized on Mn for both functionals. In the transition state, the β spin density (blue regions in figure 4.7) from the C-H bond is shared between the C atom of RH (which is becoming a radical) and the O of the framework which is nearest-neighbour to Mn active site. We observe that F_0-PBE functional gives a product like TS where the β spin is mostly localized on C, while $F_{0.50}$-PBE yields a reactant like TS where β spin is more on C, H and O atoms involved in the H transfer reaction. The H atom has much smaller spin density and intervenes the radical transfer from C to the framework. However, it does not itself become spin-polarized. The electron associated with the homolytic cleavage of the C-H bond is donated to the Mn^{III} site whose spin density increases upon approaching the TS. Alternatively, standard DFT has a more product like TS as the β spin is transferred completely and is well-localized on the radical carbon giving a product-like spin density.

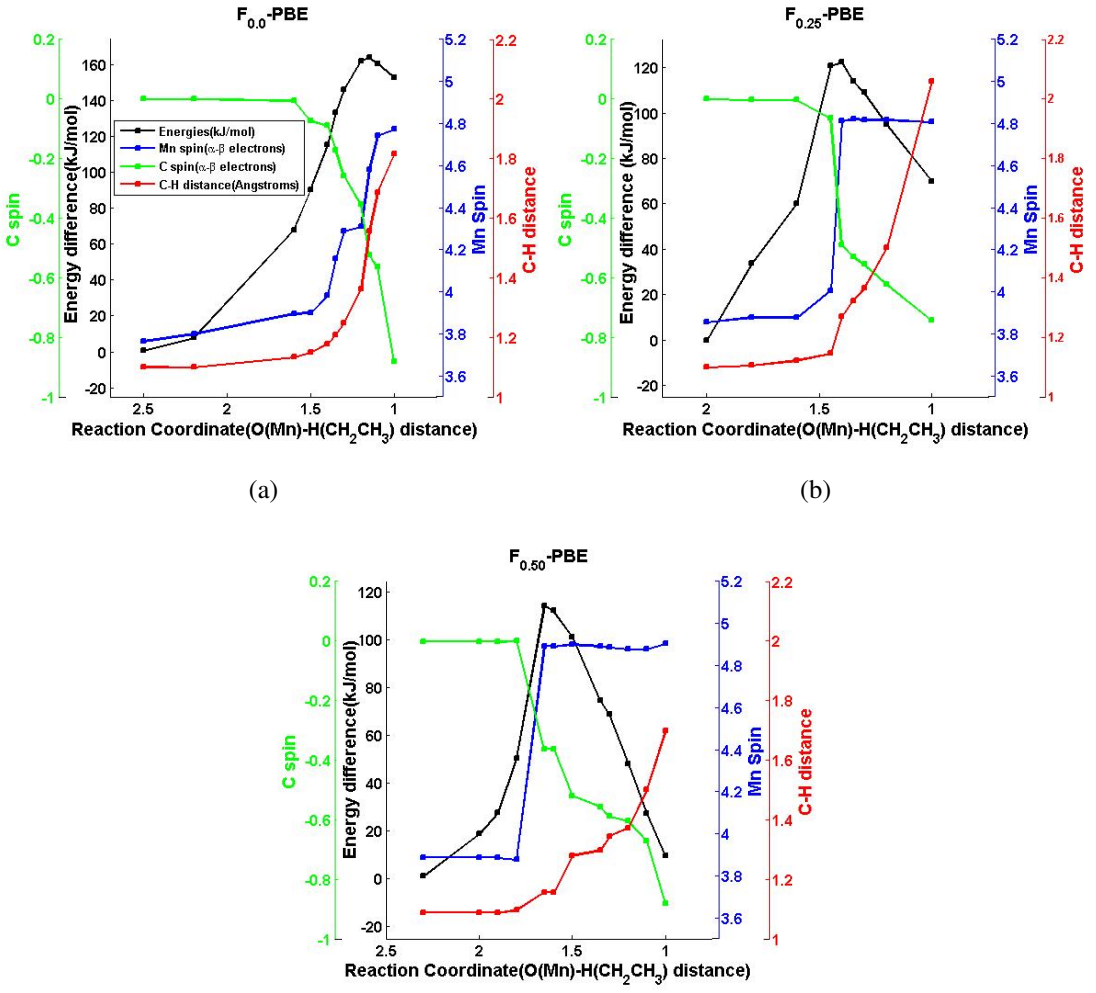

Figure 4.6: Reaction profile diagrams using F_0-PBE, $F_{0.25}$-PBE, $F_{0.50}$-PBE. Energy diagram (black line), evolution of Mn spin (blue line) and of C spin (green line), and C-H distance (red line) in Å along the reaction coordinate (O(Mn)-H(CH_2CH_3)) distance).

The hydrogen atom transfer to the framework O atom and the Mn reduction result in the elongation of all Mn-O bonds. Table 4.3 summarizes the Mn-O bond distance of the protonated oxygen along the reaction coordinate, r(OH). The largest Mn-O bond elongation is observed with the formation of the products, while with bold is noted the Mn-O bond distance on the TS. Although the O-H bond distance is different for

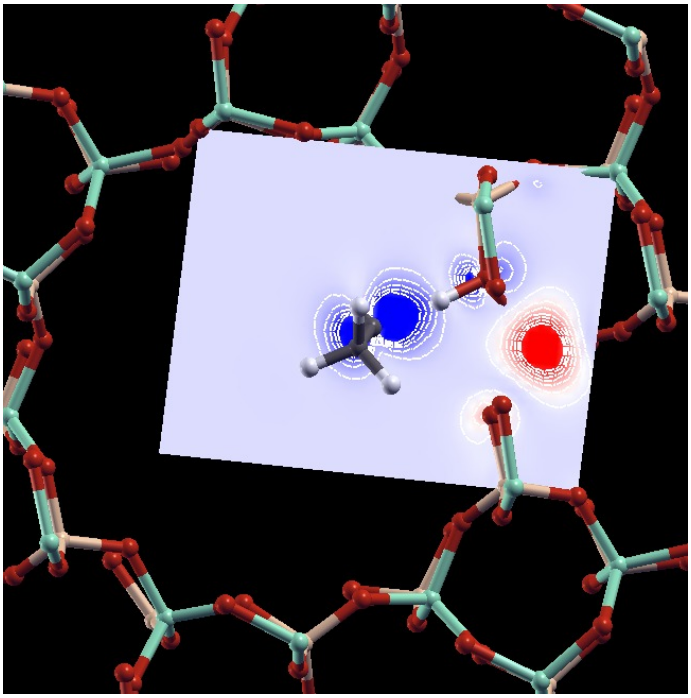

(a)

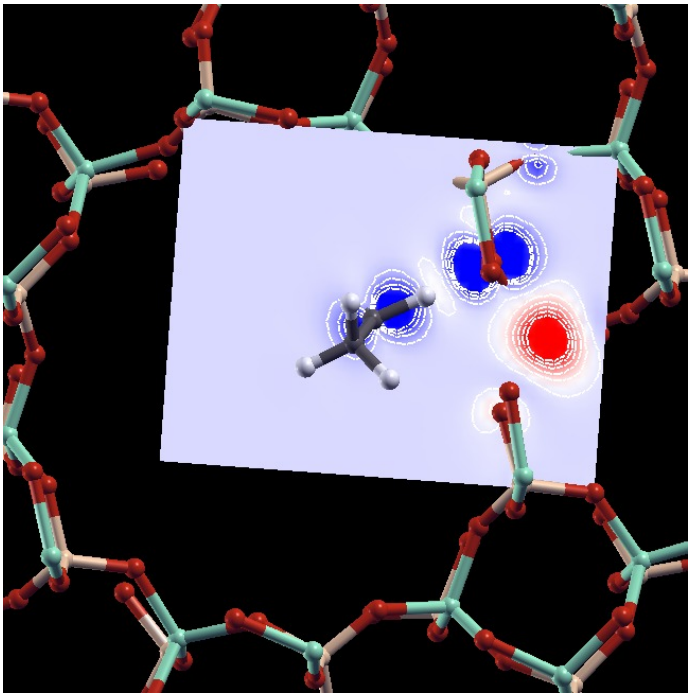

(b)

Figure 4.7: Spin density maps of the transition state of reaction step (1) of PBE with 0% (a) and 50% (b) of HF exchange. F_0-PBE functional gives a product like TS while higher amount of HF exchange gives a reactant-like TS.

r(O-H)Å	BLYP	B3LYP	$F_{0.25}$-BLYP	F_0-PBE	$F_{0.5}$-PBE	$F_{0.10}$-PBE	$F_{0.25}$-PBE	$F_{0.50}$-PBE
1.0	2.27	2.25	2.26	2.29	2.27	2.27	2.25	2.23
1.15	**2.19**			**2.19**				
1.2	2.10	2.20	2.21	2.10	2.17	2.20	2.20	2.20
1.3	2.0	2.17	2.14	2.0	**2.13**	**2.15**		
1.4	1.97	**2.15**	**2.14**	1.94	1.94	1.96	**2.14**	2.00
1.6	1.95	1.91	1.89	1.91	1.90	1.60	1.90	**2.17**
2.2	1.95	1.91	1.88	1.90	1.88		1.88	

Table 4.3: Mn-O bond distances in Å of the protonated oxygen.

every functional on the TS, the elongation of Mn-O bond is similar for all functionals, indicative of the Mn reduction.

4.3 *Propagation step* - H-transfer from RH to $Mn^{III} \cdots OR$

The second step we examine in detail is part of the radical propagation stage (reaction step 4.5a) which occurs on a $Mn^{III} \cdots OR$ site and involves a H transfer from a new hydrocarbon molecule in order to saturate the ethoxo radical RO·, and form an ethanol molecule ROH [42] (figures 4.8 and 4.9):

$$\text{Mn III (}\cdot\text{) OR} + \text{RH} \rightarrow \text{Mn III}\cdots\text{(ROH)} + \text{R}\cdot$$

The reaction coordinate chosen to represent this reaction step is the distance between the H atom in ethane that will be transferred and the radical O atom in RO·. In contrast to the preactivation step discussed previously, in this step Mn does not change oxidation state. Instead, it provides a stable site that stabilizes the ethoxo radical intermediate. In

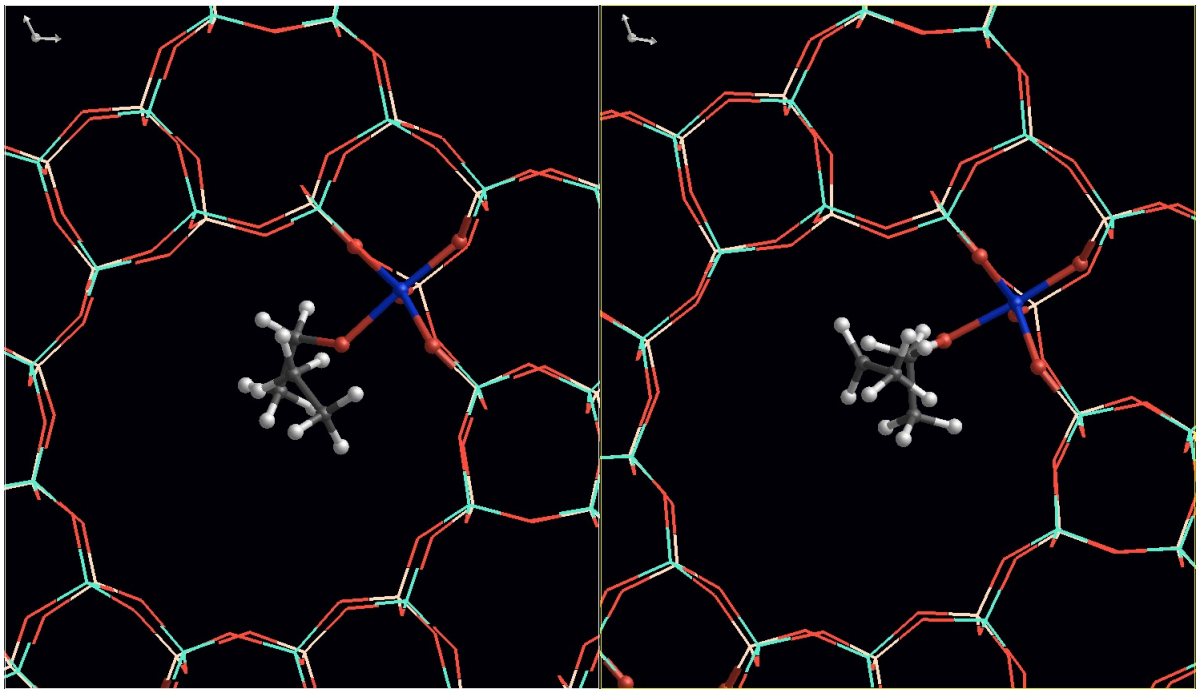

Figure 4.8: View of the TS (left) and product (right) structures for the propagation step. A hydrogen transfer to the active site takes place, yielding an ethyl (R·) radical.

this step, there is one unpaired electron throughout the process that is transferred from the O atom of the ethoxy intermediate (RO·) to C in the newly formed ethyl radical (R·). As previously, energy profiles were calculated for functionals with different amount of HF exchange.

In this reaction step, all functionals with less than 20% HF exchange converge to a different electronic state corresponding to $Mn^{IV} \cdots OH$, while the functionals with 25% or more HF exchange yield an ethoxo radical RO· coordinated to Mn^{III}. Because of the SIE intrinsic to GGA functionals, the Mn 3*d* levels are destabilized relative to the singly occupied molecular orbital containing the unpaired electron of the ethoxo radical.

In order to investigate why for functionals with less than 20% HF exchange the occupied *d* orbitals are shifted down in energy, we produced the density of state (DOS) projected from the atoms involved in the reaction to get information on the electronic

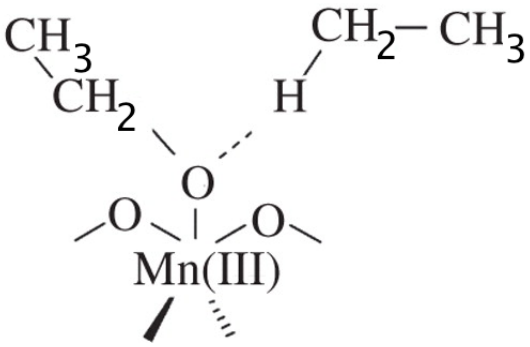

Figure 4.9: Reaction scheme showing the TS in propagation step.

structure. As shown in figure 4.10, for the F_0-PBE functional (figure 4.10a), there are two empty 3*d* α states on the Mn, indicative of the d^3 electronic configuration of Mn^{4+}, while the adsorbate O is a closed-shell species indicative of an OH^- ion. With the $F_{0.25}$-PBE functional (figure 4.10b), we have instead only one empty α state on Mn, indicative of Mn^{3+} oxidation state (d^4 configuration). The contribution from the adsorbate O shows an empty state with opposite spin with respect to the polarisation of Mn and hence, in this case an OH· radical. The filled Mn *d* levels shift down in energy relative to O-2*p* levels at the top of the valence band upon increasing the amount of HF exchange, showing that the SIE destabilizes the 3*d* orbitals giving a different electronic state.

Table 4.4 summarizes the activation energies and reaction enthalpies calculated with the functionals with more 20% HF exchange, whilst figure 4.11 shows the energy profiles along the reaction coordinate. The energy increases as the H atom of the hydrocarbon approaches the O· radical. As the amount of HF exchange increases in the functionals, the TS becomes slightly higher in energy. The variation is again a result of the SIE, but in this reaction step it plays in the opposite direction than in the preactivation step examined earlier. To understand how the self-interaction affects the activation barrier we need to investigate the extent of electronic localization in the TS relative to reactants and products. This is shown in figure 4.12. The difference between the activa-

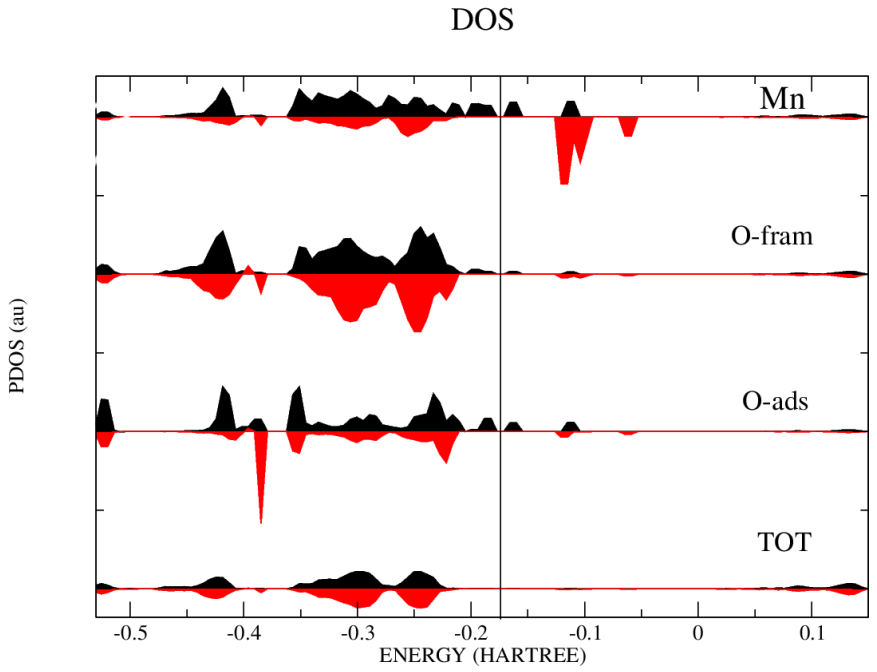

(a)

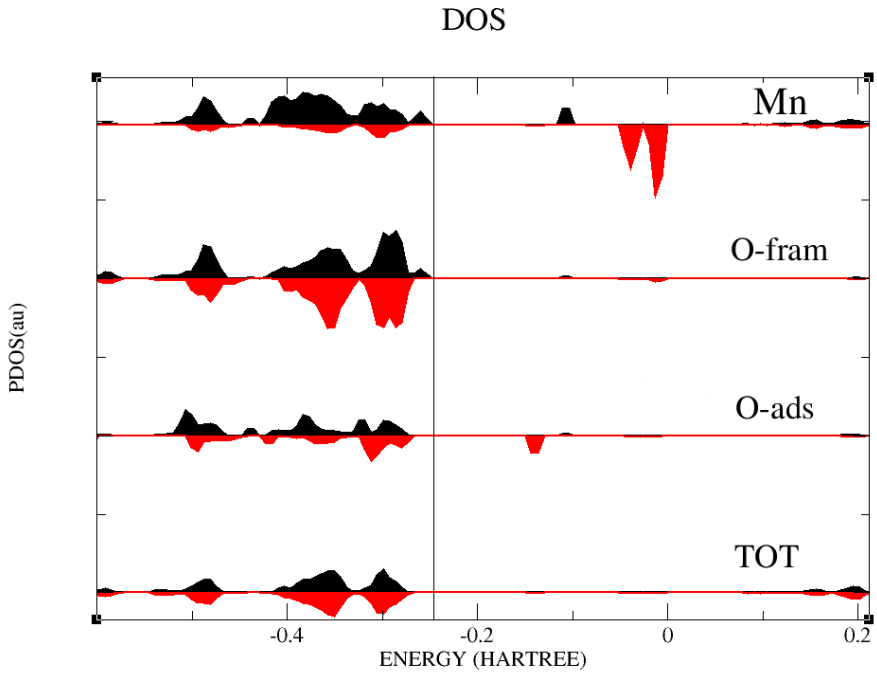

(b)

Figure 4.10: Projected density of states for Mn, O on the framework, O of the adsorbate, and total projection for PBE with 0% (a) and 25% (b) of HF exchange. The vertical line indicates the Fermi energy while black and red areas show the spin up and down contributions, respectively.

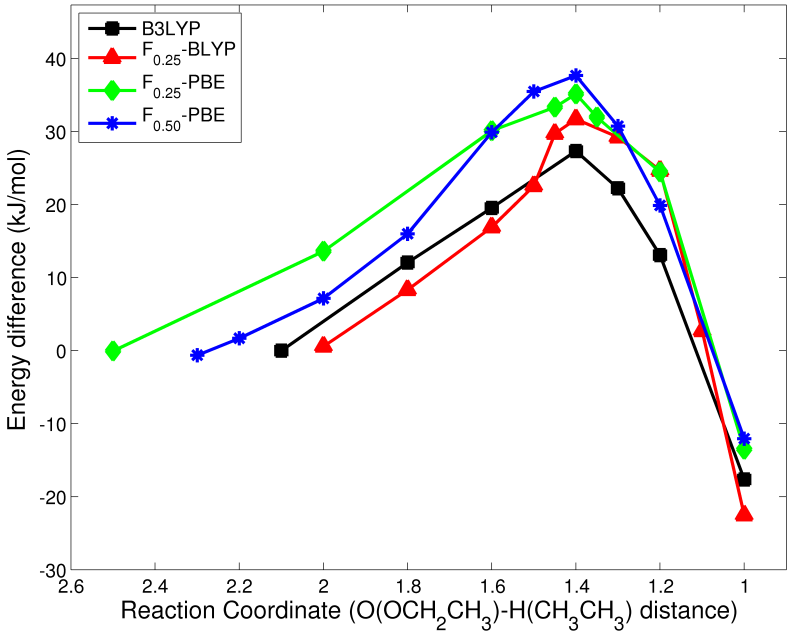

Figure 4.11: Calculated energy profiles for the reaction step 4.5a with different exchange functionals

	Activation Energy(kJ/mol)	Reaction Enthalpy(kJ/mol)	r_{OH}(TS)(Å)	spin on O at TS
B3LYP	27.34	-17.63	1.40	-0.58
$F_{0.25}$-BLYP	31.72	-22.51	1.40	-0.21
$F_{0.25}$-PBE	35.16	-13.49	1.40	-0.43
$F_{0.50}$-PBE	37.68	-12.05	1.40	-0.64

Table 4.4: Activation energies, reaction enthalpies, distances between the O which is nearest neighbour to the framework and the transferred H, as well as spin densities on O at the TS.

tion energy when using 20% of HF exchange and 50% is ~ 10kJ/mol with the highest energy for the 50% of HF, which is significantly smaller than the previous step (the difference between 20% and 50% ~ 61kJ/mol with the highest energy for the 20%).

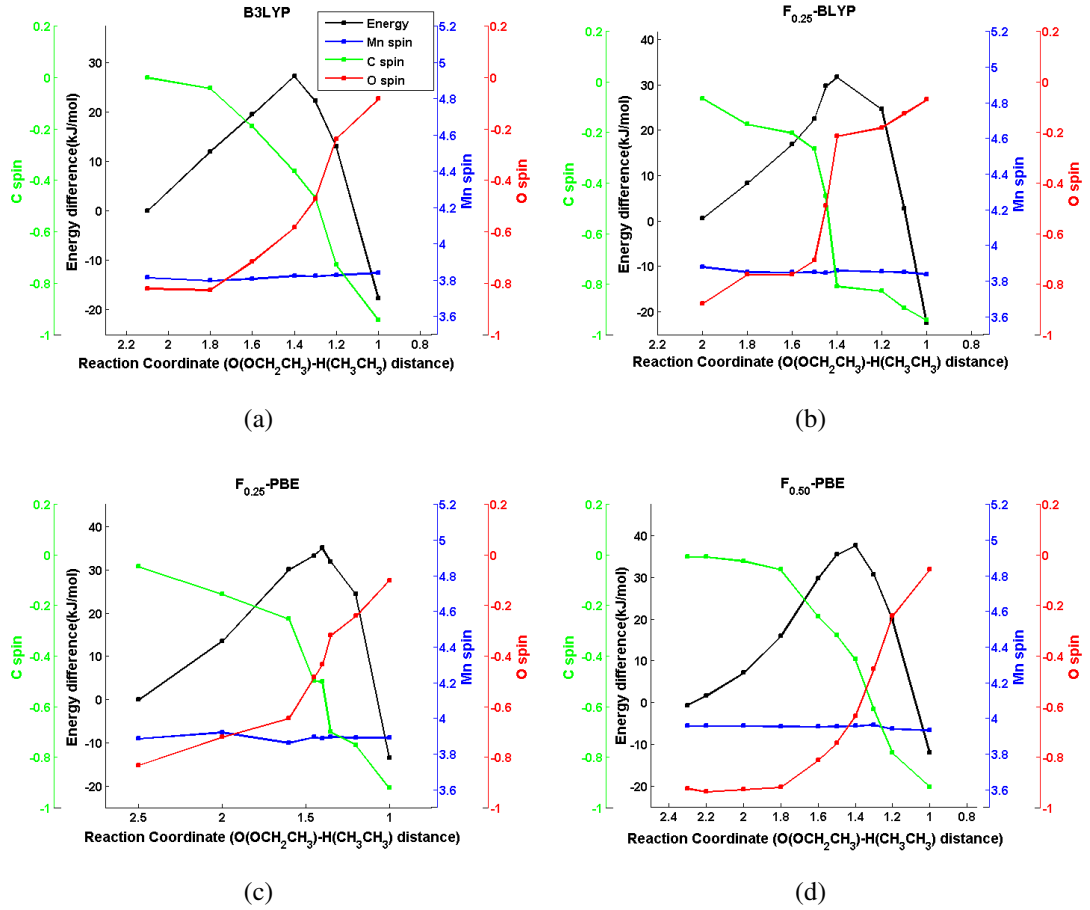

Figure 4.12: Reaction profile diagrams using B3LYP, $F_{0.25}$-BLYP, $F_{0.25}$-PBE and $F_{0.50}$-PBE. Energy diagram (black line), evolution of Mn spin (blue line), C spin (green line) and O spin (red line) along the reaction coordinate ($O(OCH_2CH_3)$-$H(CH_3CH_3)$) distance).

Figures 4.12 and 4.13 present information on how the spin polarization of the different species evolves along the reaction coordinate. Here, the oxidation state of Mn does not change; the spin of Mn (blue line) remains as $\sim$ 3.9 (corresponding to the d^4 for Mn^{III}) throughout the reaction. Instead, the unpaired electron of the organic radical is localized on a single atom in reagents and products, while it is delocalized among C and O atoms involved in the H transfer reaction, with only small contribution from H in the TS (figure 4.12). This increased delocalization is favoured by the self-interaction. The TS corresponds to the maximum delocalization of the unpaired electron. The disso-

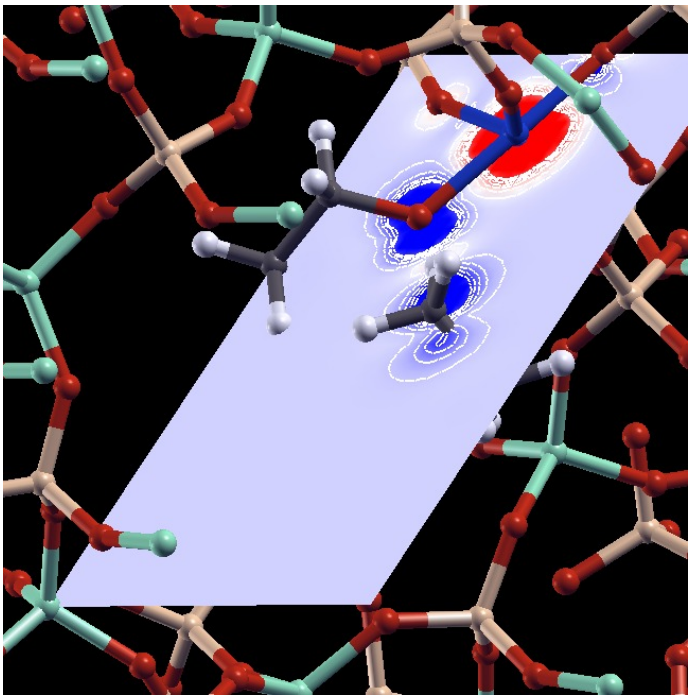

(a)

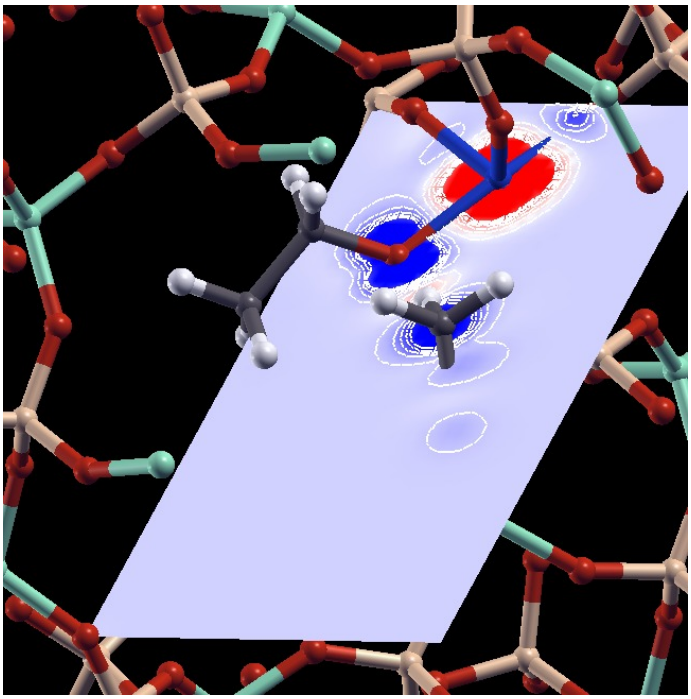

(b)

Figure 4.13: Spin density maps of the transition state of reaction step (7) of B3LYP (a) and PBE with 50% (b) of HF exchange.

ciation of the C-H bond takes place after the TS leading to the simultaneous formation of an ethyl radical R· and an ROH molecule that remains bonded to Mn. The change of C spin (green line) indicates the formation of the radical species while the initial unpaired electron localized on the O atom of the RO ligand) disappears as a result of the formation of a closed-shell species (ROH).

Delocalization at TS is confirmed in figure 4.13, where we present the spin density maps for the TS when B3LYP and PBE with 50% of HF exchange are used. We observe similar features for both functionals showing the smaller impact of SIE in this reaction step. Here the TS is not shifted to the reactants as the amount of HF increases but it appears when the O-H distance is ~1.4Å for all functionals. A well-localized α spin density on the Mn (displayed in red) remains unchanged, while the H atom is being transferred between the C and the O atom while the C atom retains a quasitetrahedral environment in the TS. The β spin density (displayed in blue) is shared between the C atom of RH (which is an incipient radical) and the O atom in the RO· ligand consistent with the homolytic dissociation of the C-H bond and the formation of an O-H bond.

4.3.1 Up and Down spin choices of oxygen radical

Figure 4.14 presents the energy profiles along the reaction coordinate for every functional separately. The two energy profiles in every diagram show how energy changes with the different amount of Hartree-Fock exchange and also how it changes for the two possible directions, up and down, of the spin of the oxygen radical. It should be mentioned that the energy of the reactants is obtained after full optimisation of the structure with the spin of the O radical up and as a result small differences on the zero point of the energy profile with spin down are observed. Although there are small differences when spin changes for B3LYP and $F_{0.25}$-PBE functionals, the spin down choice appear to be more stable for all functionals.

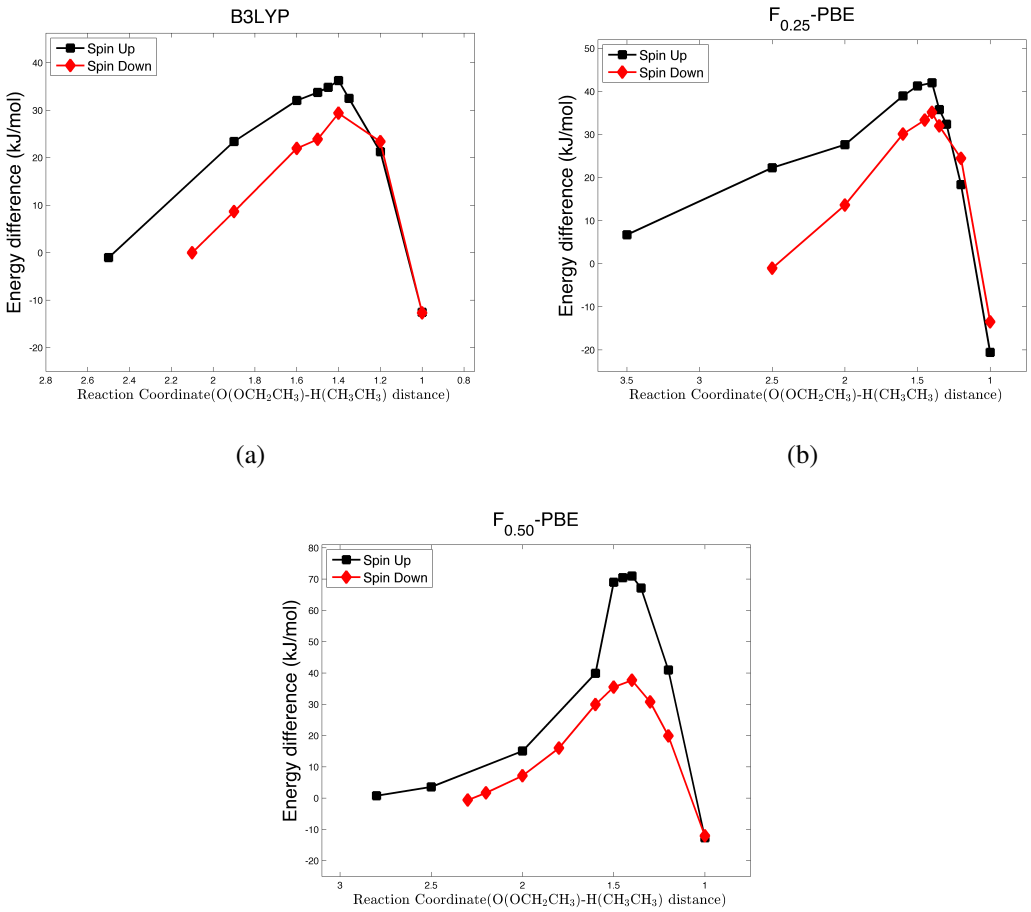

Figure 4.14: Calculated energy profiles of B3LYP, $F_{0.25}$-PBE and $F_{0.50}$-PBE functionals along the reaction coordinate distance for the two different spin directions, up (black line) and down (red line), of the radical O.

4.4 Summary and Conclusions

In this Chapter, we have identified computationally how reaction enthalpies and activation barriers of redox reactions vary with the use of different exchange functionals. The effect is large and must be treated carefully, especially when open-shell TM ions with localized *d* electrons are involved, as these are the systems where the SIE of DFT is most pronounced. The aim is to highlight the crucial role of SIE in redox reactions that proceed via radical mechanisms. For this reason, we focused on two representa-

tive steps of the aerobic oxidation of ethane catalyzed by Mn-doped nanoporous aluminophosphate catalysts discussed in [39] and [42]: the H transfer from ethane in the preactivation phase and one step of the propagation phase. SIE can increase or decrease the activation energy depending on the extent of electronic localization in each elementary reaction step.

The preactivation step occurs through reduction of Mn from 3+ to 2+ oxidation state and requires the localisation of an additional electron on the Mn ion while the electronic configuration changes from d^4 to d^5. This reaction is opposed by spurious SIE, hence we observe that the transition state becomes lower in energy with the increase of HF exchange. In particular, standard DFT functionals (PBE with 0% of HF and BLYP) yield reaction enthalpies and TS which are closer to the products and have the highest activation energies. They are unable to describe the reduction of Mn from 3+ to 2+ and they repel the electron density giving more delocalized solutions as the electron SIE becomes significant for electrons in the well-localized TM *d* levels. Hybrid exchange-correlation functionals may be used to alleviate the SIE and improper electron delocalization.

The propagation step does not require a change of oxidation state of the Mn active site, and is affected by the SIE in opposite way than the preactivation step discussed above. Here, the unpaired electron of the organic radical is delocalized between alkoxy and alkyl radical in the transition state, which is stabilized by the SIE. As a consequence, the calculated activation barrier becomes slightly higher upon increasing the fraction of Hartree-Fock exchange, while the reaction coordinate at the TS state is at 1.4Å for all functionals.

As DFT is widely used in catalytic studies, the accurate examination of reaction energies and activation barriers for transforming among reactants, adsorbed species, and products is needed. Further calibration of current functionals and greater availability of experimental model systems for benchmarking would help to clarify the reliability of the methods being used and extend the applicability of the density func-

tional calculations in similar redox reactions. For our system, as there are not many experimental model systems in order to validate our results, we need to find alternative comparisons to experiment. In the next chapter we consider that the Mn^{3+}/Mn^{2+} redox chemistry we observed here is the same exploited in the intercalation chemistry of $LiMnPO_4$ model and thus, we calculate the Li intercalation potential of $LiMnPO_4$ with a range of functionals with different amount of HF exchange, in the same way as in this chapter.

Chapter 5

Li intercalation potential of olivine phosphate cathodes - A comparative study of electronic structure calculations

5.1 Introduction

In Chapter 2, we discussed the aerobic oxidation of hydrocarbons in TM-doped aluminophosphates which is a specific example where theory has played a vital role in providing molecular detail over the whole and quite complex catalytic cycle [40]. In the catalytic reaction examined, redox activity is associated with a TM ion such as Mn, Fe, Co that replaces framework Al^{3+} sites and reversibly changes between 3+ and 2+ oxidation states during the catalytic cycle. The TM is co-ordinated in the lattice to four of the phosphate PO_4^{3-} molecule ions. Describing the localisation of electrons in the *d* atomic orbitals of TM ions at the core of redox reactions, is a weakness of local and semi-local DFT functionals that are affected critically by the self-interaction error (SIE). The SI is present in all DFT calculations but it becomes catastrophic when the electronic states are well localised, such as for *3d* TM ions.

In Chapter 4, we extended the above computational work on the catalytic oxidation of alkanes in MnAlPO-5 to cover different GGA and hybrid exchange functionals. There we showed that the critical reaction enthalpy and activation barrier for the H abstraction from the hydrocarbon (HC) substrate by Mn^{3+}, to yield an alkyl radical Mn^{2+}, vary as much as 150 kJ/mol upon varying the amount of HF exchange in hybrid exchange functionals between 0 and 50%, which would completely alter the kinetics and mechanism of the catalytic cycle.

Clearly a reliable way of refining this range must be found possibly by direct comparison to experiment, to establish confidence in the computational results. Unfortunately, the energetics of individual elementary steps in a complex catalytic cycle is not currently possible to estimate exactly. The insulating nature of the AlPO framework prevents the applications of electrochemical methods such as cyclic voltammetry that could quantify the Mn^{3+}/Mn^{2+} reduction potential of the redox active ions in real samples. We need therefore to find alternative comparisons to experiment.

Here we exploit the fact that the Mn^{3+}/Mn^{2+} redox chemistry and local environment of Mn directly bonded to phosphate ions, is the same observed in the intercalation chemistry of $LiMnPO_4$ exploited in Li battery cathodes. The shortcomings of DFT in localising an additional electron on Mn^{3+} during the catalytic cycle and the Li intercalation are very similar. The redox potential of $LiMnPO_4$ is well characterised quantitatively through its Li battery applications, hence $LiMnPO_4$ provides a suitable reference to assess the DFT results also in the heterogeneous catalytic applications of MnAlPO's. The study of $LiMnPO_4$ is complemented by that of $LiFePO_4$ to estimate transferability of results between different redox active TM ions. Both $LiMnPO_4$ and $LiFePO_4$ are olivine structure compounds and figure 5.1 shows the adopted structure.

In previous studies, Zhou *et al.* [113] claimed that the use of the DFT+U method gives Li intercalation potentials in good agreement with experiment while Wang *et al.* [8] used DFT+U to correct the SIE in the calculation of reaction energies of TM oxides. Chevrier *et al.* [111] performed hybrid density functional calculations of redox

potentials and formation energies of TM compounds and they have shown that the exact Hartree-Fock (HF) exchange in the HSE06 hybrid exchange functional corrects the self-interaction errors leading to a more accurate solution when the 3*d* electrons are involved. In addition, the inclusion of HF exchange has more recently gained increased prominence in solid state chemistry [44, 112, 140]. The general performance of hybrid functionals in solid state chemistry has been discussed in detail by Corà *et al.* [104] while B3LYP has been also proved successful for calculations of simple TM oxides [104, 141, 142].

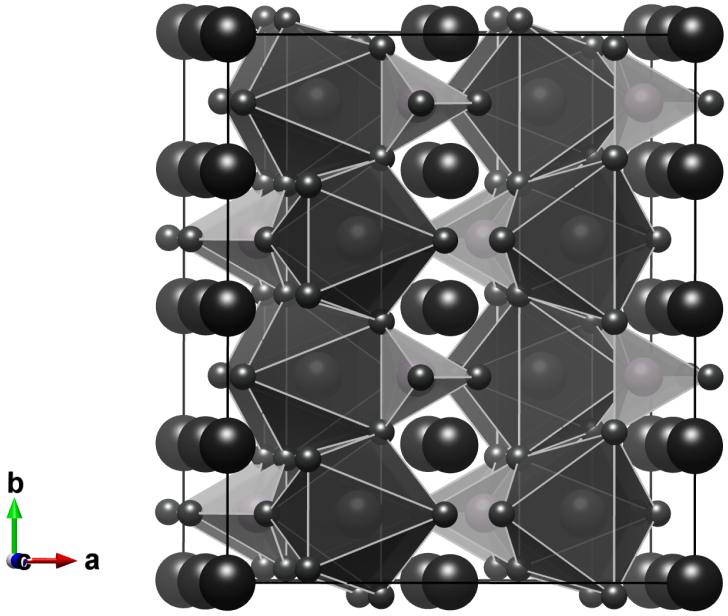

Figure 5.1: Schematic representation of $LiMPO_4$ olivine structure with PO_4 tetrahedra in light grey and MO_6 octahedra in dark grey. Li is represented by the black spheres in the interstitial channels.

In this Chapter, we perform density functional theory calculations using GGA and hybrid exchange functionals with different amounts of HF exchange in order examine how the amount of HF exchange can influence the intercalation potential of the topical

olivine structures, $LiMnPO_4$ and $LiFePO_4$. Beyond the quantitative study of materials of technological interest, our aim is to provide a reliable benchmark of different exchange DFT functionals for the study of redox reactions, that can be applied to other scientific areas that critically depend on these widespread elementary chemical steps.

5.2 Approach and Methodology

The olivine structure consists of a distorted hexagonal close-packed (hcp) framework containing Li and M (Mn or Fe) in octahedral sites and P in tetrahedral sites, as shown in figure 5.1. During battery cycling the Li ions are removed topotactically to yield heterosite, which maintains the topology of the MPO_4 framework [143].

The detailed methodology has been already described in Chapter 3. The average intercalation potential for Li in $LiMPO_4$ has been calculated from the below equation:

$$\langle V \rangle = -[E(LiMPO_4) - E(MPO_4) - E(Li)], \tag{5.1}$$

where E is the total calculated energy (in eV) and as the equation shows, $\langle V \rangle$ is determined by computing the total energy of three compounds: $LiMPO_4$, MPO_4 and metallic Li.

Experimental structures of $LiMPO_4$ were taken from the inorganic crystal structure database(ICSD) [144] while the delithiated ones were obtained after removing all Li atoms from the lithiated structures, followed by full geometry optimisation. Ferromagnetic (FM) and several antiferromagnetic (AFM) orderings of TM atoms were examined and the ordered magnetic phase with lowest energy was used to calculate intercalation potentials. We present the results from the AFM orderings. For completeness we note that at high temperatures these compounds will have magnetic disorder [145]. Full geometry optimisations of all phases were performed with each functional.

	a(Å)		b(Å)		c(Å)	
	$LiMnPO_4$	$MnPO_4$	$LiMnPO_4$	$MnPO_4$	$LiMnPO_4$	$MnPO_4$
BLYP	10.56	9.81	6.17	6.01	4.82	4.89
B3LYP	10.50	9.70	6.13	5.97	4.78	4.84
$F_{0.25}$-BLYP	10.51	9.70	6.13	5.97	4.78	4.84
$F_{0.35}$-BLYP	10.48	9.65	6.12	5.94	4.76	4.82
F_0-PBE	10.47	9.69	6.13	5.95	4.78	4.83
$F_{0.05}$-PBE	10.46	9.67	6.12	5.94	4.77	4.82
$F_{0.10}$-PBE	10.45	9.65	6.11	5.94	4.76	4.82
$F_{0.20}$-PBE	10.43	9.62	6.10	5.92	4.74	4.80
$F_{0.25}$-PBE	10.43	9.60	6.09	5.91	4.74	4.79
$F_{0.35}$-PBE	10.40	9.57	6.08	5.89	4.72	4.77
$F_{0.40}$-PBE	10.39	9.55	6.07	5.88	4.71	4.76
PBE [4]	10.55	9.92	6.13	6.01	4.78	4.93
PBE+U [4]	10.62	9.98	6.17	6.07	4.80	4.96
Exp. [1]	10.44	9.69	6.09	5.93	4.75	4.78

Table 5.1: Cell parameters for the olivine-structured $LiMnPO_4$ and $MnPO_4$.

5.3 Results and discussion

5.3.1 Structural parameters

Tables 5.3 and 5.4 present the calculated equilibrium volumes as well as the volume differences (ΔV) between lithiated and delithiated phases. For comparison, GGA, GGA+U and HSE06 results from Ceder's group [4] are also presented together with the experimental results. The relative errors in the volumes are plotted in figure 5.2 and tables 5.3 and 5.4 present the values of volumes for lithitated and delithiated structures, as well as the volume differences.

The experimental data have been obtained at room temperature where these compounds are known to be paramagnetic. Since our calculations are static the zero-point vibration and thermal effects, which we are neglecting, would introduce a very small discrepancy.

	a(Å)		b(Å)		c(Å)	
	$LiFePO_4$	$FePO_4$	$LiFePO_4$	$FePO_4$	$LiFePO_4$	$FePO_4$
BLYP	10.27	10.01	6.10	5.96	4.73	4.93
B3LYP	10.25	9.91	6.05	5.86	4.70	4.87
$F_{0.25}$-BLYP	10.26	9.91	6.05	5.85	4.70	4.86
$F_{0.35}$-BLYP	10.24	9.87	6.04	5.82	4.69	4.84
F_0-PBE	10.15	9.91	6.06	5.87	4.69	4.87
$F_{0.05}$-PBE	10.16	9.92	6.05	5.86	4.68	4.87
$F_{0.10}$-PBE	10.17	9.88	6.05	5.84	4.68	4.85
$F_{0.20}$-PBE	10.18	9.85	6.03	5.81	4.67	4.83
$F_{0.25}$-PBE	10.16	9.84	6.01	5.80	4.66	4.82
$F_{0.35}$-PBE	10.16	9.81	6.01	5.77	4.65	4.80
$F_{0.40}$-PBE	10.15	9.79	6.00	5.76	4.64	4.79
PBE [4]	10.39	9.99	6.04	5.93	4.90	4.76
PBE+U [4]	10.42	9.92	6.07	6.01	4.76	4.93
Exp.[51]	10.33	9.82	6.01	5.79	4.69	4.79

Table 5.2: Cell parameters for the olivine-structured $LiFePO_4$ and $FePO_4$.

For all compounds investigated, BLYP functionals overestimate more the values of the lattice parameters compared to the PBE functionals, while in both functionals as the amount of HF exchange increases the lattice parameters contract. Our results are consistent with those found in the previous studies. However, for precise comparison with the previous calculations we should consult the references provided, since different basis sets, magnetic orderings or exchange correlation functions, have been used. Although our atomic orbital calculations and the earlier plane-wave calculations with the same GGA functional should give the same results, there are some small differences which are usual. The agreement is good for $LiMnPO_4$ where we have Mn^{2+}. However, for $MnPO_4$ we have the biggest discrepancy, but the unit cell parameters with our calculations are closer to the experimental results compared to the results of Ceder's group. We are confident about the accuracy of our calculations since Mn^{3+} in $MnPO_4$ is

a Jahn-Teller ion with d^4 electronic configuration and pseudo-potentials are not always reliable in describing such valence state.

The predicted volume decreases from M=Mn, Fe and in general, they decrease steadily upon increasing the fraction of HF exchange, in parallel with the increased electronic localisation achieved. The volumes for $LiMnPO_4$ obtained with all BLYP functionals are larger than those with PBE functionals, while with PBE functionals, when the amount of HF exchange is closer to 20%, the lithiated volume is predicted exactly (only 0.03% relative error). In $LiFePO_4$, B3LYP and $F_{0.25}$-BLYP functionals predict the lithiated volume very well with a relative error of 0.10% and 0.14%, respectively. However, the equivalent amount of HF exchange with $F_{0.20}$-PBE and $F_{0.25}$-PBE functionals underestimate the volumes giving relative errors of -1.7% and -2.4%, respectively.

The error and variability compared to experiment is greater for delithiated structures corresponding to complete topotactic removal of all Li ions. Compensation of errors is noted in the calculated volume differences (tables 5.3 and 5.4) upon delithiation. Comparison of the calculated volume differences with the experimental value (ΔV = 6.83Å^3/formula unit) for $LiMnPO_4$ indicates that there is a good agreement with all functionals with B3LYP predicting the volume difference exactly.

However, as in previous computational investigations [4, 111], the prediction of the volume change for $LiFePO_4$ is underestimated for all functionals, but it becomes closer to the experimental value as the amount of HF exchange increases. In particular, the prediction of volume change with $F_{0.40}$-PBE (ΔV = 3.13Å^3/formula unit) is in better agreement with the experimental value (ΔV = 4.76Å^3/formula unit) than the rest of the functionals with smaller amount of HF exchange (ΔV < 3.02Å^3/formula unit).

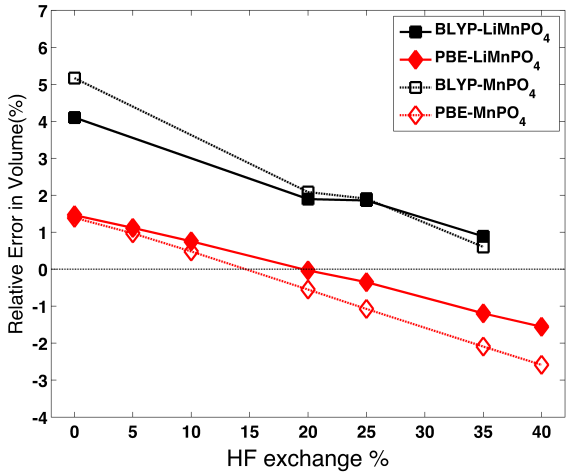

(a)

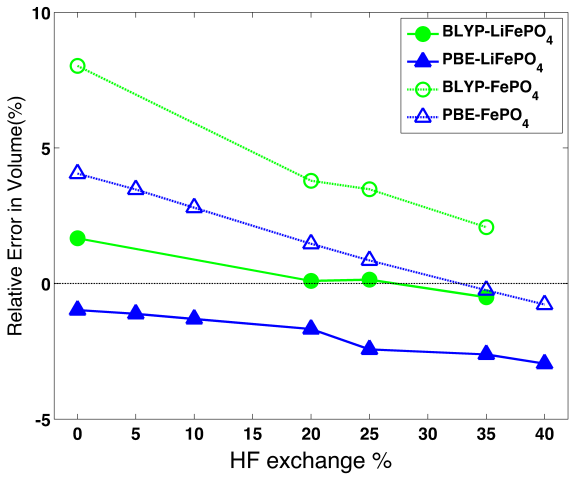

(b)

Figure 5.2: Coloured lines indicate the relative error of the optimized volumes compared to experiment for the lithiated structures of (a) $LiMnPO_4$ and (b) $LiFePO_4$. Lighter, open symbols indicate corresponding delithiated phases

5.3.2 Cell voltages

Equation (5.1) was used to obtain the Li intercalation potentials which are plotted in figure 5.3a as a function of HF exchange and the values are presented in tables 5.3 and 5.4. Experimental values are also listed.

	V(Å^3)		ΔV	Voltage
	$LiMnPO_4$	$MnPO_4$	(Å^3)	(eV)
BLYP	314.38	288.86	25.52	3.34
B3LYP	307.73	280.40	27.33	4.18
$F_{0.25}$-BLYP	307.61	279.91	27.70	4.36
$F_{0.35}$-BLYP	304.68	276.32	28.36	4.69
F_0-PBE	306.41	278.49	27.92	3.16
$F_{0.05}$-PBE	305.37	277.33	28.04	3.37
$F_{0.10}$-PBE	304.28	275.99	28.29	3.60
$F_{0.20}$-PBE	301.90	273.16	28.74	3.99
$F_{0.25}$-PBE	300.94	271.72	29.22	4.17
$F_{0.35}$-PBE	298.39	268.93	29.47	4.49
$F_{0.40}$-PBE	297.30	267.56	29.73	4.65
PBE [4]	309.13	293.92	15.21	2.99
PBE+U [4]	314.52	300.47	14.05	4.04
HSE06 [111]	302.80	283.72	19.08	3.87
Exp. [1]	302.00	274.67	27.33	4.1

Table 5.3: Volume of the olivine-structured $LiMnPO_4$ and and $MnPO_4$ and intercalation potentials.

For $LiMnPO_4$ as the amount of HF exchange increases and becomes closer to 25%, hybrid exchange functionals successfully reproduce experimental intercalation potential giving an average error of 0.02 eV. The excellent agreement of PBE with 20% of HF exchange, where the discrepancy compared to experiment is less, is in line with recent studies [104] where the optimum weight of HF exchange for a solid-state specific hybrid functional was suggested to be at least 20%. With more than 25% of HF exchange, the calculated potentials are overestimated with an average discrepancy of 0.55 eV compared to experiment. For $LiFePO_4$, comparison of the calculated results with increasing amount of HF exchange indicate that B3LYP and $F_{0.25}$-BLYP perform well in predicting the experimental value (3.5eV) as they give intercalation potentials of 3.46 eV and 3.59 eV, respectively. PBE functionals give slight different results as they

	V(Å^3)		ΔV	Voltage
	$LiFePO_4$	$FePO_4$		
BLYP	296.26	294.23	2.03	2.87
B3LYP	291.67	282.69	8.98	3.46
$F_{0.25}$-BLYP	291.80	281.84	9.97	3.59
$F_{0.35}$-BLYP	289.92	278.03	11.89	3.75
F_0-PBE	288.53	283.41	5.12	2.57
$F_{0.05}$-PBE	288.13	281.81	6.32	2.73
$F_{0.10}$-PBE	287.58	279.99	7.59	2.91
$F_{0.20}$-PBE	286.50	276.36	10.14	3.16
$F_{0.25}$-PBE	284.32	274.69	9.63	3.29
$F_{0.35}$-PBE	283.77	271.70	12.07	3.43
$F_{0.40}$-PBE	282.79	270.26	12.52	3.51
PBE [4]	298.09	290.28	7.81	2.84
PBE+U [4]	309.13	293.92	15.21	3.47
HSE06 [111]	291.68	280.00	11.68	3.33
Exp.[51] [48]	291.39	272.36	19.02	3.5

Table 5.4: Volume of the olivine-structured $LiFePO_4$ and $FePO_4$ and intercalation potentials.

underestimate the intercalation potential, but those with 35% and 40% of HF exchange yield values closer to experiment with $F_{0.40}$-PBE predicting the intercalation potential exactly.

General trends can be established for the cell voltages of both $LiMnPO_4$ and $LiFePO_4$. With the use of standard DFT functionals, the intercalation potentials are underestimated by 1 V for both olivine structures, but become closer to the experimental values with the addition of HF exchange. Similar trend was observed in heterogeneous catalysis [146], where the activation barrier of the reaction studied, vary as much as 150 kJ/mol upon the change of HF exchange used. The difference in the intercalation potential as the amount of HF exchange increases can be attributed to the SIE. In particular, with the lithiation, the electronic configuration changes from d^4 to d^5 for

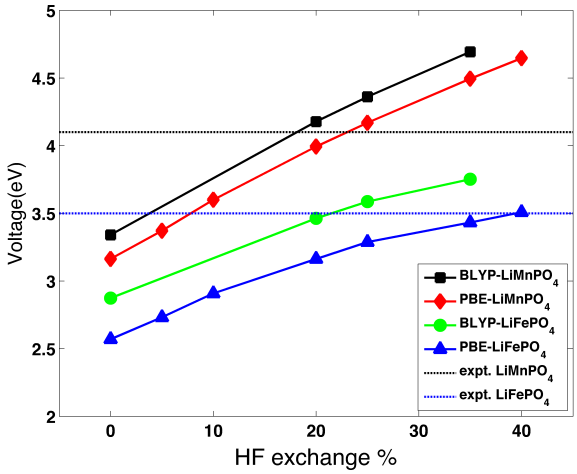

(a)

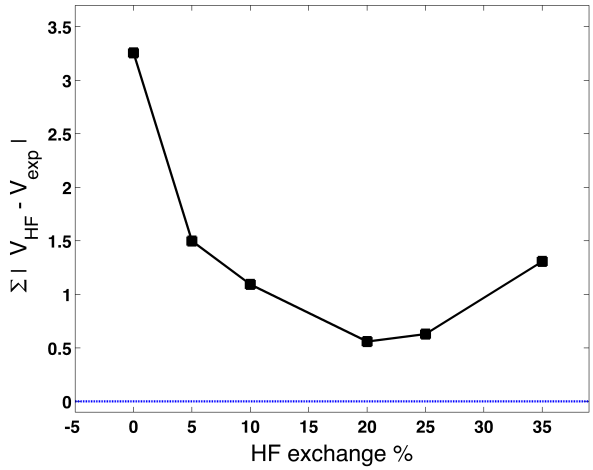

(b)

Figure 5.3: (a) Li intercalation potentials of $LiMnPO_4$ and $LiFePO_4$ olivine structures with different amounts of HF exchange and (b) Average deviation from experiment as a function of HF exchange.

$LiMnPO_4$ and from d^5 to d^6 for $LiFePO_4$ resulting the localisation of an extra electron. Standard DFT functionals oppose such a localisation due to the SIE, and thus leading to underestimated voltages. Compensation of SIE is observed as the amount of HF exchange increases. By adding HF exchange, the penalty of adding a new electron is less

and thus, the 2+ oxidation state is more stable than the 3+, leading to a more positive intercalation potential.

Figure 5.3b shows the total error for each amount of HF exchange compared to experiment, deriving after summing the absolute errors in modulus from both BLYP and PBE functionals and from both $LiMnPO_4$ and $LiFePO_4$ structures. We conclude that the inclusion of 20%-25% of HF exchange minimises the total error and can give results very close to the experiment.

5.3.3 Electron density

As we have argued, transition metal ions with *d* electrons are sensitive to the details of the Hamiltonian, as these are the systems where the SIE of DFT is most pronounced. With the use of standard DFT functionals, the spurious SIE destabilises the localised electronic states giving extended electron densities. In figure 5.4 we present the total electron density of $LiFePO_4$ for the ferromagnetic system with the use of PBE with 0% of HF exchange. The map is drawn in a plane containing one Fe-O-Fe. The continuous black line is the isodensity levels calculated from the spin density.

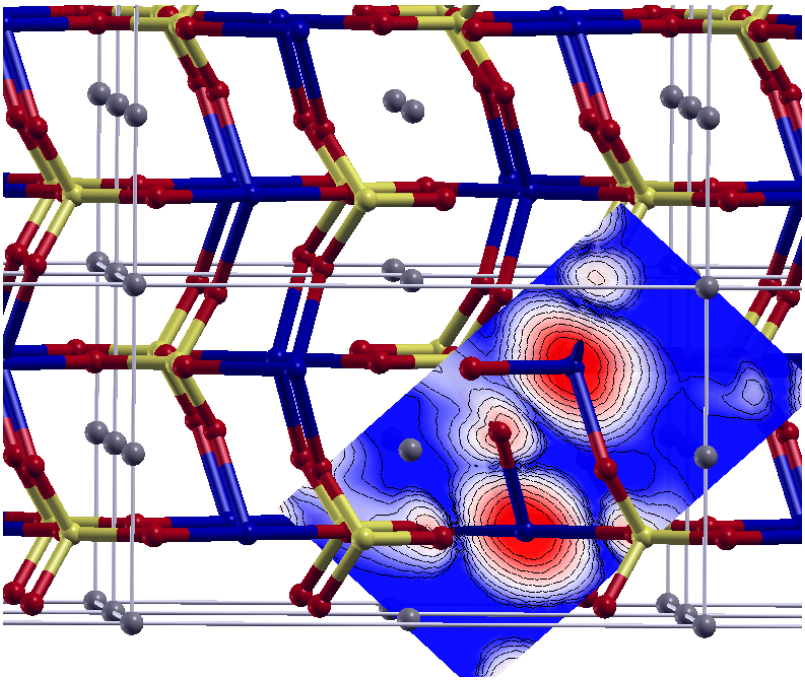

Figure 5.4: Electron density map for the ferromagnetic $LiFePO_4$ system with the use of F_0-PBE. The α spin is indicated in red. Fe is represented in blue, P in yellow, Li in grey and O in red.

The distribution of the spherical electron density around the Fe atoms is indicated with red. We haven not observed substantial differences in the density maps between different functionals, as in contrast to the MeAlPO system examined before, every single site is occupied by the same TM and the perturbation is much larger, while in AlPOs

	$LiMnPO_4$		$LiFePO_4$	
	Mn	O	Fe	O
BLYP	4.73	0.026	3.70	0.028
B3LYP	4.82	0.021	3.81	0.022
$F_{0.25}$-BLYP	4.83	0.021	3.82	0.020
$F_{0.35}$-BLYP	4.85	0.020	3.85	0.018
F_0-PBE	4.77	0.019	3.72	0.025
$F_{0.05}$-PBE	4.80	0.018	3.76	0.024
$F_{0.10}$-PBE	4.82	0.017	3.79	0.022
$F_{0.20}$-PBE	4.85	0.015	3.84	0.020
$F_{0.25}$-PBE	4.86	0.014	3.84	0.017
$F_{0.35}$-PBE	4.88	0.013	3.86	0.016
$F_{0.40}$-PBE	4.89	0.012	3.87	0.015

Table 5.5: Mulliken charges on M (Mn and Fe) and on O for $LiMnPO_4$ and $LiFePO_4$.

there was only site occupied by a TM and all the perturbation was due to that defect. As a result, the changes in density maps between functionals are not big enough as the spin can not spread due to the repetition of the defect.

However, the trends are similar to those observed in MeAlPO and the symptoms of standard DFT functionals are still there. Figure 5.5 shows the spin density on Mn and Fe in numbers for both lithiated and delithiated structures, while the values of Mulliken population analysis for Mn, Fe and O are presented in table 5.5. Via these results we can compare the population of the valence atomic orbitals on the TM. The transition metal ions investigated have a partially filled *d* shell, with electronic configuration ranging between the d^5 of Mn^{2+}, to the d^6 of Fe^{2+}. Standard DFT functionals delocalise and spread the electron density on the *d* transition metals while hybrid exchange functionals with more than 20% of HF exchange can give more localised results. The (calculated) electron density ρ shows spin localisation on the TM and less contribution of O along the bonds, as the amount of HF increases.

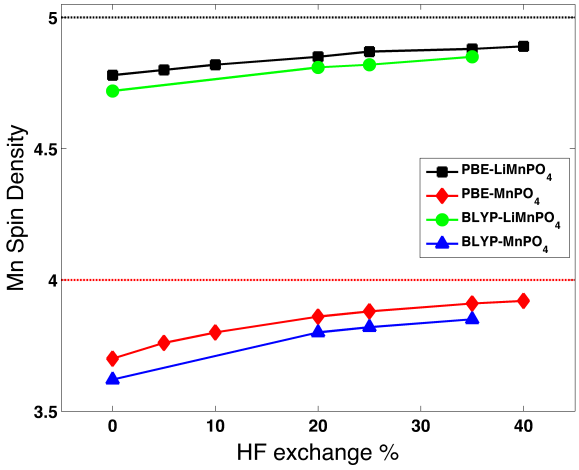

(a)

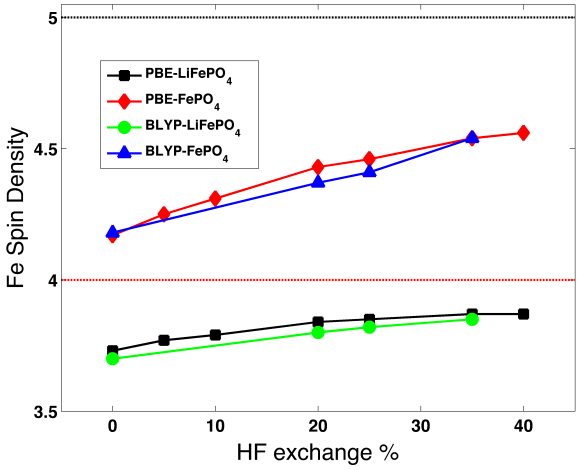

(b)

Figure 5.5: a) Mn spin density for $LiMnPO_4$ and $MnPO_4$ and b) Fe spin density for $LiFePO_4$ and $FePO_4$ along different amount of HF exchange.

5.4 Summary and Conclusions

We analysed the redox behaviour of olivine $LiMnPO_4$ and we found it similar to that of MnAlPO-5 system examined in Chapter 4, as Mn change its oxidation state from 3+ to 2+ and the localization of an extra electron takes place. Since there are no experimental investigations to compare our results deriving from Chapter 4, in this chapter we calculated the Li intercalation potential of $LiMPO_4$ (M=Mn and Fe) in order to compare the performance of different functionals. Standard DFT functionals are known to fail in describing accurately redox reactions where well localized *d* electrons are involved. The electron self-interaction places the occupied *d*-levels too high in energy while the oxidation potential is too low, and as result the Li intercalation potential is systematically underestimated. Here we have presented a benchmark of GGA and hybrid functionals with different amount of HF exchange from 0% to 40%, in order to show how crucial is the choice of a functional with redox reactions.

The results suggest that the M^{3+}/M^{2+} redox potential in $LiMnPO_4$ and $LiFePO_4$ olivine structures are in agreement with theoretical predictions when hybrid functionals with more than 20% of HF exchange are used, while standard DFT functionals and functionals with less than 20% of HF exchange underestimate the potentials due to the self-interaction error. As the amount of HF exchange decreases a strong self-interaction systematically penalizes a reduced state with more *d* electrons over an oxidized state, resulting in an underestimation of intercalation potentials. The cancellation of self-interaction on the *d* orbitals with the use of hybrid functionals improves the accuracy of the calculations.

Standard DFT functionals can poorly describe localized electrons and for our system Mulliken population analysis has shown that for functionals with high amounts of HF exchange (> 20%) the electrons are more localised around the TM. In agreement with the experimental data, hybrid functionals with 20-25 % of HF exchange, describe very well the intercalation potential of $LiMnPO_4$, while in $LiFePO_4$, this is the case when B3LYP and PBE with 40% of HF exchange are used. In general, high amounts

of HF exchange are much more successful than GGA in predicting intercalation potentials in the presence of localized electrons and the exact amount depends on the TM used, whilst the shortcomings of the standard DFT functionals and those with low HF exchange ($< 20\%$) are crucial.

The results indicate that similar amounts of HF exchange should be used in modelling other processes, including heterogeneous catalysis involving redox reactions of TM ions.

Chapter 6

Mn-doped nanoporous aluminophosphate catalysts for the regioselective aerobic oxidation of hydrocarbons

6.1 Introduction

Modelling can play important role in determining the kinetics and mechanism of catalytic cycles and this information can be used to design new Single-Site-Heterogeneous Catalysts (SSHCs) with improved selectivity. In this Chapter we make reference to the catalytic cycle described in Chapter 2, where the aerobic oxidation of ethane catalysed by Mn-doped AlPO-5 (AFI) has been revealed. In this catalytic cycle, the hydrocarbon molecules are oxidised at the C atom that undergoes the initial H abstraction reaction in order to form the alkyl radical R·. Thus, selectivity arises in the steps where the homolytical cleavage of C-H bond takes place and a hydrogen atom is abstracted. We examine how the reaction steps 4.1(preactivation) and 4.5a (propagation) can be employed to analyze the factors controlling selectivity. These two representative steps are the same as those we examined in Chapter 4; the first is the abstraction of H from ethane

in the preactivation phase (reaction step 4.1), which involves a reduction of the Mn^{III} site to Mn^{II}. The second step comes from the propagation phase of the catalytic cycle, where Mn does not change oxidation state (reaction step 4.5a). In a saturated hydrocarbon molecule, inductive effects cause the decrease of C-H bond strength when moving from primary to secondary and tertiary carbon atoms, which in turn results in a easier abstraction of H from secondary (tertiary) atoms. Consequently, in the gas phase, the oxidation at a secondary C atom is thermodynamically favoured, though the terminal oxidation at primary C atoms yields more desirable products. With microporous catalysts the modification of relative reactivity of primary and secondary C atoms of the substrate can be achieved by steric factors.

The aim is to show any selectivity issues related to functionalization of primary and secondary carbon atoms and if, by choosing the aluminophosphate with the appropriate pore size, we may impose steric constraints in order to reveal enhanced reactivity of the terminal methyl groups. Figure 6.1 presents the pore structures of AlPO-5 and AlPO-34. We argue that, with MnAlPO-5, there is no end-on restriction of entry of the propane into the active site due to the large pore diameter. Even when the constraints are increased with the propagation step, the reaction is still thermodynamically controlled and the oxidation takes place on the secondary C atom. In MnAlPO-34 we observe that although there are some steric constraints imposed from the smaller pores, the oxidation of a linear alkane is still favoured on the secondary C atom.

We have already discussed the calculated energetics for the aerobic oxidation of ethane catalysed by Mn-doped nanoporous aluminophosphates with the AFI structure (MnAlPO-5). While our use of ethane as the model hydrocarbon prevents us from discussing directly selectivity issues related to this catalytic oxidation, in this Chapter we change our hydrocarbon substrate from ethane to propane and then hexane in order to examine the activation of differently functionalized substrates. Further selectivity analysis is achieved by using aluminophosphate frameworks with different pore-size.

In particular, we change the AFI structure to the smaller CHA structure (MnAlPO-34), illustrated in figure 6.1.

We used the same computational methodology as in Chapter 4 and the majority of calculations were performed with B3LYP hybrid exchange functional. However, in the last part of this chapter we present a computational investigation when the amount of HF increases from 20% in B3LYP to 50% in $F_{0.50}$-PBE.

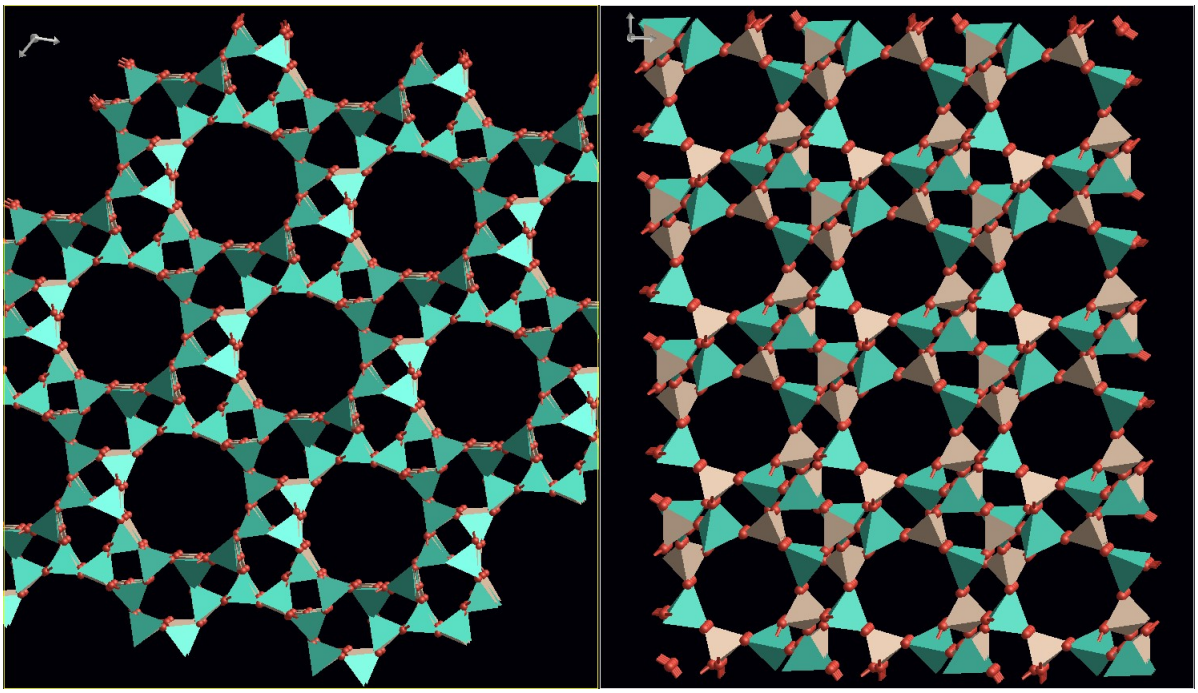

Figure 6.1: Structure of the AlPO-5 on the left and of the AlPO-34 on the right highlighting the different pore sizes available. Pore apertures are respectively 7.3 Å and 3.8 Å.

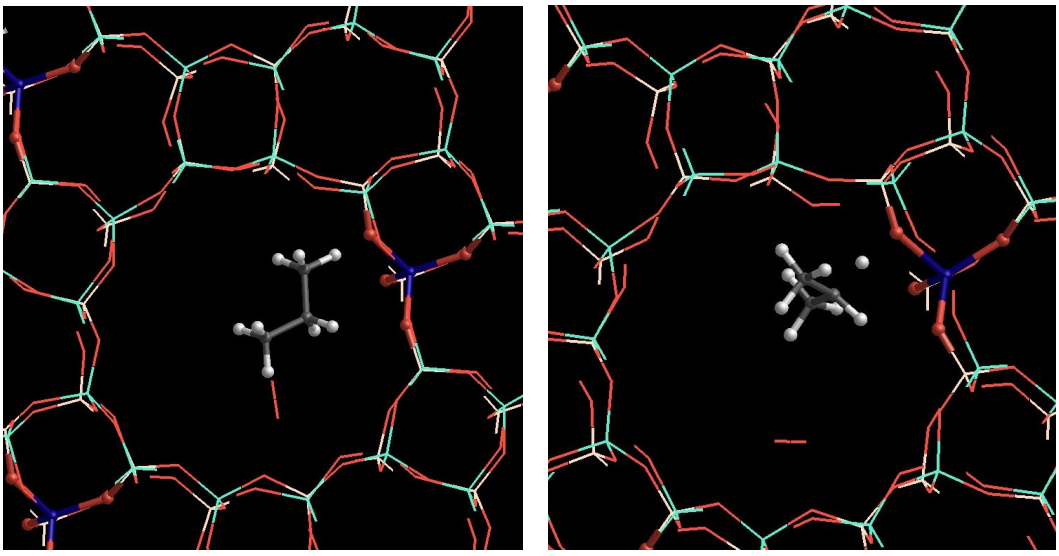

(a) (b)

Figure 6.2: View of the TS for the preactivation step. A hydrogen transfer to the active site takes place, yielding a Mn^{II} site and (a) a propyl or (b) an isopropyl radical is formed. Mn active site is represented in blue, P in brown, Al in green and O in red.

6.2 Results and Discussion

6.2.1 Ethane VS Propane

6.2.1.1 *Preactivation step*: Formation of the R· and reduction of Mn^{III} using MnAlPO-5 and MnAlPO-34

As already explained, the first part of our study considers the initial elementary step (reaction step 4.1) of the preactivation phase [39]. In the presence of O_2 and an alkane, the reduction of the Mn active site takes place through homolytic transfer of a hydrogen atom from RH to the active site (figures 6.2 and 6.3).

Mn^{III} (O) + RH $\rightarrow$ Mn^{II} (OH) + R·

As discussed in Chapter 2, a bond is formed between the H of the hydrocarbon molecule and one O of the framework which is nearest neighbour to Mn.

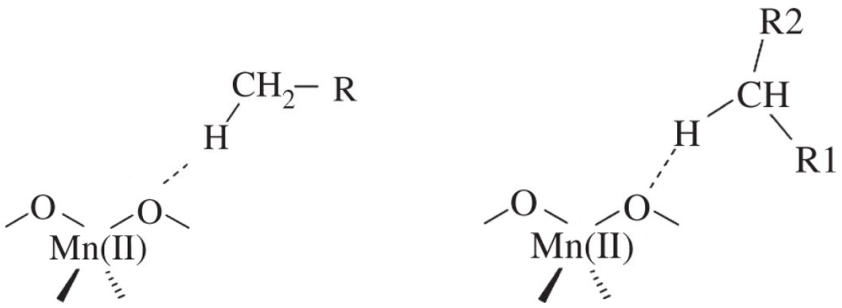

(a) (b)

Figure 6.3: Reaction scheme showing the TSs in the preactivation step corresponding to selectivity to oxidation at (a) primary and (b) secondary C atoms.

	MnAlPO-5		MnAlPO-34	
(kJ/mol)	ΔH	Ea	ΔH	Ea
H-abstraction from CH_3CH_3	92.66	135.8	130.28	158.99
H-abstraction from primary C atom of $CH_3CH_2CH_3$	105.49	143.54	129.58	163.81
H-abstraction from secondary C atom of $CH_3CH_2CH_3$	71.14	110.87	110.56	153.47
maximum Δ(ΔE)	34.35	32.67	19.82	10.34

Table 6.1: Summary of the energies (reaction enthalpies ΔH and activation energies Ea in kJ/mol) of the H abstractions from ethane and propane for both MnAlPO-5 and MnAlPO-34 frameworks.

Table 6.1 summarises the reaction enthalpies and activation barriers for all four combinations of different structures: MnAlPO-5 with ethane, MnAlPO-5 with propane, MnAlPO-34 with ethane and MnAlPO-34 with propane. Figure 6.4 illustrates the relevant reaction profiles. In the case where propane is used as substrate, we need to

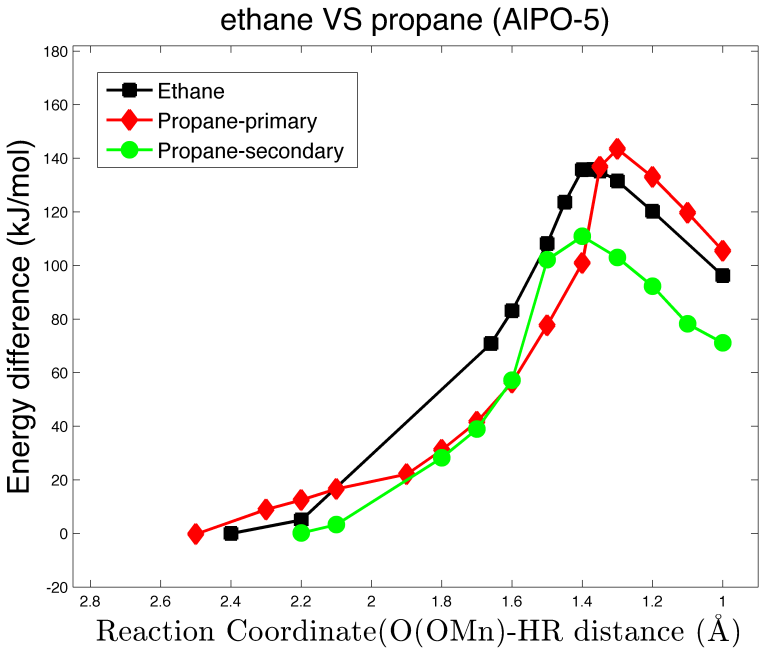

(a)

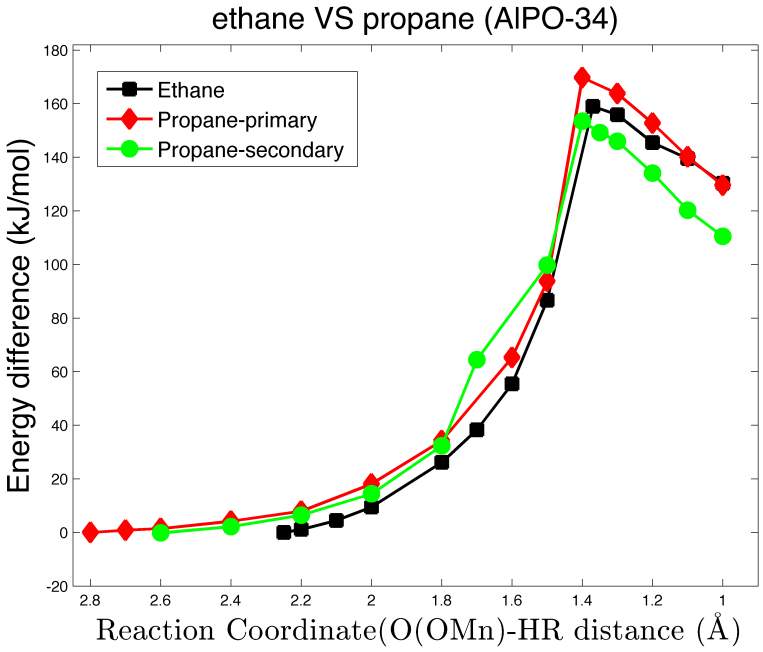

(b)

Figure 6.4: Energy profiles for the H transfer from ethane(black line) from primary C of propane(red line) and from secondary C of propane(green line) for (a) MnAlPO-5 and (b) MnAlPO-34 frameworks.

examine the barrier for both combinations where an H atom is transferred from the primary carbon of the propane and from the secondary carbon (figure 6.2). With the MnAlPO-5 catalyst we observe that reaction enthalpy and activation energy are sufficiently lower when the reaction takes place on the secondary C atom of propane. The energy difference from the oxidation on primary C atom is 32.67 kJ/mol and 34.35 kJ/mol for reaction enthalpy and activation energy, respectively. Thus, the AFI structure is not able to modify the reactivity typical of the gas-phase propane molecule. This result is not surprising given the relatively large dimension of the AFI channels as the 12-MR channels of AFI structure allow for the high flexibility of hydrocarbons and only in the TS exert limited steric constraints. It is, however, reasonable to suggest that in order to control selectivity of the oxidation, structural constraints should be imposed by frameworks whose pore dimensions are closer to the size of the hydrocarbon that is functionalized in this very first reaction step of the catalytic cycle. Thus, the MnAlPO- 34 framework is chosen whose microporous frameworks have smaller pore dimensions (8-MR). From figure 6.4, we observe that MnAlPO-34 can actually impose constraints on the bulkier TS rising from the activation of secondary C atom. However, the reaction is again dominated by thermodynamic factors as the calculated activation energy is lower when the reaction takes place on the secondary C atom but the difference between primary and secondary C oxidation is smaller than in the AFI structure - only a 10.34 kJ/mol difference in the activation energy. As shown in figure 6.4, the use of MnAlPO-34 gives sufficiently higher reaction enthalpies as well as transition states confirming the substantial effect of frameworks with smaller pore dimensions.

It is clear from the energy plots in this thesis that the points we have identified as a TS represent a maximum in one direction and not a cusp. As we have already described in our methodology section in Chapter 3, earlier work [39] confirmed that we had the right TS within the step of reaction coordinate sampling used, giving results that are close to those obtained using second derivative-based methods (usually less than 2 kJ/mol). This difference is negligible when considering that the wrong choice of

functional gives an error of up to 150 kJ/mol, as in Chapter 4. In this chapter, selected transition state configurations were confirmed by calculating the vibration harmonic frequencies. Figure 6.5 shows part of the output file from the calculation of vibrational frequencies of our system when an H is transferred from primary C atom of propane in MnAlPO-34 framework. If we can discount all numerical errors, we would have only one imaginary phonon. However, we have one very high negative frequency while the values of modes 2 and 3 are very small. This is because we have two sources of numerical noise. Firstly, the reaction coordinate is sampled at discrete steps of 0.1 Å, hence the TS will be known at best within a chosen step of 0.01 Å close to the TS. Secondly, second derivatives are calculated numerically. A typical phonon calculation in an optimised geometry would give numerical values for the three translation modes in the order of +/-15 cm^{-1}. The numerical sampling of the reaction coordinate can cause a doubling of the numerical error. The data below are within those boundaries, giving confidence to our results.

```
HHHHHHHHHHHHHHHHHHHHHHHHHHHHHHHHHHHHHHHHHHHHHHHHHHHHHHHHHHHHHHHHHHHHHHHHHHHHHHHHHHHHHHHHHHHHHHHHHHHHH
EIGENVALUES (EIGV) OF THE MASS WEIGHTED HESSIAN MATRIX AND HARMONIC
FREQUENCIES. IRREP LABELS REFER TO SYMMETRY REPRESENTATION ANALYSIS;  A AND I
INDICATE WHETHER THE MODE IS ACTIVE OR INACTIVE, RESPECTIVELY, FOR IR AND
RAMAN; IR INTENSITIES IN BRACKETS.

CONVERSION FACTORS FOR FREQUENCIES:
     1 CM**(-1) =   0.2194746E+06 HARTREE
     1 THZ      =   0.2997925E-01 CM**(-1)

HHHHHHHHHHHHHHHHHHHHHHHHHHHHHHHHHHHHHHHHHHHHHHHHHHHHHHHHHHHHHHHHHHHHHHHHHHHHHHHHHHHHHHHHHHHHHHHHHHHHH

   MODES         EIGV          FREQUENCIES     IRREP  IR    INTENS     RAMAN
              (HARTREE**2)   (CM**-1)     (THZ)              (KM/MOL)
   1-   1   -0.2849E-04  -1171.5427  -35.1220  (A  )   A (      0.00)   A
   2-   2   -0.5857E-07    -53.1144   -1.5923  (A  )   A (      0.00)   A
   3-   3   -0.7058E-08    -18.4382   -0.5528  (A  )   A (      0.00)   A
   4-   4    0.2270E-08     10.4559    0.3135  (A  )   A (      0.00)   A
   5-   5    0.6780E-08     18.0718    0.5418  (A  )   A (      0.00)   A
   6-   6    0.1781E-07     29.2864    0.8780  (A  )   A (      0.00)   A
   7-   7    0.2166E-07     32.3027    0.9684  (A  )   A (      0.00)   A
   8-   8    0.3616E-07     41.7352    1.2512  (A  )   A (      0.00)   A
   9-   9    0.5339E-07     50.7117    1.5203  (A  )   A (      0.00)   A
  10-  10    0.6233E-07     54.7934    1.6427  (A  )   A (      0.00)   A
  11-  11    0.1128E-06     73.7173    2.2100  (A  )   A (      0.00)   A
  12-  12    0.1454E-06     83.6757    2.5085  (A  )   A (      0.00)   A
  13-  13    0.1622E-06     88.3858    2.6497  (A  )   A (      0.00)   A
  14-  14    0.1839E-06     94.1294    2.8219  (A  )   A (      0.00)   A
```

Figure 6.5: The output file from the calculation of vibrational frequencies.

6.2.1.2 *Propagation step* - H-transfer from RH to $Mn^{III} \cdots$ OR using MnAlPO-5 and MnAlPO-34

The second step we examine in detail is part of the propagation phase (reaction 4.5a) which occurs on a $Mn^{III} \cdots OR$ site and involves an H transfer from a new hydrocarbon molecule in order to saturate the ethoxo radical RO·, and form an ROH molecule [42] :

$$Mn^{III}(\cdot)\,OR + RH \rightarrow Mn^{III} \cdots (ROH) + R\cdot$$

This step does not take place on a bare Mn active site but on an O-based radical ligated to Mn^{III} and involves two molecular species.

Figure 6.6 shows the reaction profile in the propagation step when AlPO-34 is used as framework and ethane as substrate. We examine how the energy changes for the two possible directions, up and down of the spin of the oxygen radical. Although the differences are very small, the down choice with the use of AlPO-34 framework is again more stable as with AlPO-5 as already presented in Chapter 4; all following calculations were performed with the spin down choice.

In order to examine the activation of secondary C atoms in a hydrocarbon, we have changed our substrate from ethane to propane creating a larger molecular species in our system. The presence of the ligated RO radical may modify significantly the steric requirements of the C-H bond cleavage because of the restricted environment provided by the microporous framework of MnAlPOs. The activation of a secondary C atom may yield a bulkier TS (see figure 6.7) than that from the activation of primary C atoms and further modification of the relative reactivity of primary and secondary C atoms might be expected.

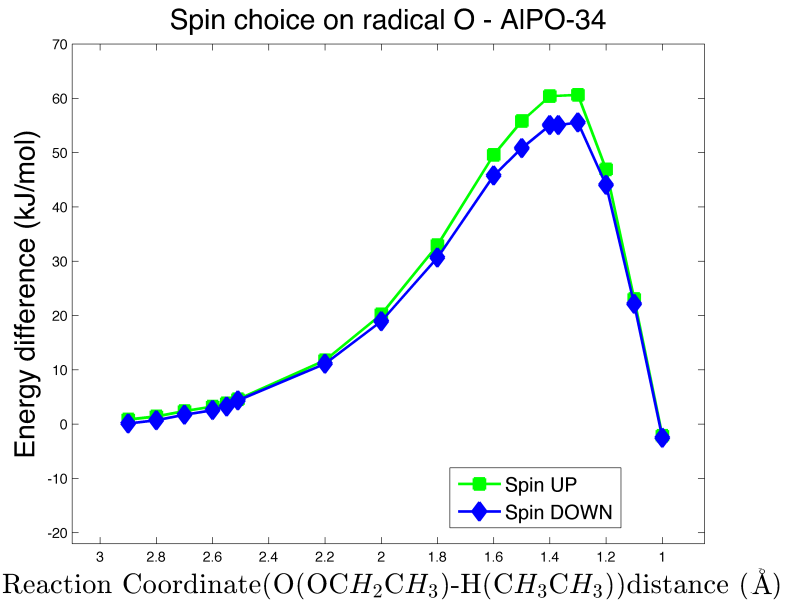

Figure 6.6: Calculated energy profiles for the two different spin directions, up (green line) and down (blue line), of the radical O.

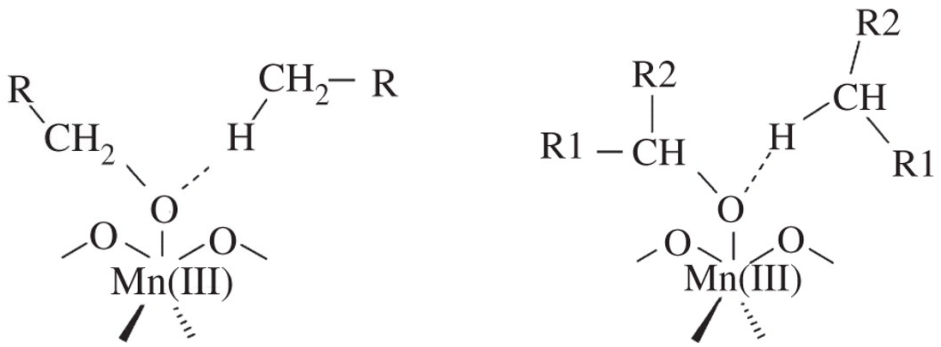

Figure 6.7: Reaction scheme showing the TSs in the propagation step corresponding to selectivity to oxidation at (a) primary and (b) secondary C atoms.

As this step requires the presence of two hydrocarbon molecules, we suggest that for product selectivity to primary C oxidation to arise, the step in which both HC molecules are activated at the primary C atom must have favourable energetics relative to those in which one or both molecules are activated at the secondary C atom.

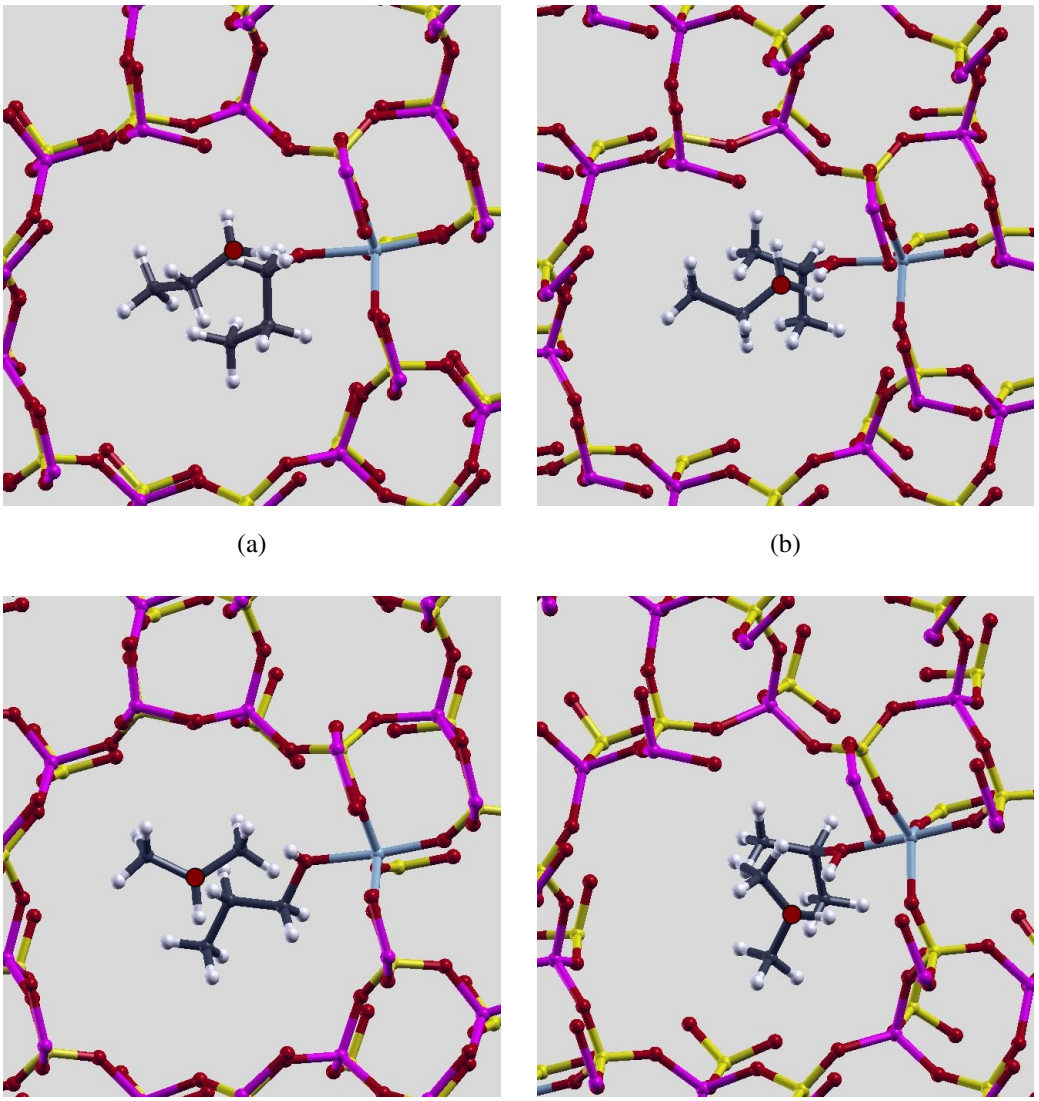

(a) (b)

(c) (d)

Figure 6.8: View of the TS for the propagation step for the four (4) possible combinations of oxidation of propane. A red dot indicates in which position of the propane the oxidation takes place. Mn active site is represented in light blue, P in yellow, Al in pink and O in red.

Thus, we examine the barrier for four (4) possible combinations of primary and secondary carbon atoms, for both MnAlPO-5 and MnAlPO-34 frameworks. Figure 6.8 show the TS structures for these four combinations when MnAlPO-5 is used as framework; (a) an H is transferred from a primary C atom of propane while the alkoxy

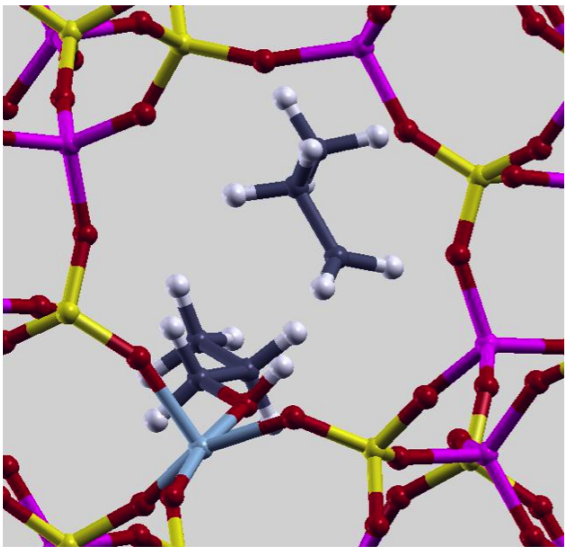

Figure 6.9: Oxidation of propane in small pore apertures of AlPO-34 showing the bulkier TS due to the presence of two hydrocarbon molecules.

	MnAlPO-5		MnAlPO-34	
(kJ/mol)	ΔH	Ea	ΔH	Ea
H abstraction from CH_3CH_3	-17.63	27.34	-2.50	55.0
H-abstraction from primary C atom of $CH_3CH_2CH_3$ - primary alkoxy radical	4.75	63.03	-13.49	42.75
H-abstraction from primary C atom of $CH_3CH_2CH_3$ - secondary alkoxy radical	-9.37	50.08	-7.66	44.79
H-abstraction from secondary C atom of $CH_3CH_2CH_3$ - primary alkoxy radical	26.42	15.71	-38.01	20.93
H-abstraction from secondary C atom of $CH_3CH_2CH_3$ - secondary alkoxy radical	-28.31	28.98	-39.70	28.81

Table 6.2: Summary of the energies (reaction enthalpies ΔH and activation energies Ea in kJ/mol) of the H abstractions from propane for both MnAlPO-5 and MnAlPO-34 frameworks.

radical is activated at the primary C atom, (b) a H is transferred from a primary C atom of propane while the alkoxy radical is activated at the secondary C atom, (c) a H is transferred from a secondary C atom of propane while the alkoxy radical is activated at the primary C atom, and (d) an H is transferred from a secondary C atom of propane while the alkoxy radical is activated at the secondary C atom. Comparison of the structures with figure 6.9 shows that the smaller pore dimensions of MnAlPO-34 (pore aperture of 3.8 Å) impose more stringent constraints on the bulkier TS originating from the activation of the secondary C atoms while the large channels of MnAlPO-5 (pore aperture of 7.3Å) allows for a reactivity on the secondary C atom, typical of the gas-phase propane molecules. Figure 6.10 represents the reaction profiles while table 6.2 summarises the reaction enthalpies and activation barriers for all combinations. Because of the formation of $Mn^{III} \cdots OR$ complex, we could expect more structural constraints.

At first glance, we observe similar trends in TS and reaction barriers for both AlPO-5 and AlPO-34 frameworks. The higher activation energy is when MnAlPO-5 is used and an H atom is transferred from a primary carbon atom and the radical O atom is bonded to a primary C atom as well (energy difference ~13kJ/mol), while with MnAlPO-34 the energy is not affected by the position of the alkoxy radical (energy difference ~0.30 kJ/mol). In general, the reaction is thermodynamically controlled and gives more stable results when the H is transferred from secondary C atom for both structures. The initial alkoxy radical is stabilized by ligation to Mn and whether it is primary or secondary C has little effect; the energy difference is ~13kJ/mol and ~8kJ/mol for AlPO-5 and AlPO-34 respectively and the TS is lower with the activation of primary alkoxy radical. The biggest energy difference between the use of AlPO-5 and AlPO-34 lies when selectivity arises on the primary C atom for both hydrocarbon species involved in the reaction (~18kJ/mol), showing that the smaller AlPO-34 can reduce considerably the activation energy when oxidation takes place on the primary C atom.

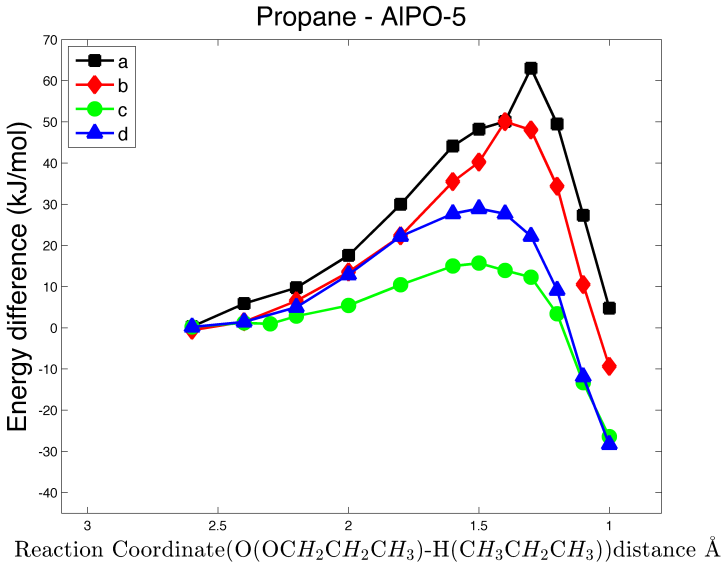

(a)

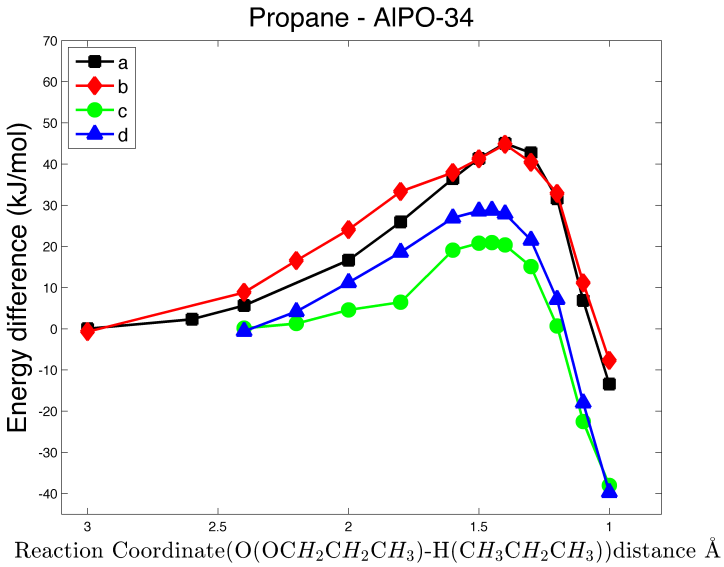

(b)

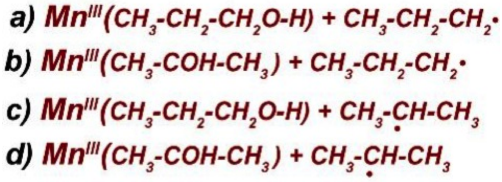

(c)

Figure 6.10: Propagation step with (a) AlPO5 and (b) AlPO-34 framework and propane as substrate; reaction profiles for four (4) possible combinations of primary and secondary carbon atoms, and (c) the relative reactions.

6.2.2 Propane VS Hexane

6.2.2.1 Aerobic oxidation of hexane catalysed by Mn-doped AlPO-34

So far, we have observed that the choice of a framework with smaller pore dimensions than AlPO-5 can actually impose some steric constraints on the bulkier TS arising from the activation of secondary C atom of propane. However, both preactivaion and propagation step reactions are again dominated by thermodynamic factors as the calculated activation energies are lower when the reaction takes place on the secondary C atom.

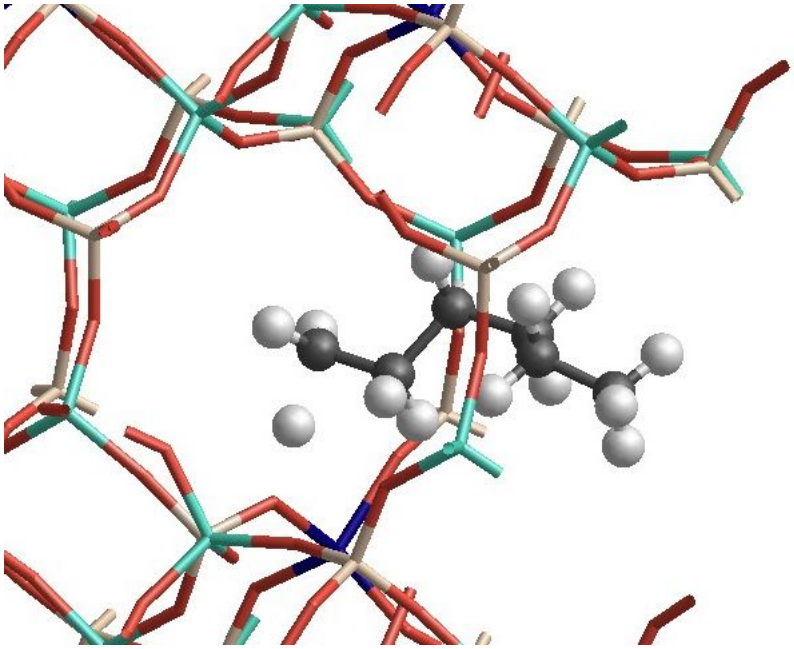

Figure 6.11: Structural representation of the H transfer from primary C atom of hexane in the double unit cell of MnAlPO-34.

In this section, we chose AlPO-34 framework and we change our substrate from propane to hexane in order to examine how reaction enthalpies and activation barriers are changing for the preactivation step when a smaller-pore molecular sieve is used. Although Mn image sites do not interact significantly with each other, there could be a small interaction between the reactants in contiguous image cells because the CHA unit cell dimensions are not large enough and most importantly, linear hexane is con-

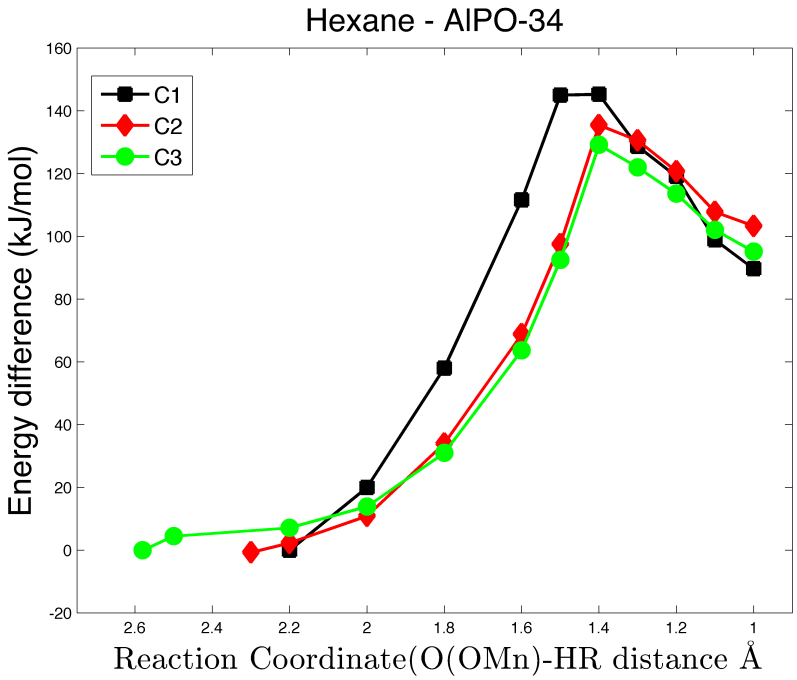

Figure 6.12: Energy profiles for the H transfer from hexane from primary C1 and secondary C2, C3 carbon atoms in MnAlPO-34.

siderably longer than ethane and propane. For this reason, we doubled our unit cell to avoid any undesirable interaction.

Table 6.3 summarises the reaction enthalpies and activation barriers for all three combinations of different structures: H transfer from a primary carbon atom C1 atom and from a secondary carbon atom from position C2 or C3. For comparison, we have also included in the table the energetics from ethane and propane examined before. Figure 6.12 presents the reaction profiles for the hexane oxidation for the three combinations. A very important observation is that the activation of the primary C1 gives the lowest reaction enthalpy (~ 89kJ/mol) compared to the secondary C2 (~103kJ/mol) and C3 (~ 95kJ/mol) showing that AlPO-34 can impose some selectivity constraints. However, the activation of C1 gives the highest TS energy while C3 the lowest (energy difference ~ 16kJ/mol) confirming that the hexane oxidation is thermodynamically controlled. Figure 6.11 shows how the long chain of hexane approaches the active

site inside the AlPO-34 framework. In the confined space provided by the small-pore AlPO-34, the presence of two hexane molecules in the propagation step may modify sufficiently the steric requirements of the C-H bond cleavage. Functionalization arises on the propagation step, but it is too complicated to examine this step with two hexane molecules with the available resources.

MnAlPO-34		
(kJ/mol)	ΔH	Ea
H-abstraction from CH_3CH_3	130.28	158.99
H-abstraction from primary C atom of $CH_3CH_2CH_3$	129.58	163.81
H-abstraction from secondary C atom of $CH_3CH_2CH_3$	110.56	153.47
H-abstraction from primary C1 atom of C_6H_{14}	89.64	145.25
H-abstraction from secondary C2 atom of C_6H_{14}	103.27	135.43
H-abstraction from secondary C3 atom of C_6H_{14}	95.10	129.12

Table 6.3: Summary of the energies (reaction enthalpies ΔH and activation energies Ea in kJ/mol) of the H abstraction from a hexane in MnAlPO-34 frameworks.

6.2.3 Impact on energies with the increase on the amount of HF exchange

Taking into account the results from our study in Chapter 4, we have performed a series of calculations with a different functional and in particular, we increased the amount of HF exchange from 20% in B3LYP to 50% in $F_{0.50}$-PBE.

Figure 6.13 shows the reaction profiles when ethane is used as substrate and AlPO-34 as framework. We observe similar trends as in AlPO-5 framework. For the

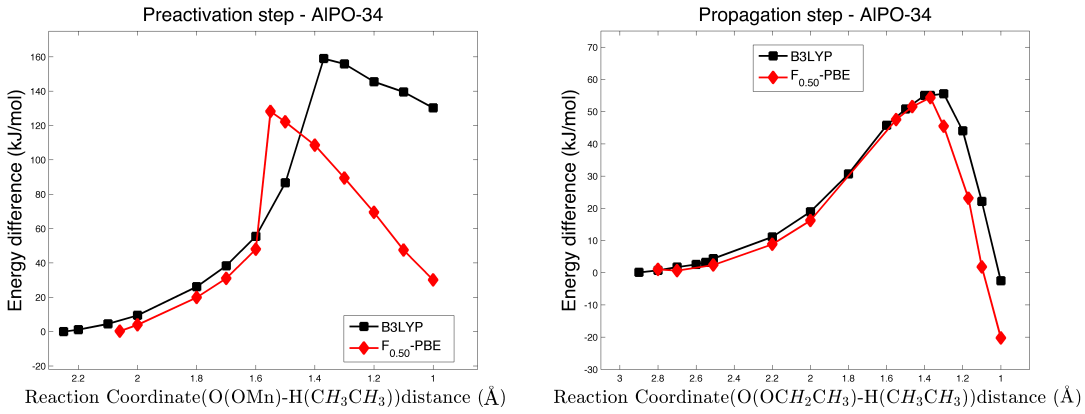

(a) (b)

Figure 6.13: Energy profiles with the use of B3LYP and $F_{0.50}$-PBE functionals for (a) the preactivation step and (b) the propagation step. Ethane is used as substrate and AlPO-34 as framework.

preactivation step, the TS gets lower in energy with the increase of HF exchange and also closer to the reactants. Particularly, for the B3LYP functional, the energy diagram shows for this process an activation energy of 160kJ/mol and for $F_{0.50}$-PBE of 135kJ/mol which means a difference of 25kJ/mol, while in AlPO-5 the difference between the TS of the two functional was 20kJ/mol. This indicates again that the choice of functional has a strong influence on the energy when the oxidation state of Mn changes from 3+ to 2+ and the increase of HF exchange progressively stabilises the high spin d^5 electronic configuration of Mn^{2+} relative to Mn^{3+}. For the propagation step, again we observe slightly different behaviour. Although the reaction enthalpy becomes lower with the increase of HF exchange, the activation energy does not change significantly (only $\sim$ 1kJ/mol).

In a further investigation of increasing the amount of HF exchange, we have changed ethane to propane and have examined the energetics for the preactivation step in AlPO-5. In this case, we need to examine the barrier for both combinations where a H atom is transferred from the primary carbon of the propane and from the secondary carbon (figure 6.2). When the reaction takes place on the primary carbon

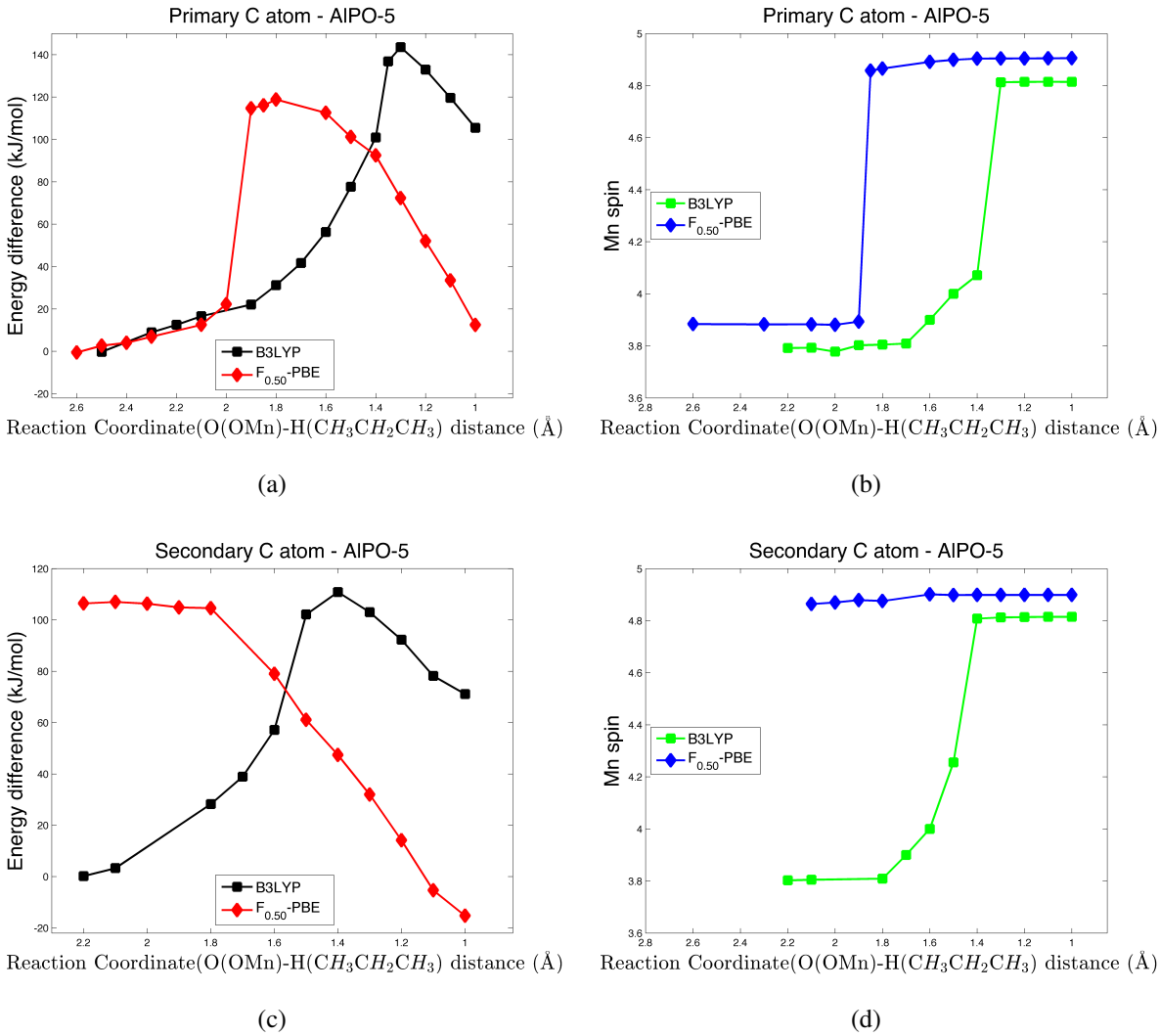

Figure 6.14: Energy diagram for the activation of propane by MnAlPO-5. (a) Activation of terminal C atom and (b) Mn spin density, (c) activation of secondary C atom and (c) Mn spin density when using B3LYP and $F_{0.50}$-PBE hybrid exchange functionals.

atom of propane, we observe the same trend as previously where an ethyl radical was formed. As the amount of HF exchange increases to 50% the TS state becomes lower in energy and closer to the reactants while for B3LYP is higher in energy and closer to the products (figure 6.14). The TS when we use B3LYP functional appears at 142 kJ/mol, while for $F_{0.50}$-PBE is at 120 kJ/mol. There is an energy difference between these TSs of 20kJ/mol. When the reaction takes place on the secondary carbon atom

of propane, substantial differences appear. As expected, for the B3LYP functional the reaction enthalpy as well as the TS are lower in energy when the secondary carbon atom is activated (figure 6.14). However for the $F_{0.50}$-PBE functional the energy profile and spin evolution of this process represented in figure 6.14, show that Mn does change its oxidation state and thus, the reaction does not follow the radical mechanism but probably a complete transfer of electrons takes place leading to the formation of an ion.

6.3 Summary and Conclusions

By making reference to the catalytic cycle of the aerobic oxidation of ethane catalyzed by MnAlPO-5 analysed in Chapter 2, in this Chapter we extended the study of Chapter 4 in two directions: the examination of oxidation of primary and secondary carbon atoms of linear hydrocarbons and the comparison of the oxidation of hydrocarbons in different Mn-doped AlPO frameworks. We have chosen two elementary reaction steps where selectivity issues arise; the first is the abstraction of H from ethane in the preactivation phase, and the second step comes from the propagation phase of the catalytic cycle, where two hydrocarbon molecules are involved and the bulkier TS in secondary C oxidation can be blocked in small-pore microporous AlPOs.

Although the use of ethane as the hydrocarbon substrate does not allow us to discriminate the reactivity of primary and secondary carbon atoms to oxidation, it helps us though to show how a small pore aperture like this of MnAlPO-34 can impose some steric constraints and give a higher activation energy than the larger MnAlPO-5. The choice of propane enables us to compare the reactivity of primary and secondary C atoms, which is a real issue in practical hydrocarbon oxidation reactions. With the use of MnAlPO-5 framework, our results show that when the H-abstraction reaction takes place on the secondary carbon atom of propane, it requires lower activation barriers than on the primary C atoms. This result is consistent with the gas phase stability of primary and secondary C-based radicals. It indicates that the pore size on AlPO- 5 is

too large to impose structural constraints on the transition states and products formed, hence the propane oxidation is thermodynamically controlled. Imposition of structural constraints to control the selectivity of the catalytic reaction requires AlPO frameworks whose pore dimension is close to the size of the organic substrate, that is functionalised in the reaction cycle. In order to observe if the frameworks impose any constraints, the preactivation step was repeated for the AlPO-34 framework. Although the oxidation of secondary carbon is energetically favoured, the activation energy is very close to the one when oxidation takes place on the primary C atom confirming the stringent effect of the smaller pore sized framework.

Continuing with the propagation step which involves two substrate molecules both contributing to the steric constraints, we show how the oxidation of propane can be affected when the space neighbouring the active site is already occupied by an alkoxy radical. For this step we needed to examine four (4) possible combinations of primary and secondary carbon atoms, for both MnAlPO-5 and MnAlPO-34 frameworks. With MnAlPO-5, when the H-abstraction takes place on the secondary carbon atom of propane, it requires lower activation barriers than on the primary C atoms, indicating again that the pore size of AlPO-5 is too large to impose structural constraints on the transition states and products formed. MnAlPO-34 does not alter the typical reactivity of the gas-phase propane; however the reaction barriers for both primary and secondary C oxidation are very close ($\sim$ 24kJ/mol difference). The initial alkoxy radical is stabilized by ligation to Mn and whether it is primary or secondary C has little effect, especially with MnAlPO-34.

In the following part of this chapter, we changed our hydrocarbon from propane to hexane where we observe similar trends, although the reaction enthalpy is lower when the oxidation takes place on the primary carbon atom C1.

In the last part of this chapter, we performed a series of calculations with different amount of HF exchange in order to compare the results deriving from different AlPO frameworks. The trend the reaction profiles follow in AlPO-34 is similar to AlPO-5.

The self-interaction error is again present giving a TS lower in energy and closer to the reactants as the amount of HF exchange increases. However, in the propagation step both B3LYP and $F_{0.50}$-PBE functionals show similar reaction barriers.

Our computational study has given a useful insight in order to enable a future rational design of new catalysts in which the atomic-level features of the TS are suitably constrained to direct selectivity toward oxidation of primary and secondary C atoms.

Chapter 7

Conclusion

7.1 Summary of thesis contributions

We have demonstrated that computer modelling has become increasingly powerful in materials science in a qualitative and quantitative way, where it effectively complements the experimental investigations, investigates atomic-scale features that could be difficult to obtain only from experiment, and also has a predictive role in the improvement of materials, allowing rational design of heterogeneous catalysts. This thesis has focused on simulating catalytic redox reactions, aiming to provide insight for the design of new catalysts and the improvement of existing ones.

TM-doped microporous aluminophosphates have enormous catalytic potential in redox processes. They catalyse a variety of synthetically useful oxidative transformations with environmentally and economically attractive oxidants, such as molecular oxygen. Their pore sizes endow them with special capabilities for heterogeneous catalysis. In particular, aluminophosphate catalysts are of great importance as their activation with different dopant atoms such as Co, Mn and Fe can give a series of doped materials with catalytic properties. The selective oxidation of saturated hydrocarbons in the terminal position represents a major challenge in contemporary catalytic chemistry as it leads to alcohols, ketones, aldehydes and carboxylic acids which are desirable feedstocks for the chemical and pharmaceutical industries.

In the mechanism of the aerobic oxidation of ethane catalysed by Mn-doped AlPO-5 we did not know the accuracy of the reaction barriers and reaction enthalpies and the level of confidence for these results. Starting from the results of Gómez Hortigüela *et al.* [40] we extended these studies. In this Thesis, three sets of complementary results were presented; **(1)** the comparison of different functionals (a selection of GGA and hybrid functionals with different amounts of exact exchange between 0 and 50%) **(2)** the examination of the oxidation of primary and secondary carbon atoms of linear alkanes (propane and hexane), and **(3)** the comparison of different sized Mn-doped AlPO frameworks (MnAlPO-5 and MnAlPO-34) in imposing steric constraints. Two representative steps of the catalytic cycle discussed in [40] were studied: the abstraction of H from the hydrocarbon in the preactivation phase, which involves a reduction of the Mn^{III} site to Mn^{II} and the formation of a carbon-based radical, and one step of the propagation mechanism where Mn does not change oxidation state, while the radical-like nature of this RO· ligand allows H-transfer from a new hydrocarbon molecule in order to form an alcohol molecule (ROH).

We have shown that calculated reaction and activation energies vary on changing the exchange and correlation functionals used in the DFT calculations. The rationale is that redox processes change the electronic configuration and number of *d*-electrons of the transition metal ions, and hence are expected to be affected by the self-interaction error (SIE) of local DFT functionals. The orbital-dependent solution obtained by inclusion of exact exchange in hybrid-exchange functionals corrects for the SIE. We examined the performance of a selection of GGA and hybrid exchange functionals with different amounts of exact exchange between 0 and 50%. Indeed results confirm that the self-interaction contribution to calculated reaction and activation energies is very important. In the preactivation step, it is observed that the activation barrier becomes lower in energy with the increase of Hartree-Fock exchange in the functional. Local DFT functionals are unable to describe in a quantitative way the reduction of Mn from 3+ to 2+ oxidation state, which occurs through the localisation of an extra electron on

Mn and is opposed by a spurious SIE. In the propagation step, the unpaired electron of the organic radical is delocalised between alcoxy and alkyl radical in the transition state, which is stabilised by the self-interaction error. As a consequence, the calculated activation barrier increases upon increasing the fraction of Hartree-Fock exchange. Thus, DFT results of this and similar redox reactions need to be carefully calibrated.

As there are no experimental investigations estimating the Mn^{III}/Mn^{II} reduction potential in the AlPO matrix, in order to establish confidence in our computational results, the Li intercalation potential of $LiMPO_4$ (M=Mn or Fe) has been computed using the same functionals with different amounts of HF exchange. With the delithiation of $LiMPO_4$, Mn changes its oxidation state from M^{3+} to M^{2+} in a similar way as in the MnAlPO-5 system. When the amount of HF exchange is between 20% and 25%, the Li intercalation potential is closest to the experimental value, but the choice of TM plays also important role. For example, the PBE with 40% of HF exchange gives better results for Li intercalation of $LiFePO_4$. These results suggest that similar amounts of HF could be used in modelling other processes involving redox reactions or TM ions, including catalysis.

In Chapter 6 of this thesis, we considered the main advantages of TM-doped AlPOs which are associated with the molecular dimensions of their pore system, allowing for shape-selectivity as the reaction taking place can be affected by the constrained environment. Thus, we analysed selectivity issues related to the chosen preactivation and propagation elementary reaction steps. We compared the reactivity of primary and secondary C atoms in linear alkanes, such as propane and hexane, with the aim of understanding if selectivity in terminal methyl groups arises when steric constraints are imposed by the catalyst, which is an open question in practical hydrocarbon oxidation reactions. We showed that when the H-abstraction reaction takes place on the secondary carbon atom of propane, it requires lower activation barriers than on the primary C atoms. The pore size of AlPO-5 is too large to impose structural constraints on the

transition states and products formed, hence propane oxidation is thermodynamically favoured on the secondary C atom.

In order to observe if the choice of framework can impose any constraints, the calculations were repeated for the small-pore AlPO-34 framework. Similar trends were observed in TS and reaction barriers as in AlPO-5. However, in the propagation step where mechanism requires two hydrocarbon molecules and hence steric constraints are more important, the energy difference between activation energies of primary and secondary C atoms are much closer in the small-pore AlPO-34 than in AlPO-5, indicative of some steric constraint. We therefore changed our hydrocarbon substrate from propane to hexane to further investigate the reactivity of alkanes. Although hexane is a longer molecule, AlPO-34 does not impose steric constraints to an extent that it could reverse the relative reactivity of the different carbon atoms product away from that predicted by the basic thermodynamics of the hydrocarbon oxidation, although we note that oxidation on the primary C1 atom has the lowest reaction enthalpy.

7.2 Future work

The interest in redox processes in catalytic chemistry is growing rapidly. Based on the work reported in this thesis, we now discuss open issues and possible directions for extending this research. Future targets of research can be related to the advantageous properties of TM-doped aluminophosphate catalysts. These could be explored by capitalising on the continuing exponential growth of computational power.

The redox potential of the Mn^{3+}/Mn^{2+}, Fe^{3+}/Fe^{2+} and Co^{3+}/Co^{2+} is substantially different. However, the way in which this could affect the reaction mechanisms is not yet understood. Developing a full explanation of the performance of AlPO catalysts in oxidation reactions from the calculated mechanistic and energetic information would be of particular interest. Since a comparative computational study of the aerobic oxidation of a hydrocarbon catalysed by Mn- and Fe-doped AlPOs have been already examined [132] and have shown distinctive features for each transition metal depending on its

electronic configuration, the performance of Co dopant could be also investigated in order to provide a screening of different dopants.

The work reported in Chapter 4 has clear potential for future calculations into the effect of different dopants. As we showed in Chapter 5, PBE functional with 40% of HF exchange predicts very well the Li intercalation potential on $LiFePO_4$ while for $LiMnPO_4$ this is the case for an amount between 20-25%. Thus, a benchmark of functionals with different amounts of HF exchange could also be produced for Fe-doped AlPO-5 in order to investigate to what extend the change of electronic configuration from d^5 to d^6 in the preactivation phase, can be affected by the SIE compared to Mn-doped AlPO-5.

Another direction could be to study further oxidation reactions [147] from the mechanism described on reference [40]. Of particular interest would be the transformation of primary oxidation products, like alcohols, into aldehydes first and then carboxylic acids with MnAlPO-34 as the framework.

A different extension would consist of the investigation of ammonia oxidation. In the reaction to produce alcohol, the oxidising agent is NH_2OH produced *in situ* with MeAlPO catalysts from NH_3 and O_2 [85] . While the stoichiometry suggests this reaction proceeds with a mechanism analogous to the alkane oxidation, the atomic level changes introduced by replacing C with N are not known. Ammonia is a suitably simple substrate from a computational perspective, hence suggesting that computational work may provide valuable insight.

Finally, creating bimetallic multifunctional active sites in microporous solids is a relatively new area of research with industrial importance [148]. The design of bimetallic multifunctional active sites involves the isomorphous replacement of a few atom percent of the aluminophosphate framework, Al(III) and P(V) cations with tetrahedrally-coordinated TM ions. Taking into consideration the work in Chapter 6, the selective oxidation of hexane could be investigated for bimetallic AlPO-34 and compare the results with those deriving from the monometallic AlPO-34. Since the titanium-based microp-

orous solids have been proved particularly effective in epoxidation reactions [149], the simultaneous incorporation of two metals could reveal enhancements in the observed synergy in catalytic reactions.

Overall, there are many avenues for future computational studies, for which the work reported in this thesis will provide a good basis.

Bibliography

[1] G. H. Li, H. Azuma, and M. Tohda. $LiMnPO_4$ as the Cathode for Lithium Batteries. *Electrochemical and Solid-State Letters*, 5:A135–A137, 2002.

[2] G. Pistoia. *Lithium Batteries*. Elsevier, 1994.

[3] D. Morgan, A. Van der Ven, and G. Ceder. Li conductivity in Li_xMPO_4 (M= Mn, Fe, Co, Ni) olivine materials. *Electrochemical and Solid-State Letters*, 7:A30–A32, 2004.

[4] F. Zhou, M. Cococcioni, K. Kang, and G. Ceder. The Li intercalation potential of $LiMPO_4$ and $LiMSiO_4$ olivines with M = Fe, Mn, Co, Ni. *Electrochemistry communications*, 6:1144–1148, 2004.

[5] J. M. Osorio-Guillen, B. Holm, R. Ahuja, and B. Johansson. A theoretical study of olivine $LiMPO_4$ cathodes. *Solid State Ionics*, 167:221–227, 2004.

[6] A. Van der Ven, M. K. Aydinol, G. Ceder, G. Kresse, and J. Hafner. First-principles investigation of phase stability in Li_xCoO_2. *Physical Review B*, 58:2975, 1998.

[7] F. Zhou, M. Cococcioni, C. A. Marianetti, D. Morgan, and G. Ceder. First-principles prediction of redox potentials in transition-metal compounds with LDA + U. *Physical Review B*, 70:235121, 2004.

[8] L. Wang, T. Maxisch, and G. Ceder. Oxidation energies of transition metal oxides within the GGA+ U framework. *Physical Review B*, 73:195107, 2006.

[9] M. K. Aydinol, A. F. Kohan, G. Ceder, K. Cho, and J. Joannopoulos. Ab initio study of lithium intercalation in metal oxides and metal dichalcogenides. *Physical Review B*, 56:1354, 1997.

[10] C. J. Cramer and D. G. Truhlar. Density functional theory for transition metals and transition metal chemistry. *Physical Chemistry Chemical Physics*, 11:10757–10816, 2009.

[11] A. Van der Ven and G. Ceder. Lithium Diffusion in Layered Li_xCoO_2. *Electrochemical and Solid-State Letters*, 3:301–304, 2000.

[12] C.R.A. Catlow. *Computer Modelling in Inorganic Crystallograpy*. Academic Press, London, 1997.

[13] I. Saadoune, F. Corà, M. Alfredsson, and C. R. A. Catlow. Computational study of the structural and electronic properties of dopant ions in microporous AlPOs. 2. Redox catalytic activity of trivalent transition metal ions. *The Journal of Physical Chemistry B*, 107:3012–3018, 2006.

[14] F. Corà, G. Sankar, C. R. A. Catlow, and J. M. Thomas. Electronic state and three-dimensional structure of Mn(III) active sites in manganese-containing aluminophosphate molecular sieve catalysts for the oxyfunctionalisation of alkanes. *Chemical Communications*, 20:734–735, 2002.

[15] I.W.C.E. Arends, R. A Sheldon, M. Wallau, and U. Schuchardt. Oxidative Transformations of Organic Compounds Mediated by Redox Molecular Sieves. *Angewandte Chemie International edition*, 36:1144–1163, 1997.

[16] J. M. Thomas, R. Raja, G. Sankar, and R. G. Bell. Molecular-sieve catalysts for the selective oxidation of linear alkanes by molecular oxygen. *Nature*, 398:227–230, 1999.

[17] P Hohenberg and W. Kohn. Inhomogeneous electron gas. *Physical Review B*, 136:864–871, 1964.

[18] W. Kohn and L. Sham. Self-Consistent Equations Including Exchange and Correlation Effects. *Physical Review A*, 140:1133–1138, 1965.

[19] J. P. Perdew, K. Burke, and M. Ernzerhof. Generalized Gradient Approximation Made Simple. *Physical Review Letters*, 77:3865–3868, 1996.

[20] A. D. Becke. Density-functional exchange-energy approximation with correct asymptotic behavior. *Physical Review A*, 38:3098–3100, 1988.

[21] C. Lee, W. Yang, and R. G. Parr. Development of the Colle-Salvetti correlation-energy formula into a functional of the electron density. *Physical Review B*, 37:785–789, 1988.

[22] D. D. Davis. *Ullmann's Encyclopedia of Industrial Chemistry*. VCH, 1985.

[23] T. Tatsumi, M. Nakamura, S. Negishi, and H. Tominaga. Shape-selective oxidation of alkanes with H_2O_2 catalysed by titanosilicate. *J. Chem. Soc., Chem. Commun.*, pages 476–477, 1990.

[24] J. M. Thomas, R. Raja, G. Sankar, and R. G. Bell. Molecular sieve catalysts for the regioselective and shape-selective oxyfunctionalization of alkanes in air. *Acc. Chem. Res.*, 34:191–200, 2001.

[25] S. T. Wilson, B. M. Lok, and E. M. Flanigen. Crystalline metallophosphate compositions, 1982. US patent 4310440.

[26] http://www.iza-structure.org/databases/.

[27] J. M. Thomas. Design, synthesis, and in situ characterization of new solid catalysts. *Angewandte Chemie International edition*, 38:3589–3628, 1999.

[28] R. Raja and J. M. Thomas. A manganese-containing molecular sieve catalyst designed for the terminal oxidation of dodecane in air. *Chemical Communications*, pages 1841–1842, 1998.

[29] R. Raja and J. M. Thomas. Catalyst design strategies for controlling reactions in microporous and mesoporous molecular-sieves. *Journal of Molecular Catalysis A-Chemical*, 181:3–14, 2002.

[30] B. Modén, L. Oliviero, J. Dakka, J. G. Santiesteban, and E. Iglesia. Structural and functional characterisation of redox Mn and Co site in AlPO materials and their role in alkane oxidation catalysis. *Journal of Physical Chemistry B*, 108:5552–5563, 2004.

[31] B. Modén, B. Z. Zhan, J. Dakka, J. G. Santiesteban, and E. Iglesia. Reactant selectivity and regiospecificity in the catalytic oxidation of alkanes on metal-substituted aluminophosphates. *The Journal of Physical Chemistry C*, 111:1402–1411, 2007.

[32] R. Raja, G. Sankar, and J. M. Thomas. Designing a molecular sieve catalyst fir the aerial oxidation of n-hexane to adipic acid. *Angewandte Chemie International edition*, 39:2313–2316, 2000.

[33] R. Raja, G. Sankar, and J. M. Thomas. New catalysts for the aerobic selective oxidation of hydrocarbons: Mn(III)- and Co(III)-containing molecular sieves for the epoxidation of alkenes. *Chemical Communications*, pages 829–830, 1999.

[34] R. Raja, G. Sankar, and J. M. Thomas. Powerful redox molecular sieve catalysts for the selective oxidation of cyclohexane in air. *Journal American Chemical Society*, 121:11926–11927, 1999.

[35] B. Modén, B. Z. Zhan, J. Dakka, J. G. Santiesteban, and E. Iglesia. Kinetics and mechanism of cyclohexane oxidation on MnAPO-5 catalysts. *Journal of Catalysis*, 239:390–401, 2006.

[36] L. Zhou, J. Xu, C. Chen, F. Wang, and X. Li. Synthesis of Fe, Co and Mn substituted AlPO-5 molecular sieves and their catalytic activities in the selective oxidation of cyclohexane . *Journal of Porous Materials*, 15:7–12, 2008.

[37] R. Raja, J. M. Thomas, and G. Sankar. Baeyer-Villiger oxidations with a difference: Molecular sieve redox catalysts for the low temperature conversion of ketons to lactones. *Chemical Communications*, 30:525–526, 1999.

[38] M. Hartmann and S. Ernst. Selective Oxidations of Linear Alkanes with Molecular Oxygen on Molecular Sieve Catalysts-A Breakthrough? *Angewandte Chemie International edition*, 39:888–890, 2000.

[39] L. Gómez Hortigüela, F. Corà, and C. R. A. Catlow. Aerobic oxidation of hydrocarbons catalyzed by Mn-doped nanoporous aluminophosphates(I): Preactivation of the Mn sites. *ACS Catalysis*, 1:18–28, 2011.

[40] L. Gómez Hortigüela, F. Corà, G. Sankar, C. M. Zicovich-Wilson, and C. R. A. Catlow. Catalytic Reaction Mechanism of Mn-Doped Nanoporous Aluminophosphates for the Aerobic Oxidation of Hydrocarbons. *CHEMISTRY-A-EUROPEAN JOURNAL*, 16:13638–13645, 2010.

[41] L. Gómez Hortigüela, F. Corà, and C. R. A. Catlow. Aerobic oxidation of hydrocarbons catalyzed by Mn-doped nanoporous aluminophosphates(II): Hydroperoxide decomposition. *ACS Catalysis*, 1:945–955, 2011.

[42] L. Gómez Hortigüela, F. Corà, and C. R. A. Catlow. Aerobic oxidation of hydrocarbons catalyzed by Mn-doped nanoporous aluminophosphates(III): Propagation mechanism. *ACS Catalysis*, 1:1487–1497, 2011.

[43] L. Gómez Hortigüela, F. Corà, and C. R. A. Catlow. Aerobic oxidation of hydrocarbons catalyzed by Mn-doped nanoporous aluminophosphates(IV): Regeneration mechanism. *ACS Catalysis*, 1:1475–1486, 2011.

[44] M. S. Islam and P. R. Slater. Solid-state materials for clean energy: insights from atomic-scale modeling. *MRS bulletin*, 25:935, 2009.

[45] N. Choi, Z. Chen, S. A. Freunberger, X. Ji, Y. Sun, K. Amine, G. Yushin, L. F. Nazar, J. Cho, and P. G. Bruce. Challenges Facing Lithium Batteries and

Electrical Double-Layer Capacitors. *Angewandte Chemie International Edition*, 51:9994–10024, 2012.

[46] J. B. Goodenough and Y. Kim. Challenges for rechargeable Li batteries. *Chemistry of Materials*, 22:587–603, 2009.

[47] K. Amine, H. Yasuda, and M. Yamachi. Olivine $LiCoPO_4$ as 4.8 V electrode material for lithium batteries. *Electrochemical and Solid-State Letters*, 3:178–179, 2000.

[48] A. Yamada, S. C. Chung, and K. Hinokuma. Optimized $LiFePO_4$ for lithium battery cathodes. *Journal of the Electrochemical Society*, 148:A224–A229, 2001.

[49] A. Yamada, M. Hosoya, S. C. Chung, Y. Kudo, K. Hinokuma, K. Y. Liu, and Y. Nishi. Olivine-type cathodes: achievements and problems. *Journal of Power Sources*, 119:232–238, 2003.

[50] J. Wolfenstine and J. Allen. Ni^{3+}/Ni^{2+} redox potential in $LiNiPO_4$. *Journal of power sources*, 142:389–390, 2005.

[51] A. K. Padhi, K. S. Nanjundaswamy, and J. B. Goodenough. Phospho-olivines as positive-electrode materials for rechargeable lithium batteries. *Journal of the Electrochemical Society*, 144:1188–1194, 1997.

[52] S. Y. Chung, J. T. Bloking, and Y. M. Chiang. Electronically conductive phospho-olivines as lithium storage electrodes. *Nature materials*, 1:123–128, 2002.

[53] H. van Bekkum, E. M. Flanigen, P. A. Jacobs, and J. C. Jansen. *Introduction to zeolite science and practice*. Elsevier, Amsterdam, 2001.

[54] J. M. Thomas. Design, synthesis, and in situ characterization of new solid catalysts. *Angewandte Chemie International Edition*, 38:3588–3628, 1999.

[55] C. S. Cundy and P. A. Cox. The hydrothermal synthesis of zeolites: history and development from the earliest days to the present time. *Chemical Reviews*, 103:663–702, 2003.

[56] R. E. Morris. Ionothermal synthesis-ionic liquids as functional solvents in the preparation of crystalline materials. *Chemical Communications*, pages 2990–2998, 2009.

[57] L. Gómez Hortigüela, F. Corà, C. R. A. Catlow, J. Perez-Pariente, and T. Blasco. Structure-directing role of molecules containg bemzyl rings in the synthesis of a large-pore aluminophosphate molecular sieve: An experimental and computational study. *J. Phys. Chem. C*, 109:21539–21548, 2005.

[58] E. R. Parnham and R. E. Morris. Ionothermal synthesis of zeolites, metal–organic frameworks, and inorganic-organic hybrids. *Accounts of chemical research*, 40:1005–1013, 2007.

[59] R. E. Morris and S. J. Weigel. The synthesis of molecular sieves from non-aqueous solvents. *Chem. Soc. Rev.*, 26:309–317, 1997.

[60] E. R. Cooper, C. D. Andrews, P. S. Wheatley, P. B. Webb, P. Wormald, and R. E. Morris. Ionic liquids and eutectic mixtures as solvent and template in synthesis of zeolite analogues. *Nature*, 430:1012–1016, 2004.

[61] M. Hartmann and L. Kevan. Transition-metal ions in aluminophosphate and silicoaluminophosphate molecular sieves: location, interaction with adsorbates and catalytic properties. *Chemical reviews*, 99:635–664, 1999.

[62] G. Sankar, R. Raja, and J. M. Thomas. Redox solid catalysts for the selective oxidation of cyclohexane in air. *Catalysis letters*, 55:15–23, 1998.

[63] J. M. Thomas, R. Raja, G. Sankar, and R. G. Bell. Molecular-sieve catalysts for the selective oxidation of linear alkanes by molecular oxygen. *Nature*, 398:227–230, 1999.

[64] F. Corà, M. Alfredsson, C. M. Barker, R.G. Bell, M.D. Foster, I. Saadoune, A. Simperler, and C. R. A. Catlow. Modelling the framework stability and catalytic activity of pure and transition metal-doped zeotypes . *Journal of Solid State Chemistry*, 176:496–529, 2003.

[65] L. Gómez Hortigüela, R. Garcia, F. Lopez-Arbeloa, F. Corà, and J. Perez-Pariente. Structure Directing effect of (1S,2S)-2-Hydroxymethyl-1-benzyl-1-methylpyrrolidinium in the Synthesis of AlPO-5. *J. Phys. Chem. C*, 114:8320–8327, 2010.

[66] M. Stöcker. Methanol-to-hydrocarbons: catalytic materials and their behavior. *Microporous and Mesoporous Materials*, 29:3–48, 1999.

[67] S. Wilson and P. Barger. The characteristics of SAPO-34 which influence the conversion of methanol to light olefins. *Microporous and Mesoporous Materials*, 29:117–126, 1999.

[68] W. O. Haag, R. M. Lago, and P. B. Weisz. The active site of acidic aluminosilicate catalysts. *Nature*, 309:589–591, 1984.

[69] S. Hoéevar, J. Batista, and V. Kauéié. Acidity and Catalytic Activity of MeAPSO-44 (Me= Co, Mn, Cr, Zn, Mg), SAPO-44, $AlPO_4$-5, and $AlPO_4$-14 Molecular Sieves in Methanol Dehydration. *Journal of Catalysis*, 139:351–361, 1993.

[70] C. de las Pozas, R. Lopez-Cordero, J. A. Gonzalez-Morales, N. Travieso, and R. Roque-Malherbe. Effect of pore diameter and acid strength in ethanol dehydration on molecular sieves. *Journal of molecular catalysis*, 83:145–156, 1993.

[71] H. Nur and H. Hamdah. The ionic size of metal atoms in correlation with acidity by the conversion of cyclohexanol over MeAPO-5. *Materials Research Bulletin*, 36:315–322, 2001.

[72] P. Ugliengo, B. Civalleri, C. M. Zicovich-Wilson, and R. Dovesi. H-Chabazite with variable Si/Al ratio: stability and OH vibrational frequency computed in a periodic LCAO B3LYP approach. *Chemical Physics Letters*, 318:247–255, 2000.

[73] M. Elanany, M. Koyama, M. Kubo, P. Selvam, and A. Miyamoto. Periodic density functional investigation of Brønsted acidity in isomorphously substituted chabazite and AlPO-34 molecular sieves. *Microporous and Mesoporous Materials*, 71:51–56, 2004.

[74] H. G. Karge and V. Dondur. Investigation of the distribution of acidity in zeolites by temperature-programmed desorption of probe molecules. I. Dealuminated mordenites. *Journal of Physical Chemistry*, 94:765–772, 1990.

[75] H. G. Karge, V. Dondur, and J. Weitkamp. Investigation of the distribution of acidity strength in zeolites by temperature-programmed desorption of probe molecules. 2. Dealuminated Y-type zeolites. *The Journal of Physical Chemistry*, 95:283–288, 1991.

[76] G. Lischke, B. Parlitz, U. Lohse, E. Schreier, and R. Fricke. Acidity and catalytic properties of MeAPO-5 molecular sieves. *Applied Catalysis A: General*, 166:351–361, 1998.

[77] F. Corà, I. Saadoune, and C. R. A. Catlow. Lewis Acidity in Transition-Metal-Doped Microporous Aluminophosphates. *Angewandte Chemie International Edition*, 41:4677–4680, 2002.

[78] F. J. Luna, S. E. Ukawa, M. Wallau, and U. Schuchardt. Cyclohexane oxidation using transition metal-containing aluminophosphates (MAPO-VFI). *Journal of Molecular Catalysis A: Chemical*, 117:405–411, 1997.

[79] I. Bertini, H. B. Gray, S. J. Lippard, and J. S. Valentine. *Bioinorganic chemistry*. University Science Books, 1994.

[80] N. Herron and C. A. Tolman. A highly selective zeolite catalyst for hydrocarbon oxidation. A completely inorganic mimic of the alkane ω-hydroxylases. *Journal of the American Chemical Society*, 109:2837–2839, 1987.

[81] V. L. Pecoraro. *Manganese redox enzymes*. VCH, 1992.

[82] J. M. Thomas, R. Raja, and D. W. Lewis. Single-Site Heterogeneous Catalysts. *Angewandte Chemie International Edition*, 44:6456–6482, 2005.

[83] T. Yamada, T. Takai, O. Rhode, and T. Mukaiyama. Highly efficient method for epoxidation of olefins with molecular oxygen and aldehydes catalyzed by nickel (II) complexes. *Chemistry Letters*, pages 1–4, 1991.

[84] C. M. Freeman, C. R. A. Catlow, J. M. Thomas, and S. Brode. Computing the location and energetics of organic molecules in microporous adsorbents and catalysts: a hybrid approach applied to isometric butenes in a model zeolite. *Chemical physics letters*, 186:137–142, 1991.

[85] J. M. Thomas and R. Raja. Design of a green one-step catalytic production of ε-caprolactam (precursor of nylon-6). *Proceedings of the National Academy of Sciences of the United States of America*, 102:13732–13736, 2005.

[86] W. M. Meier and D. H. Olson. *Atlas of Zeolite Structure Types*. third edition, 1992.

[87] C. J. Cramer. *Essentials of Computational Chemistry - Theories and Models*. WILEY, second edition, 2004.

[88] C. R. A. Catlow, R. Bell, F. Corà, and B. Slater. *Introduction to Zeolite Molecular Sieves*, volume 168, chapter Molecular Modelling in Zeolite Science, pages 659–700. Elsevier, 2007.

[89] J. Cejka, H. Van Bekkum, A. Corma, and F. Schueth. *Introduction to Zeolite Molecular Sieves*, volume 168. Elsevier, 2007.

[90] A. Simperler, M. D. Foster, R. G. Bell, and J. Klinowski. Hypothetical uninodal zeolite structures: comparison of AlPO4 and SiO2 compositions using computer simulation. *The Journal of Physical Chemistry B*, 108:869–879, 2004.

[91] F. Jensen. Introduction to computational chemistry. *New York*, pages 127–131, 1999.

[92] R. Parr and W. Yang. *Density Functional Theory of Atoms and Molecules*. New York, 1989.

[93] P. Atkins and R. Friedman. *Molecular Quantum Mechanics*. OXFORD University Press, fourth edition, 2005.

[94] A. J. Cohen, P. Mori-Sánchez, and W. Yang. Challenges for density functional theory. *Chemical reviews*, 112:289–320, 2012.

[95] N. Kaltsoyannis. Recent developments in computational actinide chemistry. *Chemical Society Reviews*, 32:9–16, 2003.

[96] R. Grau-Crespo, F. Corà, A. A. Sokol, N. H. de Leeuw, and C. R. A. Catlow. Electronic structure and magnetic coupling in $FeSbO_4$: a DFT study using hybrid functionals and GGA+U Methods. *Physical Review B*, 73:035116, 2006.

[97] W. Koch and M. C. Holthausen. *A chemist's guide to density functional theory*, volume 2. Wiley-Vch Weinheim, 2001.

[98] P. A. M. Dirac. Note on exchange phenomena in the Thomas atom. *Proceedings of the Cambridge Philosophical Society*, 26:376–385, 1930.

[99] S. H. Vosko, L. Wilk, and M. Nusair. Accurate spin-dependent electron liquid correlation energies for local spin-density calculations - A critical analysis. *Canadian Journal of Physics*, 58:1200–1211, 1980.

[100] F. Bloch. Über die quantenmechanik der elektronen in kristallgittern. *Zeitschrift für physik*, 52:555–600, 1929.

[101] R. Jones and O. Gunnarsson. Density-functional formalism: Sources of error in local-density approximations. *Physical review letters*, 55:107, 1985.

[102] J. P. Perdew and A. Zunger. Self-interaction correction to density-functional approximations for many-electron systems. *Physical Review B*, 23:5048–5079, 1981.

[103] A. Ruzsinszky, J. P. Perdew, G. I. Csonka, O. A. Vydrov, and G. E. Scuseria. Density functionals that are one-and two-are not always many-electron self-interaction-free, as shown for H. *The Journal of chemical physics*, 126:104102, 2007.

[104] F. Corà, M. Alfredsson, G. Mallia, D. S. Middlemiss, W. C. Mackrodt, R. Dovesi, and R. Orlando. *Structure of Bonding*, chapter The performance of hybrid density functionals in solid state chemistry, pages 171–232. Springer, 2004.

[105] V. I. Anisimov, J. Zaanen, and O. K. Andersen. Band theory and Mott insulators: Hubbard U instead of Stoner I. *Physical Review B*, 44:943–954, 1991.

[106] J. Tao, J. P. Perdew, V. N. Staroverov, and G. E. Scuseria. Climbing the density functional ladder: Nonempirical meta-generalized gradient approximation designed for molecules and solids. *Physical Review Letters*, 91:146401, 2003.

[107] A. D. Becke. A new mixing of Hartree-Fock and local density-functional theories. *Journal of Chemical Physics*, 98:1372–1377, 1993.

[108] M. Ernzerhof. Construction of the adiabatic connection. *Chemical Physics Letters*, 263:499–506, 1996.

[109] J. P. Perdew, M. Ernzerhof, and K. Burke. Rational for mixing exact exchange with density functional approximations. *Journal of Chemical Physics*, 105:9982–9985, 1996.

[110] C. Adamo and V. Barone. Toward reliable density functional methods without adjustable parameters: The PBE0 model. *The Journal of chemical physics*, 110:6158–6170, 1999.

[111] V. L. Chevrier, S. P. Ong, R. Armiento, M. K. Y. Chan, and G. Ceder. Hybrid density functional calculations of redox potentials and formation energies of transition metal compounds. *Physical Review B*, 82:075122, 2010.

[112] J. Heyd, G. E. Scuseria, and M. Ernzerhof. Hybrid functionals based on a screened Coulomb potential. *The Journal of Chemical Physics*, 118:8207–8215, 2003.

[113] F. Zhou, C. A. Marianetti, M. Cococcioni, D. Morgan, and G. Ceder. Phase separation in Li_xFePO_4 induced by correlation effects. *Physical Review B*, 69:201101, 2004.

[114] V. I. Anisimov, F. Aryasetiawan, and A. Lichtenstein. First-principles calculations of the electronic structure and spectra of strongly correlated systems: the LDA+ U method. *Journal of Physics: Condensed Matter*, 9:767–808, 1997.

[115] A. Rohrbach, J. Hafner, and G. Kresse. Electronic correlation effects in transition-metal sulfides. *Journal of Physics: Condensed Matter*, 15:979, 2003.

[116] J. Hubbard. Electron correlations in narrow energy bands. *Proceedings of the Royal Society of London. Series A. Mathematical and Physical Sciences*, 276:238–257, 1963.

[117] S. L. Dudarev, G. A. Botton, S. Y. Savrasov, C. J. Humphreys, and A. P. Sutton. Electron-energy-loss spectra and the structural stability of nickel oxide: An LSDA+ U study. *Physical Review B*, 57:1505–1509, 1998.

[118] D. Maurice and M. Head-Gordon. Analytical second derivatives for excited electronic states using the single excitation configuration interaction method: theory

and application to benzo[a]pyrene and chalcone. *Molecular Physics*, 96:1533–1541, 1999.

[119] C. Møller and M. S. Plesset. Note on an approximation treatment for many-electron systems. *Physical Review*, 46:618, 1934.

[120] J. Kolorenč and L. Mitas. Applications of quantum Monte Carlo methods in condensed systems. *Reports on Progress in Physics*, 74:026502, 2011.

[121] http://www.ccp5.ac.uk/DL_POLY/Democritus/Theory/pbc-mi.html.

[122] I. Saadoune, F. Corà, and C. R. A. Catlow. Computational study of the structural and electronic properties of dopant ions in microporous AlPOs. 1. Acid catalytic activity of divalent metal ions. *The Journal of Physical Chemistry B*, 107:3003–3011, 2003.

[123] A. Heyden, A. T. Bell, and F. J. Keil. Efficient methods for finding transition states in chemical reactions: Comparison of improved dimer method and partitioned rational function optimization method. *The Journal of chemical physics*, 123:224101, 2005.

[124] https://en.wikipedia.org/wiki/Energy_profile_(chemistry).

[125] H. Jónsson, G. Mills, and K. W. Jacobsen. Nudged elastic band method for finding minimum energy paths of transitions. *Classical and quantum dynamics in condensed phase simulations*, 1:385–404, 1998.

[126] G. Henkelman and H. Jónsson. A dimer method for finding saddle points on high dimensional potential surfaces using only first derivatives. *The Journal of chemical physics*, 111:7010–7022, 1999.

[127] A. Laio and M. Parrinello. Escaping free-energy minima. *Proceedings of the National Academy of Sciences*, 99:12562–12566, 2002.

[128] R. Dovesi, V. R. Saunders, C. Roetti, R. Orlando, C. M. Zicovich-Wilson, F. Pascale, B. Civalleri, K. Doll, N. M. Harrison, I. J. Bush, Ph. D'Arco, and M. Llunell. *CRYSTAL09*. Torino,Italy, 2009.

[129] http://www.crystal.unito.it/Manuals/crystal14.pdf.

[130] Ionicity and framework stability of crystalline aluminophosphates.

[131] http://www.crystal.unito.it/Basis_Sets/Ptable.html.

[132] L. Gómez Hortigüela, F. Corà, and C. R. A. Catlow. Complementary mechanistic properties of Fe-and Mn-doped aluminophosphates in the catalytic aerobic oxidation of hydrocarbons. *Physical Chemistry Chemical Physics*, 15:6870–6874, 2013.

[133] J. P. Perdew, J. A. Chevary, S. H. Vosko, K. A. Jackson, M. R. Pederson, D. J. Singh, and C. Fiolhais. Atoms, molecules, solids, and surfaces - Applications of the generalized gradient approximation for exchange and correlation. *Physical Review B*, 46:6671–6687, 1992.

[134] W. R. McKinnon. Insertion electrodes I: Atomic and electronic structure of the hosts and their insertion compounds. *Solid state electrochemistry*, pages 163–198, 1995.

[135] http://www.archer.ac.uk/about-archer/.

[136] https://wiki.rc.ucl.ac.uk/wiki/Legion.

[137] H. H. Kung. *Transition Metal Oxides: Surface Chemistry and Catalysis.*, volume 45. Elsevier, Amsterdam, 1989.

[138] J. M. Thomas and W.J. Thomas. *Principles and Practice of Heterogeneous Catalysis*. Weinham, 1996.

[139] O. Deutschmann, H. Knözinger, K. Kochloefl, and T. Thomas. Heterogeneous catalysis and solid catalysts. In *Ullmann's Encyclopedia of Industrial Chemistry*. 2009.

[140] J. Heyd, G. E. Scuseria, and M. Ernzerhof. Efficient hybrid density functional calculations in solids: assessment of the Heyd-Scuseria-Ernzerhof screened Coulomb hybrid functional. *The Journal of chemical physics*, 121:1187–1192, 2004.

[141] M. Alfredsson, G. D. Price, C. R. A. Catlow, S. C. Parker, R. Orlando, and J. P. Brodholt. Electronic structure of the antiferromagnetic *B*1-structured FeO. *Physical Review B*, 70:165111, 2004.

[142] X. Feng and N. M. Harrison. Magnetic coupling constants from a hybrid density functional with 35% Hartree-Fock exchange. *Physical Review B*, 70:092402, 2004.

[143] A. S. Andersson, B. Kalska, L. Häggström, and J. O. Thomas. Lithium extraction/insertion in LiFePO 4: an X-ray diffraction and Mössbauer spectroscopy study. *Solid State Ionics*, 130:41–52, 2000.

[144] A. Belsky, M. Hellenbrandt, V. L. Karen, and P. Luksch. New developments in the Inorganic Crystal Structure Database (ICSD): accessibility in support of materials research and design. *Acta Crystallographica Section B: Structural Science*, 58:364–369, 2002.

[145] F. Zhou, K. Kang, T. Maxisch, G. Ceder, and D. Morgan. The electronic structure and band gap of $LiFePO_4$ and $LiMnPO_4$. *Solid State Communications*, 132:181–186, 2004.

[146] P. Pelekanaki, L. Gómez Hortigüela, C. R. A. Catlow, and F. Corà. Effect of exchange functionals on the calculated activation energies - A DFT study of the catalytic aerobic oxidation of ethane in MnAlPO-5. *prepared*.

[147] L. Gómez Hortigüela, F. Corà, and C. R. A. Catlow. Mechanism and Energetics of Secondary Oxidation Reactions in the Aerobic Oxidation of Hydrocarbons Catalyzed by Mn-Doped Nanoporous Aluminophosphates. *The Journal of Physical Chemistry C*, 116:6691–6702, 2012.

[148] J. Paterson, M. Potter, E. Gianotti, and R. Raja. Engineering active sites for enhancing synergy in heterogeneous catalytic oxidations. *Chemical Communications*, 47:517–519, 2011.

[149] B. Notari. Microporous crystalline titanium silicates. *Advances in catalysis*, 41:253–334, 1996.

Appendix A

Proof of HK Theorem 1

If we have two external potentials $V(\mathbf{r})$ and $V'(\mathbf{r})$ that differ by more than an additive constant, then we want to show that the resulting ground-state densities $\rho(\mathbf{r})$ and $\rho'(\mathbf{r})$ cannot be the same. I denote by $H = H_0 + V$ and $H' = H_0 + V'$ the Hamiltonians associated with the two potentials v and v' and their ground-state many-electron wavefunctions are called Ψ and Ψ'; these wavefunctions are necessarily different. Then by the variational principle we have:

$$E' = \langle \Psi' | H' | \Psi' \rangle < \langle \Psi | H' | \Psi \rangle = \langle \psi | H_0 + V + (V' - V) | \Psi \rangle \tag{A.1}$$

Hence:

$$E' < E + \langle \Psi | V' - V | \Psi \rangle = E + \int d\mathbf{r} \rho(\mathbf{r})(V'(\mathbf{r}) - V(\mathbf{r})) \tag{A.2}$$

We can use the same argument to prove that:

$$E < E' + \int d\mathbf{r} \rho'(\mathbf{r})(V(\mathbf{r}) - V'(\mathbf{r})) \tag{A.3}$$

Adding the two equations, we get:

$$E' + E < E + E' - \int d\mathbf{r} \rho'(\mathbf{r}) - \rho(\mathbf{r})(V'(\mathbf{r}) - V(\mathbf{r})) \tag{A.4}$$

But since this a strict inequality, we cannot have $\rho'(\mathbf{r}) = \rho(\mathbf{r})$

Appendix B

Proof of HK Theorem 2

If $E[\rho(\mathbf{r})]$ is the ground-state energy associated with external potential $V(\mathbf{r})$, then we have to show that:

$$E[\rho(\mathbf{r})] \leq \int V(\mathbf{r})\rho'(\mathbf{r})dr + F[\rho'(\mathbf{r})] \tag{B.1}$$

where $\rho'(\mathbf{r})$ is the density associated with any arbitrary external potential $V'(\mathbf{r})$. Equality holds only if $\rho'(\mathbf{r}) = \rho(\mathbf{r})$, which by theorem 1 occurs only if $V'(\mathbf{r})$ and $V(\mathbf{r})$ differ by at most as additive constant.

The proof follows immediately from the variational principle. Let Ψ and Ψ' be the many-electron ground-state wave functionals associated with $V(\mathbf{r})$ and $V'(\mathbf{r})$. Then:

$$E[\rho(\mathbf{r})] < \langle \Psi | H_0 + V | \Psi' \rangle = \int V(\mathbf{r})\rho'(\mathbf{r})dr + F[\rho'(\mathbf{r})] \tag{B.2}$$

which proves the theorem.